Performance Evaluation of T-transform Based OFDM in Underwater Acoustic Channels

Hengda Ding

School of Electrical and Electronic Engineering

Newcastle University

A thesis submitted for the degree of

Doctor of Philosophy

November 2016

To my family and those who helped me along this journey.

Acknowledgements

First and foremost, I would like to express my deepest gratitude to my primary supervisor Jeff Neasham for his generous support and understanding throughout the course of my PhD. His enthusiasm about engineering guided me in achieving the goals I have made in this research. I would also like to thank my secondary supervisors, Said Boussakta and Charalampos Tsimenidis, for their valuable comments and sharing of their great knowledge on both theory and practical aspects of underwater communications.

My gratitude extends to my thesis examination committee members for their time, constructive criticism, and feedback. This thesis is much the better because of them.

Secondly, I would like to express my gratitude to my lab colleagues, Dave Graham, Gerry Goodfellow and Ben Sherlock. The dedication they have shown on their work has always urged me to consummate my own research. Without the sharing of their experience and knowledge, this journey could have been a lot harder for me. Outside of work, I would like to thank all of my close friends for being a lively and entertaining part of this journey. Special thanks to my best friends, Dave, Jamie, Gerry and Maede, for all the ups and downs we have shared together in the past four years. Because of you guys, I felt a lot closer to home.

Lastly, my heartfelt thanks to my father and mother for the love, generous care and support they provided me all my life. I am truly blessed to have them as my parents. My biggest thanks to my wife Yadi. Without her encouragement and understanding, it would be impossible for me to finish this work.

Abstract

Recently there has been an increasing trend towards the implementation of orthogonal frequency division multiplexing (OFDM) based multicarrier communication systems in underwater acoustic communications. By dividing the available bandwidth into multiple sub-bands, OFDM systems enable reliable transmission over long range dispersive channels. However, OFDM is prone to impairments such as severe frequency selective fading channels, motioned induced Doppler shift and high peak-to-average-power ratio (PAPR). In order to fully exploit the potential of OFDM in UWA channels, those issues have received a great deal of attention in recent research.

With the aim of improving OFDM's performance in UWA channels, a T-transformed based OFDM system is introduced using a low computational complexity T-transform that combines the Walsh-Hadamard transform (WHT) and the discrete Fourier transform (DFT) into a single fast orthonormal unitary transform. Through real-world experiment, performance comparison between the proposed T-OFDM system and conventional OFDM system revealed that T-OFDM performs better than OFDM with high code rate in frequency selective fading channels. Furthermore, investigation of different equalizer techniques have shown that the limitation of ZF equalizers affect the T-OFDM more (one bad equalizer coefficient affects all symbols) and so developed a modified ZF equalizer with outlier detection which provides major performance gain without excessive computation load. Lastly, investigation of PAPR reduction methods delineated that T-OFDM has inherently lower PAPR and it is also far more tolerant of distortions introduced by the simple clipping method. As a result, lower PAPR can be achieved with minimal overhead and so outperforming OFDM for a given power limit at the transmitter.

Contents

List of Tables

List of Figures

List of Abbreviations and Symbols

List of Symbols

A Amplitude

B Magnetic Field

C Capacitance

c   Speed of Sound

E   Expected Value

f Frequency

f_c Centre Frequency

f_s Sampling Frequency

I   Identity Matrix

L   Inductance

P_a Acoustic Power

P_e Electrical Power

$n(t)$ Noise Signal

$r(t)$ Received Signal

$s(t)$ Transmitted Signal

r	Transmission Range
$\hat{s}_n$	Equalizer Symbol Estimates
s_n	Transmitted Signal
T	Symbol Duration
TL	Transmission Loss
U	Upper Triangular Matrix
α	Absorption Coefficient
Δ	Induced Doppler Shift
δ	Skin Dpeth
γ	Conductivity
Λ	Diagonal Matrix
λ	Wavelength
ω	Angular Frequency
π	Mathematical Constant
ψ	Angle of Arrival
ρ	Resistivity
σ	Standard Deviation
τ	Delay
Θ	Induced Doppler Shift
φ	Grazing Angle of an Acoustic Ray
$(.)^{*}$	Complex Conjugate
$(.)^{T}$	Matrix Transpose
$(.)^{H}$	Hermitian Transpose

$*$	Linear convolution operation
$\circledast$	Circular convolution operation
Γ	The probability of $\varsigma_n = 1$
$\hat{\Gamma}$	The probability of $\varsigma_n = 0$
$\hat{R}$	Received signal in Frequency-domain
$\hat{T}$	Inverse T-transform matrix
$\hat{X}$	Equalized data sequence
$\hat{d}$	The resultant data sequence of PTS scheme in the time-domain
$\hat{L}$	Number of the channel paths
$\hat{m}$	Data index in the Walsh-domain
$\hat{m}_{\hat{r}}$	Bit representation of index $\hat{m}$
$\hat{w}^n$	Twiddle factor of T-transform
$\xi\{.\}$	Imaginary part of complex value
λ_0	SNR of transmission
$\hat{Q}$	Equalizer sequence in the Walsh-domain
$\hat{q}$	The disjoint sub blocks of the PTS scheme
A and **B**	Sub-matrices of the FFT matrix **F**
A''' and **B'''**	Sub-matrices of the matrix **B'**
A' and **A''**	Sub-matrices of the matrix **A**
B' and **B''**	Sub-matrices of the matrix **B**
C and **C'**	Sub-matrices of the matrix **A'**
C''' and **E'''**	Sub-matrices of the matrix **B''**
D	Circulant channel matrix

$\mathbf{d}^{(u)}$	The uth disjoint sub block in SLM and PTS scheme
$\mathbf{F}$	DFT matrix
$\mathbf{h}$	Vector of the channel impulse response
$\mathbf{s}$	Phase rotation vector of the SLM scheme
$\mathbf{T}$	Forward T-transform matrix
$\mathbf{v}$	Phase optimized vector in SLM and PTS scheme
$\mathbf{W}$	WHT matrix
$\mathbf{X}$	Discrete frequency-domain sequence
$\mathbf{x}$	Discrete time-domain sequence
Ω_k	The quantity that equivalent to $Q_k H_k$
$\oplus$	Bit-by-bit modulo 2 sum of the integers
$\otimes$	The tensor or Kronecker product operation
$\overline{\otimes}$	Dyadic convolution operation
ρ	Gaussian noise in Walsh-domain
σ_x^2	Desired signal average power
σ_z^2	White Gaussian noise average power
$E[.]$	Expectation operator
L	Oversampling factor
N	Number of the subcarriers
N_g	CP length
N_t	Total length of symbol

List of Abbreviations

16-QAM   Sixteen-Quadrature Amplitude Modulation

ADSL   Asymmetric Digital Subscriber Lines

ADC   Analogue to Digital Converter

AM   Amplitude Modulation

ASK   Amplitude Shift Keying

AWGN   Additive White Gaussian Noise

BER   Bit Error Rate

BICM   Bit Interleaved Coding and Modulation

CIR   Channel Impulse Response

CP   Cyclic Prefix

CSI   Channel State Information

CRC   Cyclic Redundancy Check

DAC   Digital to Analogue Converter

DFE   Decision Feedback Equalizer

DFT   Discrete Fourier Transform

DSI   Dummy Sequence Insertion

EM   Electro Magnetic

FDM   Frequency Division Multiplexing

FIR   Finite Impulse Response

FSK   Frequency Shift Keying

FFT   Fast Fourier Transform

FEC	Forward Error Correction
FS	Frequency Selective
HF	High Frequency
ICI	Inter-Carrier Interference
ISI	Inter-Symbol Interference
IEEE	Institute of Electrical and Electronics Engineers
IFFT	Inverse Fast Fourier Transform
ITT	Inverse T-Transform
LED	Light Emitting Diode
LE	Linear Equalizer
LFM	Linear Frequency Modulation
LMS	Lease Mean Square
LOS	Line-Of-Sight
M-PSK	M-array Phase Shift Keying
M-QAM	M-array Quadrature Amplitude Modulation
MC	Multicarrier
MI	Magneto Inductive
MSME	Minimum Mean Square Error
MSE	Mean Square Error
OFDM	Orthogonal Frequency Division Multiplexing
PAPR	Peak-to-Average Power Ratio
PTS	Partial Transmitted Sequence
QPSK	Quadrature Phase Shift Keying

RF   Radio Frequency

RLS   Recursive Least Squares

RMS   Root Mean Square

SC   Single Carrier

SI   Side Information

SLM   Selective Mapping

SNR   Signal-to-Noise Ratio

T   T-transform

TR   Tone Reservation

UAC   Underwater Acoustic Communication

WHT   Walsh-Hadamard Transform

ZF   Zero-Forcing

CHAPTER 1

Introduction

Orthogonal frequency division multiplexing (OFDM) represented multicarrier underwater acoustic communication systems have received a great deal of attention recently due to its ability of enabling high data rate transmission over long range dispersive channels. OFDM systems divide the available bandwidth into multiple sub-bands, as a result, the frequency selective fading channel can be regarded as flat fading within each sub-band. This makes OFDM an ideal candidate for the highly dispersive underwater acoustic channel. On the contrary, OFDM systems suffer from low immunity against severe frequency selective fading as deep fades attenuate certain subcarriers resulting in an enormously high BER unless strong FEC coding, interleaving, switching off the most attenuated subcarriers or adaptive bit loading are applied. Additionally, the high peak-to-average power ratio arise from the overlapping subcarriers necessitates the usage of a highly linear preamplifier which not only increases the cost of the whole system but also hampers the overall performance.

In order to deal with those detrimental aspects of OFDM systems, a T-transform based OFDM system is proposed in this thesis. The T-transform combines Walsh-Hadamard transform and discrete Fourier transform, providing high frequency diversity gain by spreading the transmitted data onto all subcarriers therefore increase the robustness of OFDM systems against frequency selective fading channels. This thesis focused on channel equalizer design and evaluating the optimal PAPR reduction technique for the proposed T-OFDM system.

1.1 Contributions

The key areas of novelty can be attributed to the development of a reliable, high speed underwater acoustic communication system. The research specifically focused on the design of a modified ZF channel equalizer for T-OFDM in underwater environment and the evaluation of various PAPR reduction techniques and the selection of an optimal PAPR reduction technique for T-OFDM in UWA channels. The following list summarizes the key contributions that have been made within the scope of this research.

1. T-OFDM systems outperform OFDM system in severe multipath channels due to the spectral diversity introduced by the Walsh-Hadamard transform without affecting throughput.

2. T-OFDM systems can be used with lower redundancy (high throughput) than OFDM so spectral efficiency is increased.

3. T-OFDM systems suffer more from inaccurate channel coefficients in deep fades due to spectral spreading (one bad coefficient affects all subcarriers)

4. A modified ZF channel equalizer can mitigate the effect of noise enhancement and maximize the advantage of T-OFDM's high spectral efficiency.

5. BER performance of the proposed T-OFDM system degrades more gracefully with signal clipping, hence large gains in performance can be achieved using a very simple PAPR reduction technique (and amplifier non-linearity is also better tolerated).

6. Investigation and evaluation of the T-transform based OFDM in UWA environment.

1.2 Publications

The following papers have been published based on the research presented in this thesis:

[1] **H. Ding**, J. A. Neasham, S. Boussakta and C. C. Tsimenidis, "Performance evaluation of T-transform based OFDM in underwater acoustic communications," *OCEANS 2015 – Genova,* Genoa, 2015, pp. 1-7.

[2] **H. Ding**, J. A. Neasham, S. Boussakta and C. C. Tsimenidis, "Performance Evaluation of T-transform based OFDM with PAPR reduction in underwater acoustic communications," submitted to *IEEE Journal of Oceanic Engineering*.

1.3 Thesis Outline

The structure of this thesis is outlined in the following paragraphs.

Chapter 2 provides an overview on underwater acoustic communications starting with a selection of transmission mechanisms. The dominant difficulties encountered in transmitting wirelessly underwater are analyzed. A brief review on research milestones conducted through the years in the form of phase coherent and non-coherent transmissions is given. The state-of-the art coherent systems are also presented. Lastly, OFDM represented multicarrier transmission systems are demonstrated stating its inherent advantage in terms of multipath resilience and reduction in receiver complexity.

Chapter 3 outlined the key concepts of OFDM systems with an emphasis on the effect of multipath transmission and the design of guard intervals. The fast transforms associated with OFDM systems, namely, discrete Fourier transform (DFT) and Walsh-Hadamard transform (WHT) are discussed in terms of the basic ideas and computational complexity. Moreover, the T-transform which combines DFT and WHT is also presented, with an illustration of T-transform based OFDM system. Lastly, training symbol based channel equalization techniques were introduced.

Chapter 4 investigates the performance of conventional OFDM and the proposed T-OFDM system in underwater channels. Three types of receiver were presented with the corresponding computational complexity analysis. Theoretical performance of both conventional OFDM and T-OFDM were demonstrated for AWGN channel, flat-fading channel and frequency selective fading channel. Finally, water tank results comparing the BER performance and system throughput of OFDM and T-OFDM systems were presented.

Chapter 5 focused on equalization techniques for OFDM and T-OFDM system. A modified ZF channel equalizer is proposed in order to suppress the detrimental noise enhancement effect. Performance of the proposed equalizer is tested in both water tank and via sea trial in comparison to a DCT-OFDM system represented pre-coded OFDM systems.

Chapter 6 presents an evaluation of PAPR reduction techniques in the proposed T-OFDM systems. Various PAPR reduction techniques are analyzed and an optimal technique is chosen and tested in both water tank and real world environment. With the selected PAPR reduction technique, the proposed T-OFDM system revealed significant BER performance improvement

against conventional OFDM system, and validates the effectiveness of the selected PAPR reduction technique.

Chapter 7 summarizes the key contributions of the preceding chapters, highlighting the most notable finding and emphasizes a set of design recommendation for the development of a high data rate underwater multicarrier communication system. Finally, the author highlights aspects of future work, indicating areas where further contribution to the academic field could be made.

CHAPTER 2

Background and State-of-the-Art

Exploration of the mysterious world under ocean surface has never been ceased from the birth of human civilization. Our knowledge and understanding of the underwater world relies on the ability to accumulate information from remote underwater locations, whereas the discovery has always been scarce. Fortunately, such progress has been vastly accelerated through the development of wireless underwater communication systems in the past decades. Along with vehicular technology and sensor technology, wireless communication facilitates new applications ranging from navigation and positioning to environmental monitoring and marine archaeology. This chapter presents the background of underwater wireless communication and draws the attention to some of the common difficulties encountered in designing underwater wireless communication systems. A literature overview offers insight into the current state-of-the-art and provides context to the proposed area of research.

2.1 Underwater Wireless Communication

The characteristics of the wireless channel experienced in underwater environment are determined by the information carrier. Different techniques have been explored in order to achieve reliable communications sub-sea. Historically, research has been focused on transmission schemes utilizing electromagnetic, optical and acoustic waves. Before its implementations sub-sea, the electromagnetic (EM) communication is already widely used in the air channel. However, due to the skin effect caused by the conductive nature of water channel where currents tend to flow with higher density close to the water surface [1], only

radio waves with extremely low frequencies (30Hz~300Hz) will propagate through any desirable distance with a huge antenna and immense transmitter power required. On the other hand, optical waves are less affected by attenuation but highly prune to scattering. Consequently transmission using optical waves demands high precision in aligning the transmitter and receiver where narrow light beams are optimal for effective transmission. Components such as high quality Light Emitting Diodes (LED) or laser diodes are used for generating information carrying beams where avalanche diodes or Photo Multiplier Tubes (PMT) are paired at the receiver to ensure good signal-to-noise ratio [2]. Latest researches have been focused on utilizing narrow laser beams to overcome the turbidity of the water in order to extend the transmission range. Although laser technology is still being polished for practical use, the set up for directional light sources and receiver still puts limitation on operational complexity and maintenance [3].

2.1.1 Underwater Acoustic Communication

During the past decades, acoustic communication has witnessed a vast development in underwater channels due to its ability to overcome high attenuation and severe scattering in long range transmissions. It was first developed during the Second World War in the United States for communicating between submarines [4]. In late 80's more complex systems were made available through the emergence of powerful DSPs with moderate power consumption. Systems capable of accomplishing the impossible previously have been made available with the latest development [5] where acoustically controlled robots have been used in replacement of divers performing maintenance of submerged platforms [6], high-quality video transmission from the bottom of deepest ocean trenches (6500 m) to the surface ship was established [7]; and data telemetry over horizontal distances in excess of 200 kilometers was demonstrated [8]. Unlike optical waves, acoustic transmission experiences minimal degradation due to the turbidity of the water which result in less spread and scattering by suspended sediment or particles. Also, the omnidirectional radiation of acoustic signals substantially lowers the requirement of alignment enabling the free positioning for both transmitter and receiver within the water column. With the development of efficient communication systems, the field of their applications continues to expand, and so do the requirement on the system throughput and

performance. Current research is focusing on the development of efficient communications and signal processing algorithms, design of efficient modulation and coding schemes, multiple access methods, and techniques for mobile underwater communications.

2.2 Channel Characteristics

The propagation of acoustic signal underwater is principally driven by transmission loss, ambient noise level, reverberation and temporal and spatial variability of the channel [4], where transmission loss and noise level are the primary deterministic factors for the available bandwidth, range and signal-to-noise ratio. The time variability of the channel often acts as a limitation for system performance due to its influences on signal design and processing.

2.2.1 Underwater Acoustic Propagation: path loss and background noise

2.2.1. A. Attenuation

The path loss through acoustic transmission underwater is caused by spreading and sound absorption. Given an acoustic signal with frequency f, the path loss over a distance d is given by [10]:

$$A(d,f) = A_0 d^k \alpha(f)^d \tag{2.2.0}$$

where A_0 is a unit-normalizing constant, k is the spreading factor, and α stands for the absorption coefficient. The logarithmic representation of the acoustic path loss is given by:

$$10\log[A(d,f)/A_0] = k \cdot 10\log d + d \cdot 10\log\alpha(f) \tag{2.2.1}$$

The first term stands for the spreading loss and the second term represents the absorption loss. The geometry of the transmission is described by the spreading factor k. For spherical spreading the common value of k is $k = 2$, while $k = 1$ for cylindrical spreading is typically used. The absorption coefficient is usually expressed empirically using Thorp's model which gives $\alpha(f)$ in dB/km for f in kHz as [110]:

$$10\log\alpha(f) = \frac{0.1f_c{}^2}{1+f_c{}^2} + \frac{40f_c{}^2}{4100+f_c{}^2} + 2.75 \times 10^{-4}f_c{}^2 + 0.003 \tag{2.2.2}$$

The above is best suited for frequencies above a few hundred Hertz. Whilest the following representation is applies instead for lower frequencies:

$$10 \log \alpha(f) = 0.002 + 0.11 \frac{f_c{}^2}{1 + f_c{}^2} + 0.011 f_c{}^2 \qquad (2.2.3)$$

The relationship between the absorption coefficients and frequency is best illustrated in Figure 2.1.
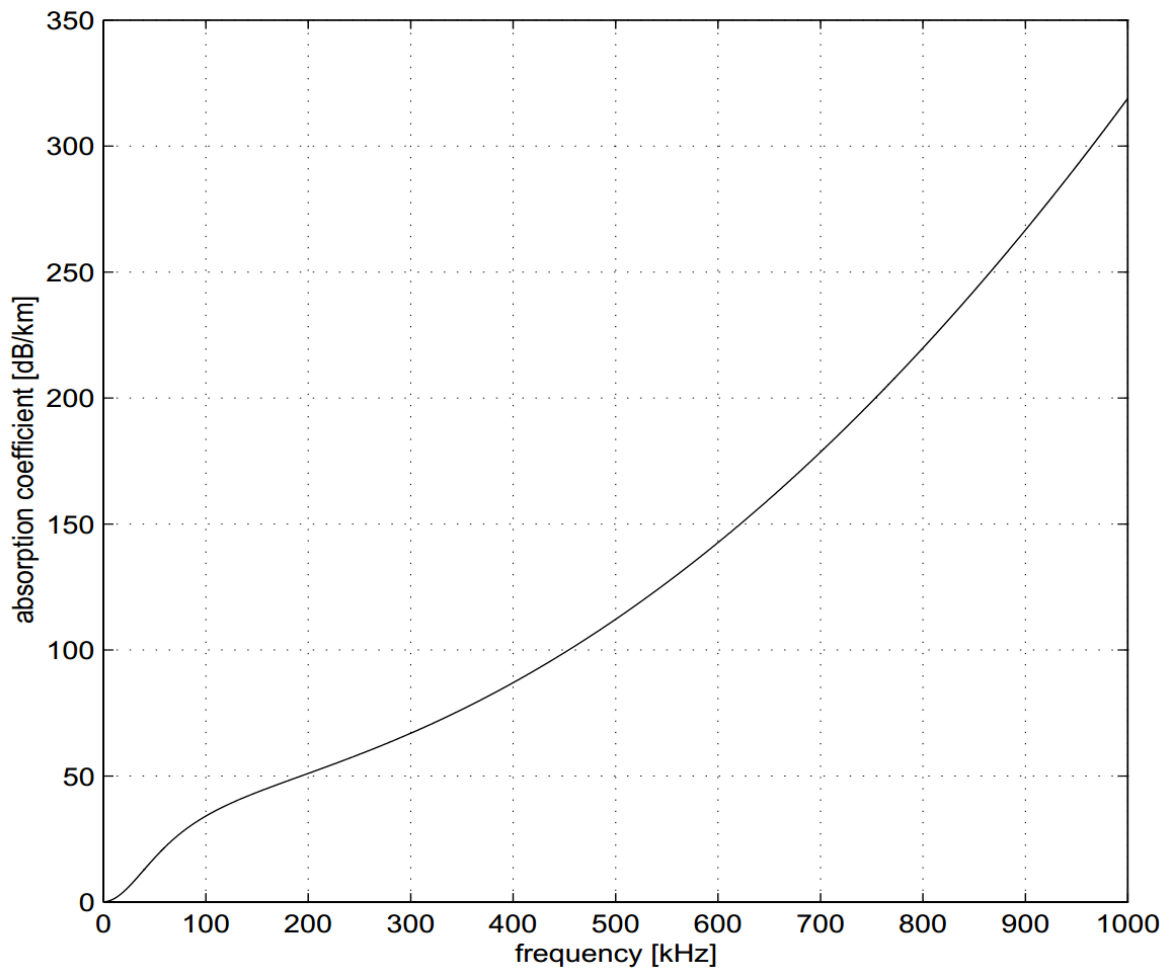
Figure 2.1: Absorption coefficient $\alpha(f)$ in dB/km.

From Figure 2.1 it is clear that the maximal usable frequency for a given acoustic link is restricted by the absorption coefficient as it increases drastically with frequency.

2.2.1. B. Ambient noise

Although the transmission loss at a certain location can be predicted using a pre-determined stochastic propagation model [9], the degree of accuracy cannot be guaranteed. On the other

hand, noise observed subsea unveils strong frequency dependency as well as site dependency. In ocean environments, inshore sites experience much higher noise level than offshore environments from the frequent human activities while most of the ambient noise can be modelled using a continuous spectrum and Gaussian statistics [11]. In general the most prominent noise sources across all water environments are thermal noise, shipping noise, the turbulence and wind driven waves [11]. Their power spectral density (PSD) in dB per μPa per Hz are shown below respectively [11].

$$10 \log N_{thermal}(f) = -15 + 20 \log f \tag{2.2.4}$$

$$10 \log N_s(f) = 40 + 20(S - 0.5) + 26 \log f - 60 \log(f + 0.03) \tag{2.2.5}$$

$$10 \log N_{turb}(f) = 17 - 30 \log f \tag{2.2.6}$$

$$10 \log N_{wind}(f) = 50 + 7.5\sqrt{\kappa} + 20 \log f - 40 \log(f + 0.4) \tag{2.2.7}$$

As can be seen from (2.2.4) to (2.2.7), the ambient noise in the ocean is associated with many different factors with specific frequency. Turbulence noise only influences frequencies $f <$ 10 Hz. In the region of $10\ \text{Hz} - 100\ \text{Hz}$ shipping noise $N_s(f)$ is the dominant factor with shipping factor S ranges between 0 and 1. $N_{wind}(f)$ represents the noise generated from wind driven waves (with κ as the wind speed in m/s and mainly influences frequencies ranging from 100 Hz to 100 kHz. For $f > 100$ kHz, thermal noise $N_{thermal}(f)$ becomes prominent.

Finally, the composite noise PSD $N_f = N_{thermal}(f) + N_s(f) + N_{turb}(f) + N_{wind}(f)$ in μPa is shown in Figure 2.2. [26]:
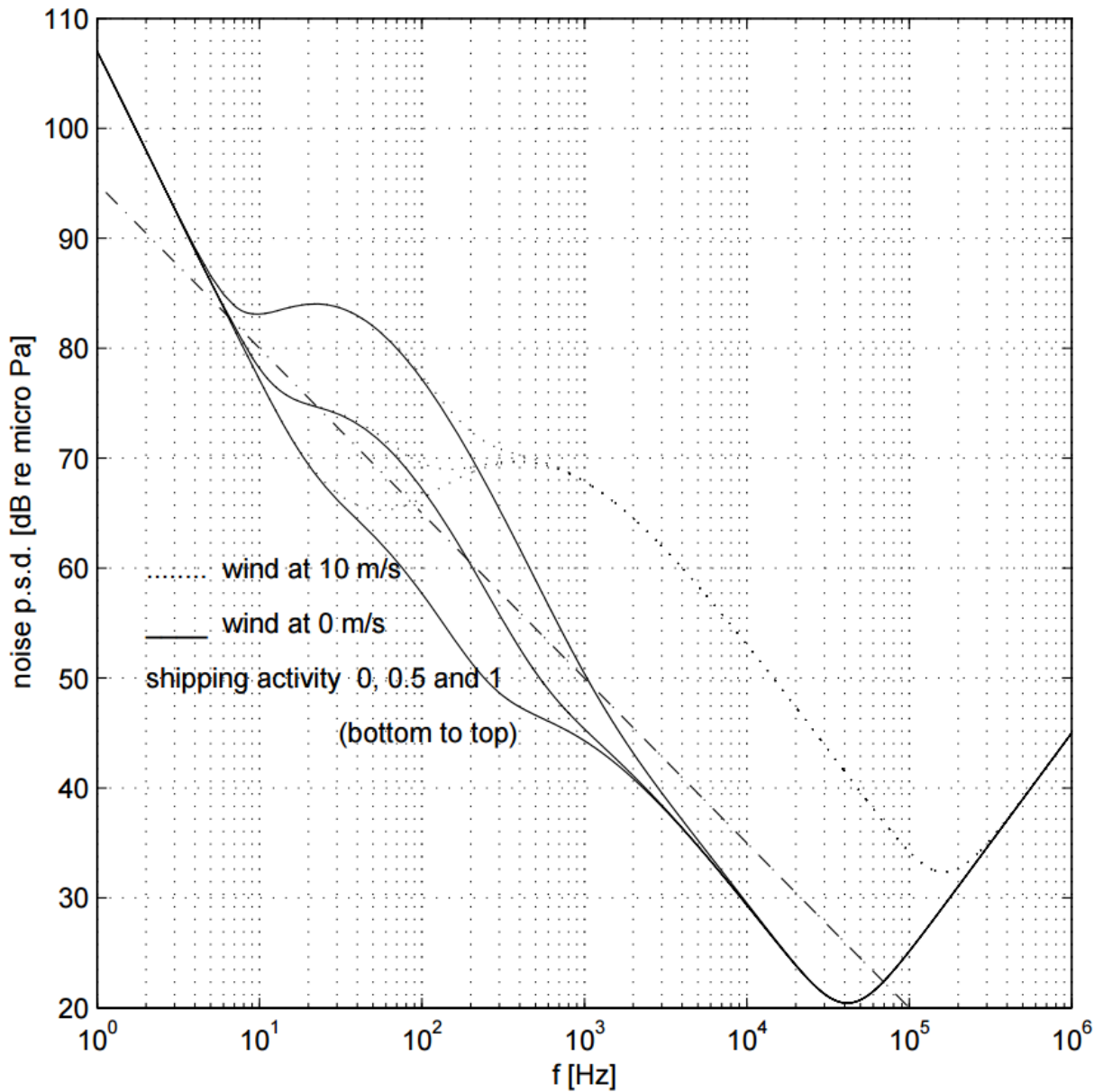
Figure 2.2: Power spectral density of composite ambient noise N_f. The solid and dotted line represents the cases of no wind and moderate wind (10 m/s), respectively. The dash-dotted line shows an approximate linear decay on the logarithmic scale of $10 \log N(f) = 50 - 18 \log f$ [26].

A more comprehensive view of a selection of dominant noise sources encountered in a typical marine environment is summarized in Figure 2.3 by visualizing a pressure spectral density graph. Note that some type of ambient noises can be predicted and estimated based on the location and operating time of the year. Whilst other forms of noise are deemed to be erratic and unpredictable due to the nature of the channel itself.
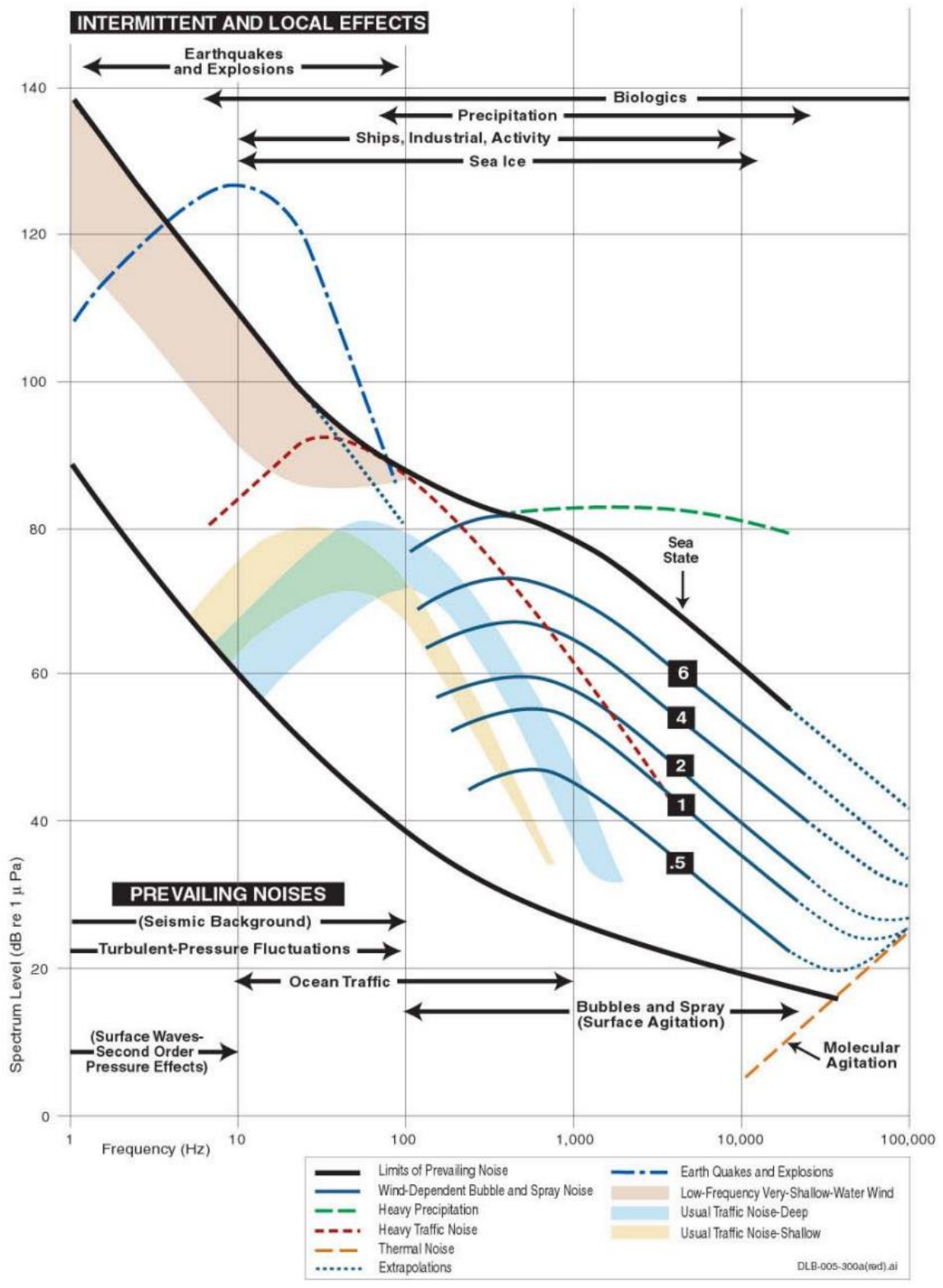
Figure 2.3: Wenz curves showing the pressure spectral density levels of marine ambient noise. Original curves developed by Wenz [49], with additional overlays of marine mammal activity by David Bradley. Source image from "*Ocean Noise and Marine Mammals*" [50].

2.2.1. C. Signal-to-Noise-Level

Combining the frequency dependent transmission loss with ambient noise determines the relationship between transmission range, available bandwidth and SNR at the receiver. Considering only the pass loss, the narrow-band SNR in UWA channel can be calculated as [26]:

$$\text{SNR}(d, f) = \frac{P}{A(d, f)N(f)\Delta f} \tag{2.2.8}$$

where $\text{SNR}(d, f)$ represents the SNR over a distance d with center transmission frequency f. P is the signal transmission power and Δf stands for the receiver noise bandwidth. Evidently, the optimal frequency can be determined using (2.2.8) according to the attenuation-noise factor $A(d, f)$. This relationship is illustrated in Figure 2.4 [10].
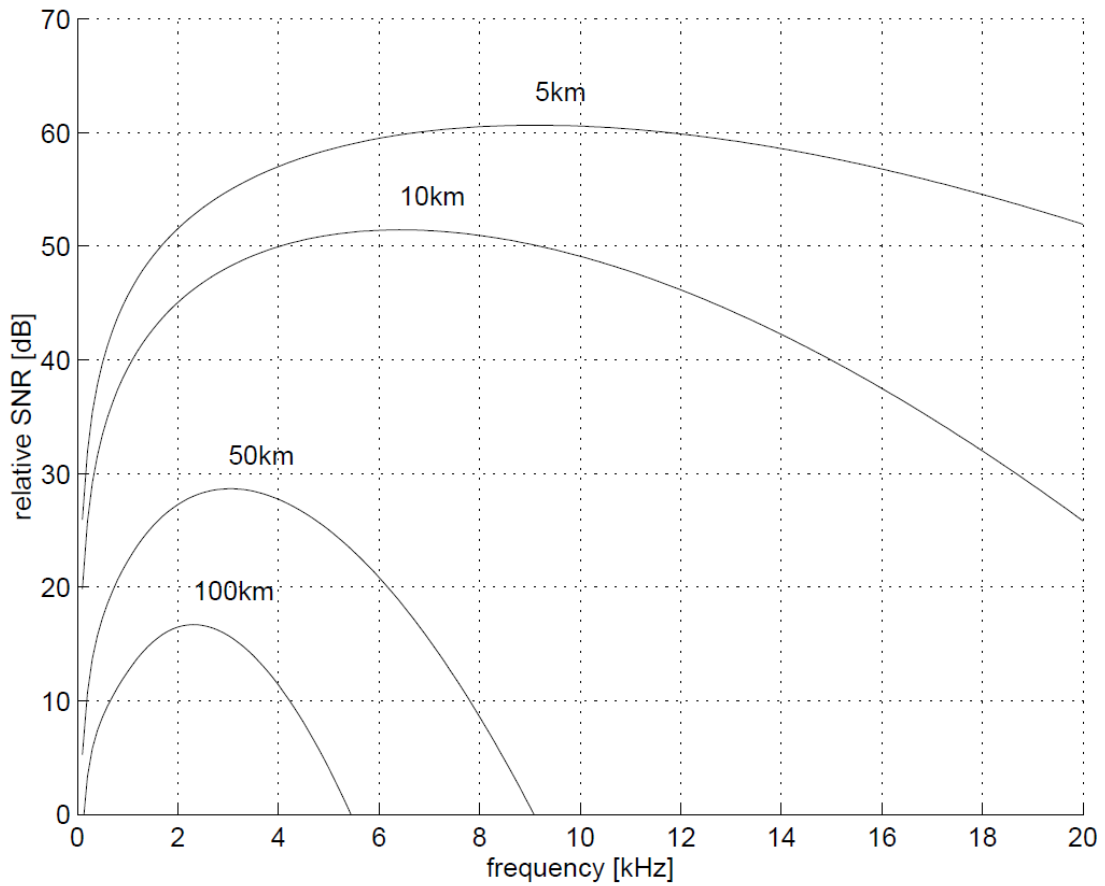
Figure 2.4: Narrow-band SNR variation with range and operating frequency in a typical marine acoustic environment (assuming spherical spreading, absorption according to Thorp [110]).

2.2.2 Multipath

Several ways of multipath propagation can be experienced depending on the system location with the structure of multipath varying with water depth, operating frequency and transmission range. Within those determine factors, it is mostly the water depth that determines the type of propagation. Although the definition of shallow or deep water is not strict, it usually implies the region of continental shelves (including inland environments such as rivers and lakes), with depth less than about 100 m, and the region past the continental shelves, respectively. Those two types of channel are commonly referred as horizon channel and vertical channel based on their geometry characteristics. In both scenarios, the fundamental mechanisms of multipath formation occur as reflections at boundaries (surface, bottom and any objects in the water) and ray bending (refraction) due to the fact that sound speed is a function of depth and rays of sound always bend toward regions of lower propagation speed. The relationship between sound velocity and the depth of operation is best illustrated below in Figure 2.5 [9], where zone 1 is typically within the range of 100m, zone 2 usually has the depth of couple hundred meters, and zone 3 covers the depth of 1km and beyond.
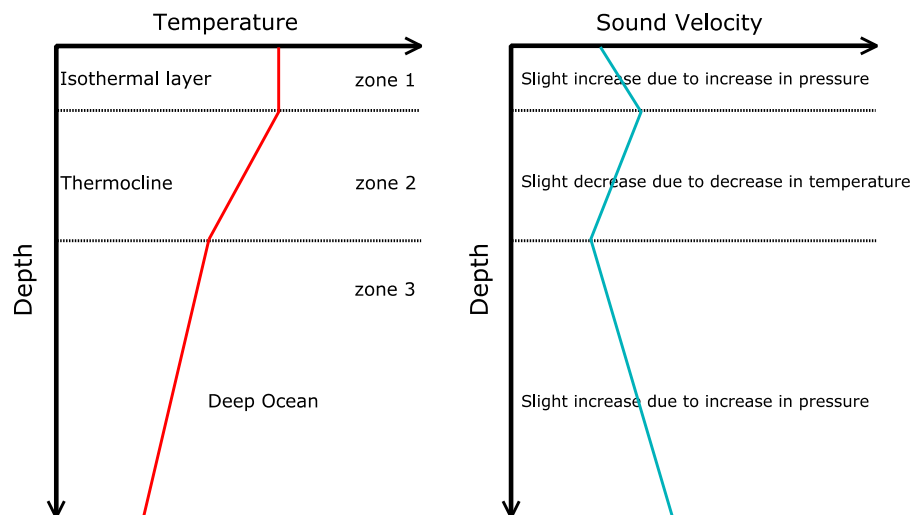
Figure 2.5: Velocity variation with depth due to change in water temperature and pressure.

In vertical channels, the sound propagation may form by bending of the rays towards the location where the sound speed reaches its minimum, known as the axis of the deep sound channel. Since there is little loss due to reflections, sound can travel over several thousands of kilometers. Alternatively, the rays bending upwards may reach the surface focusing in one point

where they are reflected, and this process is repeated periodically. The region between two focusing points on the surface forms a convergence zone, with a typical length span of 60 ~ 100 km [11]. The effect of ray bending is shown in Figure 2.6.
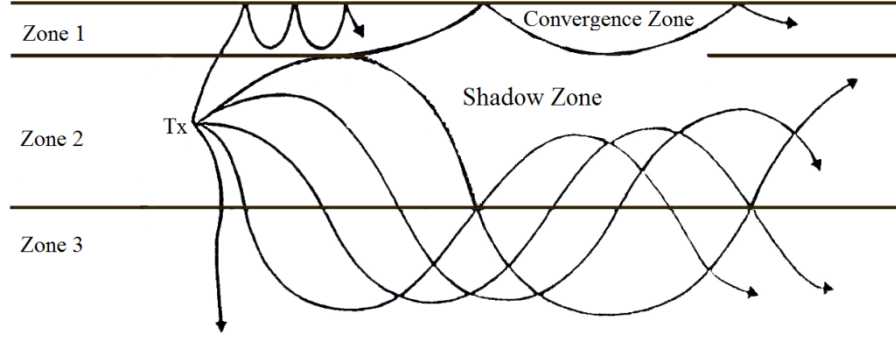
Figure 2.6: Effect of ray bending of sound transmitting in different depth regions subsea [12].

Conversely, horizontal channels experienced in shallow water are composed of surface-bottom bounces in addition to a possible direct path. The impulse response of such acoustic channel is determined by strong arrivals with their relative strengths and delays. An example of typical multipath experienced in horizontal shallow water channel is demonstrated in Figure 2.7.
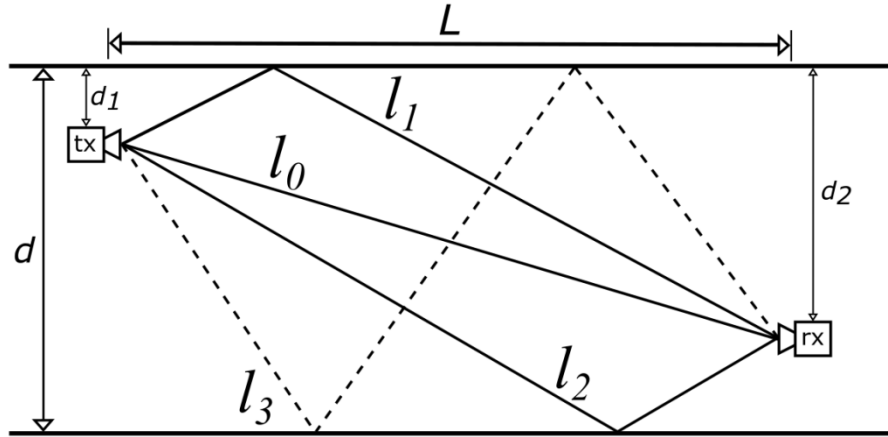
Figure 2.7: Multipath propagation in a shallow water channel.

For a multipath propagation shown in Figure 2.6, denote the length of the pth path as l_p, the path delay is obtained as l_p/c, where c denotes the sound speed in water. Define the arrival time of the first path (the strongest path may not be the first path) as t_0, therefore the relative path delays can be obtained as:

$$\tau_p = \frac{l_p}{c} - t_0 \tag{2.2.9}$$

14

The path magnitude can be represented using the reflection coefficient of the pth path Γ_p and the corresponding transmission attenuation A_p as:

$$h_p = \frac{\Gamma_p}{\sqrt{A_p}} \tag{2.2.10}$$

Adopting typical channel model in a radio channel, the channel impulse response for a multipath propagation with P paths can be expressed as:

$$h(t) = \sum_{i=1}^{P} h_i \delta(t - \tau_i) \tag{2.2.11}$$

According to (2.2.0), the path attenuation is a function of frequency. For a wideband signal, each frequency will experience a different amount of attenuation. As a result, the frequency response of the pth can be obtained:

$$H_p(f) = \frac{\Gamma_p}{\sqrt{A(l_p, f)}} \tag{2.2.12}$$

As shown in (2.2.12), each path of an acoustic channel has its own dispersion. As a result, the multipath propagation introduces frequency selectivity which puts a huge challenge for many UWA systems. Combining the frequency response of each path, the overall channel frequency response can be represented:

$$H(f) = \sum_{i=1}^{P} H_i(f) e^{-j2\pi f \tau_i} \tag{2.2.13}$$

The corresponding channel impulse response is expressed as:

$$h(t) = \sum_{i=1}^{P} h_i(t - \tau_i) \tag{2.2.14}$$

For a digital communication system, the formation of the received signal being a combination of components from different paths can be well modelled using a tapped delay line model. An example of a multipath channel with four paths is shown in Figure 2.8. The tap spacing D is calculated as the reciprocal of twice the channel bandwidth and the tap gains W modelled as stochastic process with certain distributions and power spectral densities.
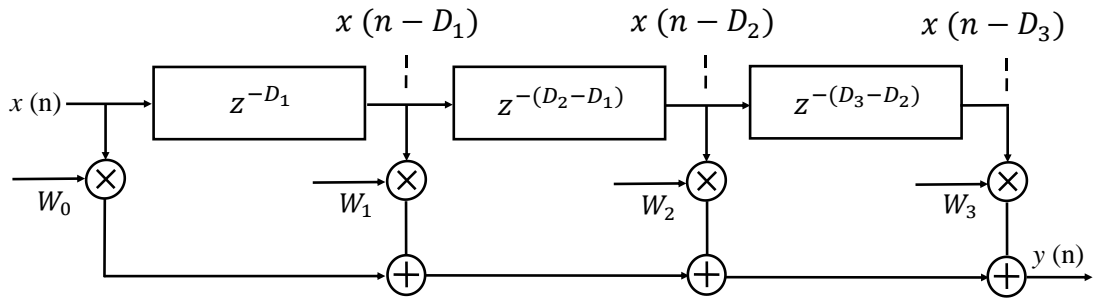
Figure 2.8: Tapped Delay Line Multipath Model

The combined signal with all delayed variants is modelled as:

$$y_n = W_0 x(n) + W_1 x(n - D_1) + W_2 x(n - D_2) + W_3 x(n - D_3) \tag{2.2.15}$$

Utilizing the tapped delay model, the channel's frequency selectivity can be visualized as demonstrated in Figure 2.9.
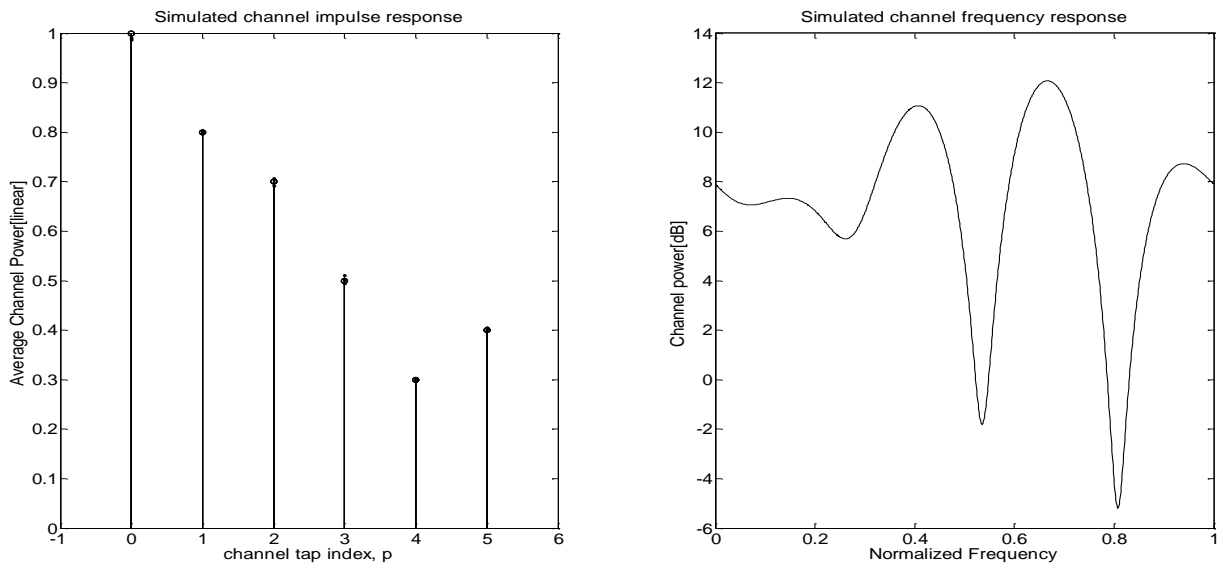
Figure 2.9: An example of a simulated UWA multipath channel utilizing a tapped delay line model with 6 arrivals and uniform tap spacing and its corresponding frequency response.

2.2.3 Time Variation

Along with each of the deterministic propagation paths (macro-multipath), which can be modelled accurately, there are random signal fluctuations (micro-multipath), which account for the time variability of the channel. The main contributing factors to a channel's variability come from inherent changes in the propagation medium and motion of the transmitter and receiver. While the inherent changes are often caused by slow alterations in the channel such as monthly

changes in temperature, the prominent contributor to the overall channel variability comes from surface waves, causing dislocation of the reflection point. The changes in reflection point result in not only scattering of the signal but also Doppler spread due to changes in path length. Surface scattering is determined by the condition of the water surface. For a smooth surface, a single incident on the surface would be reflected almost perfectly with the only deformation being the phase shifting. Unfortunately displacements do exist in most of the real life environments. Although the vertical displacement can be modelled as a zero-mean Gaussian variable with its power spectrum depending only on the wind speed [9], the frequency spreading caused by motion of the reflection point is difficult to track. Consider a single surface reflection incident at an angle of θ, the Doppler spread of the signal component with frequency f can be represented as [10]:

$$\Delta_f = \phi \frac{f}{c} \omega^{3/2} \cos \theta \qquad (2.2.16)$$

Where c is the speed of sound is underwater, ω is the wind speed in *m/s* and ϕ is the normalization factor with the value of 0.0175.

Although the study on both the deterministic and statistical modelling of sound propagation underwater has been carried on for many decades, the effort put into channel modelling only received more attention recently [13][14][15][16]. As stated in the previous section, the multipath propagation can be well represented using tapped-delay-line models. However, unlike radio channels where a number of models for both the probability distribution (e.g., Rayleigh fading) and the power spectral density of the fading process (e.g., the Jake's model) are well accepted and standardized, not a single model is widely accepted to date for any of the underwater acoustic channels. Conversely, one exception exists as for the shallow water medium range channel, most researchers consider it as fully saturated, meaning it exhibits Rayleigh fading [12] [13] [17]. On the other hand, the controversy of utilizing a statistical channel modelling still remains as [14] find out that both deep and shallow water channel fit better within a deterministic model while experimental results indicates that although some channels may just as well be characterized as deterministic, others can exhibit Rice or Rayleigh fading [18].

2.2.4 Doppler Effect

Along with the Doppler spread generated from random fluctuations on the reflection point on the surface, digital communication system in UWA channels may often experience Doppler Effect which causes frequency shifting together with additional frequency spreading. Owing to the relative motion between the transmitter and receiver, the distance which the received signal travels change accordingly. As a result, the beginning of the received signal may experience a different time delay comparing to the end of the same signal due to the change in path length. Considering a pulse signal $s(t)$ modulated onto a carrier frequency of f_c, for one received path and ignore the path attenuation, the received signal is

$$\text{U}(t_0 + t) = \text{u}(t_0 + t - \frac{d(t_0) - vt}{c}) \tag{2.2.17}$$

where $d(t_0)$ is the travelled distance of signal arriving at t_0 with a constant relative speed of v (i.e., no accelerations). Setting this time as reference, the received signal can be expressed using the transmitted pulse as

$$
\begin{aligned}
\text{r}(t) &= \text{u}(t_0 + at - \tau) \\
&= Re\{s[(1 + a)t - \tau]e^{j2\pi f_c[(1+a)t-\tau]}\}
\end{aligned}
\tag{2.2.18}
$$

Where $\tau = \frac{d(t_0)}{c} - t_0$. Also, the baseband received signal is

$$y(t) = e^{-j2\pi f_c\tau}s[(1 + a)t - \tau]e^{j2\pi a f_c t} \tag{2.2.19}$$

From (2.2.19) it is clear that the Doppler Effect is twofold. First it distorts the amplitude of the received signal by a factor of $(1 + a)$. This is equivalent to a scale of $1/(1 + a)$ on the signal duration. Secondly, it introduces a frequency offset of af_c. Those two types of distortion correspond to motion-induced Doppler spreading and Doppler shift respectively. The amount of Doppler distortion and its effect varies among applications. Due to the relatively slow (comparing to radio systems) speed which acoustic wave transmits subsea, the Doppler Effect is much more pronounced underwater. Even without intentional motion, relative velocity between transmitter and receiver still exist to a certain degree as instruments placed subsea are subject to drifting with waves, currents, and tides, which may even occur at comparable velocities to AUVs. The corresponding Doppler distortion introduced is rather erratic, making

it extremely difficult to track and compensate at the receiver. A comparison of such effect on different systems with varying propagation speed and relative speed is summarized in Table 2.1.

TABLE 2.1

Doppler Distortion on systems with different relative speed

	Mobile radio system	Stationary Underwater acoustic system	Underwater AUV system
Relative Speed	160 km/h	~0.1m/s	~2m/s
Amount of Distortion	1.5×10^{-7}	0.6×10^{-4}	1.2×10^{-3}
Type of Distortion	Continuous	Erratic	Continuous

As the Doppler spreading experienced in Radio systems is so small that the effect it has on the symbol synchronization can often be neglected. Therefore a simplified model is often adopted using an approximation $s[(1+a)t] \approx s(t)$. While in UWA systems, dedicate phase and delay synchronization is usually required in order to compensate for the detrimental effect of Doppler distortion.

2.3 State-of-the-Art: Underwater Acoustic Communication

A brief review of related research is presented, including the historical background of underwater acoustic communications and highlights of recent developments.

2.3.1 Historical Background

In order to overcome the challenging underwater acoustic communication channel, dedicated works have been investigated into this field since late 1980s. Before the recent focus of research in underwater acoustic multicarrier systems, extraordinary progress has been made in [8] [19-22]. Systems utilizing various modulation schemes have been investigated. Non-coherent detection of frequency shift keying (FSK) signals has been adopted in channels where rapid phase variation can be experienced. Such channels can often be found in shallow water medium and long-range transmissions. Systems implementing non-coherent modulation schemes often

require some sort of guard intervals to deal with the ISI which reduces the data throughput inevitably. Furthermore, as fading is correlated among frequencies separated by less than the coherence bandwidth, only frequency channels separated by more than this amount can be used at the same time, which further reduces the system efficiency. Although non-coherent modulation systems suffer from low spectrum efficiency, techniques such as non-coherent FSK still provides robust performance in applications where only moderate data rate is desired. Successful implementation including a telemetry system using a multiple FSK modulation technique operating in the frequency range of 20 kHz-30 kHz over a 3 km vertical channel and a 4 km shallow water horizontal path [19].

Conversely, coherent modulation schemes such as phase shift keying (PSK) and quadrature amplitude modulation (QAM) have received great attention since late 80's as systems with good bandwidth utilization are highly demanded in latest applications. Systems based on coherent modulation techniques are capable of achieving raw data throughputs that are an order of magnitude higher than those of the existing non-coherent systems. To simplify the carrier recovery of the transmitted sequence, differential phase shift keying (DPSK) systems are often preferred, encoding information in the relative phase change of adjacent symbols rather than from a known reference signal. However, due to the compromise between improved throughput and system complexity, recent developments have shifted towards fully-coherent communication schemes. Coherent modulation schemes have been tested in various underwater scenarios and achieved success in many channels with harsh conditions such as horizontal shallow water channels with large delay spread [8], however most commercial applications are still in vertical and very short range channels where minimal multipath and good phase stability can be expected [6]-[8] [24].

2.3.2 Receiver Design

Although coherent modulated systems can provide better bandwidth efficiency, the highly dynamic and dispersive multipath channel encountered in the real-world environments still puts a huge restraint on the performance. To mitigate such effects, recent research has been developed in areas such as large scale multi-element array receivers and the design of adaptive equalizers in addition to differentially coherent detection techniques in order to fully exploit the

potential of coherent systems. The development of adaptive equalizer structure such as Linear Equalizer (LE) and the Decision Feedback Equalizer (DFE) were considered as a significant turning point in applications of phase coherent transmission systems due to its ability in active Inter-Symbol-Interference (ISI) suppression. An early example of an adaptive equalizer was presented in [7] utilizing quadrature DPSK for transmitting of color images at a data rate of 16kbps through a 6.5km vertical channel. Another example was demonstrated in [6] utilizing a symbol spaced DFE and narrow beam transducers $(5°)$ across a 60m shallow water channel at 500kbps.

On the other hand, array processing can be adopted at both ends of the transmission for multipath suppression. [28] utilized transmitter array to generate a single path propagation using long arrays and precision positioning without any methods of equalization. This work was motivated by believing that the shallow water test channel exhibits Rayleigh fading hence no equalizer is fast enough to track the channel variability. A receiving array was employed instead to compensate for possible alignment errors. Conversely, a research group in Newcastle University investigated the possibility of multipath rejection using adaptive beamforming [29]. The beam former used a LMS algorithm to adaptively drive nulls towards the direction of a surface reflection. However the performance meets a threshold as the beam forming ability decreases rapidly with the increment of range against depth. [30] came up with the idea of applying a LMS type decision-feedback-equalizer in addition to beamforming to compensate for this detrimental effect. A separate waveform is transmitted alongside with twice the data rate for the purpose of timing synchronization. Data rate of 20kbps was successfully achieved with an estimated BER of 10^{-2}.

The state-of-the-art phase coherent detection system based on joint synchronization and equalization for compensating the effect of phase variations and ISI was developed in [8][31][32] utilizing a RLS type fractionally spaced DFE together with spatial combining to better utilize channel's timing and frequency diversity. Data of 2kbps and 40kbps are obtained across long range and shallow water medium-range channels. Table 2.2 listed some representative systems utilizing various forms of coherent receiver structures.

Table 2.2

Summary of Single Carrier Coherent Modulation Systems

$(f_c: Carrier\ Frequency, f_{band}: Bandwidth)$

Channel	Range	Data Rate	Receiver & Modulation	$f_c(f_{band})$	Equalizer	Ref
Horiz	60m	500kbps	Directional (5°), 16QAM	1MHz(250kHz)	DFE	[6]
Vertical	6500m	16kbps	Directional (80°), 4 DPSK	20kHz(8kHz)	LE	[7]
Vertical	2000m	19.2kbps	4 Element Array, 2 DPSK	53kHz(8kHz)	LE	[23]
Horiz	1000m	600bps	DSSS	30kHz(10kHz)	LE DFE	[24]
Horiz	1800m	15kbps	Directional (60°), QPSK	15kHz(8kHz)	DFE	[27]
Horiz	130m	20kbps	Directional (45), 4DPSK	50kHz(10kHz)	xxxx	[28]
Horiz	2000m	20kbps	7 Element Array, QPSK	49kHz(28kHz)	DFE	[30]

2.3.3 Multicarrier Transmissions

In recent years, orthogonal frequency division multiplexing (OFDM) represented multicarrier underwater acoustic communication systems have received a great deal of attention due to its ability of enabling high data rate transmission over long range dispersive channels. In OFDM systems, data stream is broken into multiple parallel streams and modulated on separate subcarriers. The allocated channel is simultaneously occupied through the transmission of subcarriers which divides the available bandwidth into multiple sub-bands. As a result, the detrimental effect of deep fading is alleviated as the deep fades only affect one or few sub-channels. This is best illustrated in Figure 2.10.
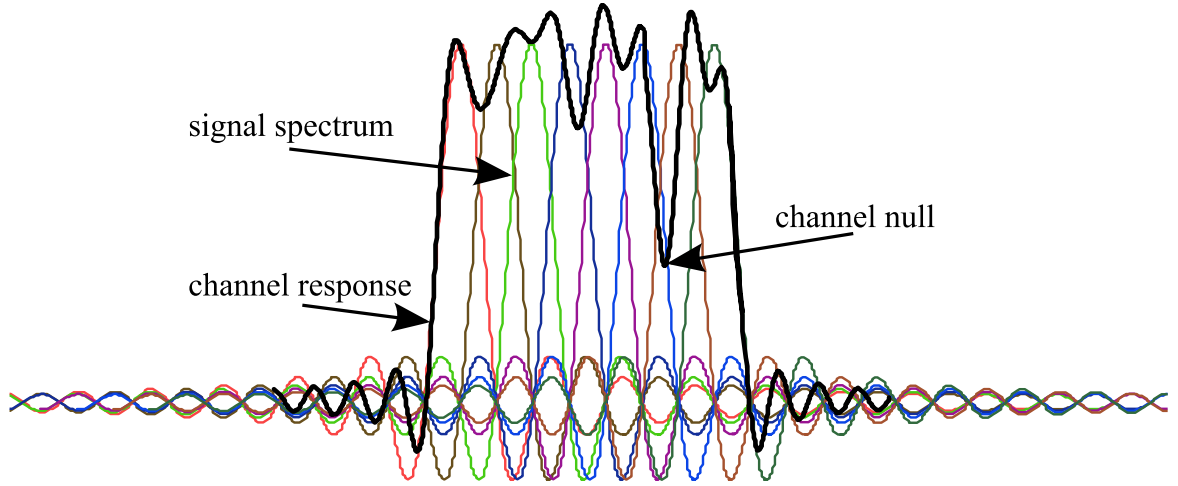
Figure 2.10. The effect of channel's frequency selectivity on OFDM systems.

Additionally, when the number of subcarrier is great enough, the dispersive channel can be considered as flat-fading on each of the sub-bands [33] which enables simple equalization at the receiver. The mathematic analysis of such properties is expressed next. Considering an OFDM system with N subcarriers, the signal transmitted on the kth subcarrier of frequency $f_k = f_0 + k\Delta f$ can be expressed as:

$$x_k(t) = Re\{d_k s(t)e^{j2\pi f_k t} = Re\{u_k(t)e^{j2\pi f_0 t}\} \tag{2.2.20}$$

where $s(t)$ is a pulse of unit amplitude with duration $T = \frac{N}{BW} = 1/\Delta f$ and d_k is the data symbol. The combined signal with bandwidth of Bw can then be expressed as:

$$x(t) = \sum_{k=0}^{N-1} x_k(t) = Re\{x_b(t)e^{j2\pi f_0 t}\} \tag{2.2.21}$$

Where x_b is the baseband transmitted signal. For efficient utilization of bandwidth, the number of subcarriers N has to be large enough. Hence we can assume that the channel's frequency response of pth path $H_p(f) \approx H_p(f_k)$ for $f \in [f_k - \Delta f/2, f_k + \Delta f/2]$. Also, if Δf is small enough, the narrowband assumption is justified. Therefore, the received signal is:

$$y(t) = \sum_{k=0}^{N-1} \sum_{i=1}^{P} H_i(f_k) x_k(t - \tau_i) = Re\{y_b(t)e^{j2\pi f_0 t}\} \tag{2.2.22}$$

Adopting the channel response in (2.2.11), the received signal can be simplified (ignore the effect of ambient noise) as:

$$y(t) = \sum_{i=1}^{P} h_i x(t - \tau_i) \qquad (2.2.23)$$

And the corresponding baseband received signal is:

$$y_b(t) = \sum_{k=0}^{N-1} d_k \left[\sum_{i=1}^{P} H_i(f_k) e^{-j2\pi f_k \tau_i} s(t - \tau_i) \right] e^{j2\pi k \Delta f t} \qquad (2.2.24)$$

Apply the fast Fourier transform (FFT) on the baseband received signal, we have:

$$Y_k(f) = \frac{1}{T} \int_{\widetilde{\tau_0}}^{T+\widetilde{\tau_0}} y_b(t) e^{-j2\pi k \Delta f t} dt$$

$$= H(f_k) d_k \qquad (2.2.25)$$

Where $\widetilde{\tau_0}$ is the estimated delay spread and T_g represents the guard interval and it is chosen so that $T_g > \tau_0$. In order to recover the transmitted signal d_k, a simple frequency domain channel equalization can be performed based on (2.2.25) with an estimated frequency response $\widetilde{H(f_k)}$.

Although OFDM systems have the advantage of great bandwidth efficiency and simple frequency domain equalization, it is prone to distortions introduced from Doppler Effect. Different from OFDM radio systems where the Doppler spread appeared as amplitude scaling can often be neglected and the Doppler shift can be assumed equal for all subcarriers, in UWA OFDM systems each sub-band experiences a different amount of Doppler shift due to the wideband nature of the channel, making it extremely difficult to track and compensate at the receiver. This effect is demonstrated in Figure 2.11.

In order to compensate for the wideband Doppler Effect, [34] introduced an OFDM system with the ability of compensating non-uniform Doppler shifts. This system is further developed into a Multi-Input-Multi-Output (MIMO) OFDM structure which achieved data rates of up to 125kbps across ranges of couple hundred meters in a particular hostile environment in [35].
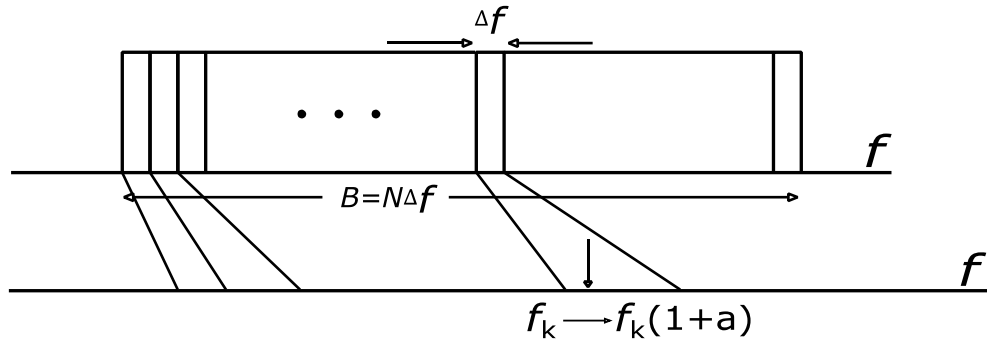
Figure 2.11. Doppler shift on a wideband system.

On the other hand, various modified OFDM schemes have been developed in order to exploit its full potential. Zero-padded OFDM introduced in [37] is considered as an interesting alternation to the conventional OFDM utilizing cyclic prefix. With the aid of frequency-domain oversampling [38], zero-padded OFDM achieves better transmission efficiency with less power consumption at the cost of increased computational complexity. Furthermore, orthogonal signal-division multiplexing (OSDM) was proposed in [39] which increase the transmission efficiency, as it measures the multipath profile without any adaptation or interpolation process. Through comparison to existing single-carrier Recursive Least Square Decision Feedback Equalizer (RLS-DFE) and OFDM systems, OSDM system is concluded as a reliable transmission scheme for UWA channels with multipath and Doppler spread. In order to further increase the transmission of OFDM systems, a guard-free OFDM transmission scheme is utilized in [111] [112] where demonstration of experimental data was achieved without any guard interval (such as cyclic prefix or zero padding) and with a superimposed pilot. In addition to the vulnerability to Doppler shifts, OFDM also suffers from its high peak-to-average-power ratio (PAPR). Conversely, OFDM systems based on Discrete Cosine Transform (DCT) are proven to provide higher PAPR reduction and better noise immunity than standard OFDM systems [39]. As the bandwidth required for DCT is only half the amount for discrete Fourier Transform (DFT) with the same number of subcarriers, better bandwidth utilization can be achieved. Additionally, the calculation speed of orthogonal components is increased three folds while the implementation size is reduced to half as compared to fast FFT based design [40]. Similarly, Walsh-Hadamard Transform (WHT) was introduced into OFDM systems as a pre-transform due to its ability of suppressing the high PAPR as it lowers autocorrelation property of the input signal [42]. In [43] a T-transform based OFDM is proposed where it combines the

WHT and the DFT into a single fast orthogonal transform which increases the channel diversity order without sacrificing any throughput. The performance of WHT OFDM in UWA channels is verified in [41] with comparison to DCT OFDM and conventional OFDM.

The current research focus on multicarrier transmission in UWA channels include overcoming variations in Doppler shift in highly mobile systems [44], design of systems utilizing novel time domain synchronization techniques in order to increase transmission efficiency [45], data rate maximization and system margin maximization through adaptive bit and power loading [46], and the design on novel coding and sparse equalization techniques [47] [48].

2.4 Chapter Conclusion

This chapter presented an overview on underwater acoustic communications starting with a selection of transmission mechanisms. Acoustic wave is considered as the most suited information carrier for medium to long range wireless communication through exploring the physical characteristics of the channel. The dominant difficulties encountered in transmitting wirelessly underwater are analyzed, which are the constraint on transmitting power; selectivity of the channel including multipath and Doppler Effect and ambient noise. A brief review on research milestones conducted through the years in the form of phase coherent and non-coherent transmissions is given. The state-of-the-art coherent systems utilizing multi element receiver arrays combined with adaptive equalizer has demonstrated the capability of robust transmission in medium to long shallow water channels with a data rate of up to 20kbps [49]. Additionally, OFDM represented multicarrier transmission systems are demonstrated to be inherently superior in terms of multipath resilience and reduction in receiver complexity [5].

The remaining chapters explain the development of a novel WHT-OFDM communication system offering better tolerance in double selective fading channels without any loss in throughput [41]. Specific focus is paid on the challenges of suppressing the detrimental noise enhancement in WHT-OFDM systems with equalizer design, and the search and implementations on optimal PAPR reduction techniques.

CHAPTER 3

OFDM and T-transformed OFDM

This chapter presents the basic ideas of OFDM and its expansion to T-transformed OFDM, including basic structures, computational costs, and fundamental principles about the fast transforms involved and their merits and challenges when utilized in UWA channels.

3.1 Multi-carrier Transmission

3.1.1 Basic Structure of a Multi-Carrier Scheme

Frequency selective fading is commonly experienced in wideband UWA communications. In multicarrier transmission systems, the available bandwidth is divided into multiple sub-bands, therefore on each sub-band, the channel can be considered as flat fading. The basic structure for multi-carrier transmission is demonstrated in Figure 3.1. As illustrated in Figure 3.1 a wideband signal is first converted in to a parallel stream of narrowband signals via a narrowband filter bank $H_k(f)$. The result signal is combined after and sent through a frequency selective channel. With the matching filter bank at the receiver, the frequency selective channel can be approximated by multiple narrowband flat fading channels. The process of converting a frequency selective fading channel into multiple flat-fading sub-channels is depicted in Figure 3.2.
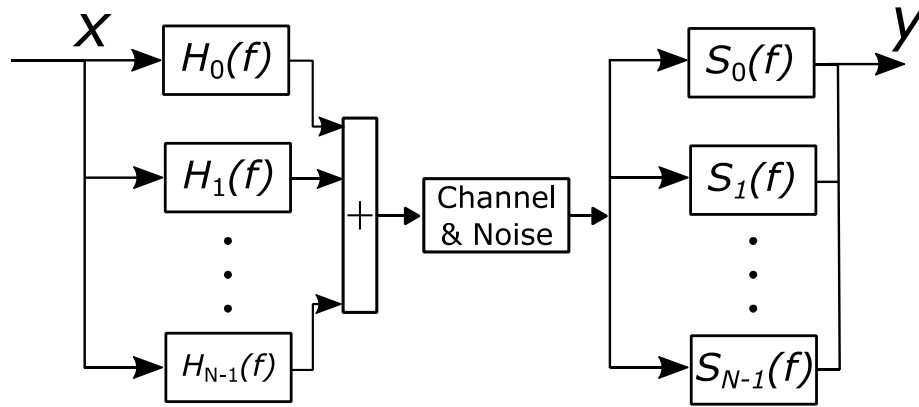
Figure 3.1 Basic structure of a multi-carrier transmission system.
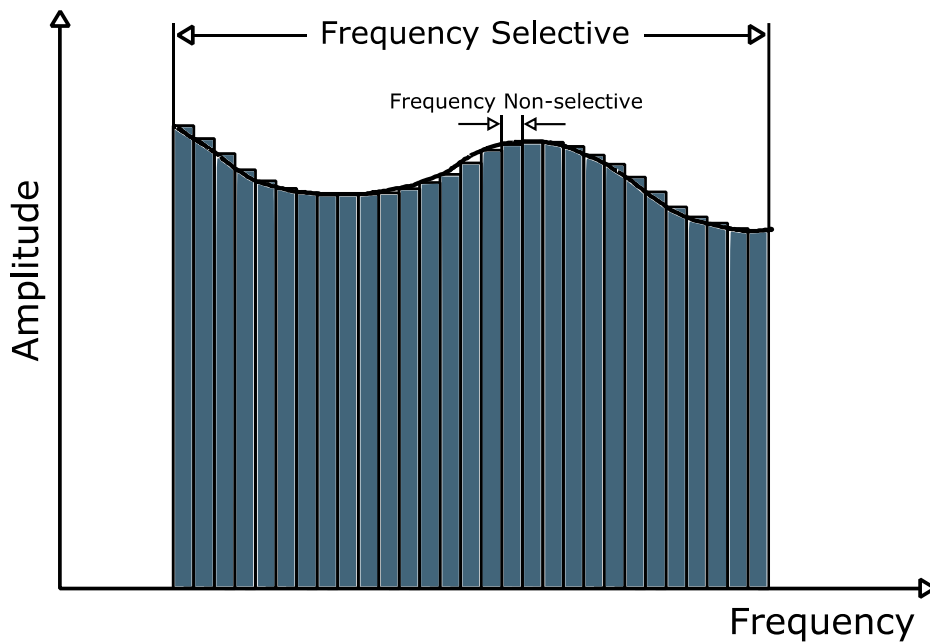
Figure 3.2 Frequency response of a multi-channel transmission system.

Moreover, the approximation of flat fading on narrowband channels enables simple equalization. As long as the neighboring channels are not overlapped, distortion less transmission can be achieved [50].

3.1.2 OFDM Transmission Scheme

Orthogonal frequency division multiplexing (OFDM) transmission scheme is another variant of multi-channel systems where information is conveyed by multiple subcarriers. Unlike conventional frequency division multiplexing transmissions, the spectra of individual OFDM sub-bands are overlapped hence allowing better bandwidth utilization, as long as the orthogonality between sub-bands are maintained. The overlapped subcarriers can be generated

via inverse discrete Fourier transform (IDFT) at the transmitter and its corresponding pair DFT at the receiver. Conversely, fast FFT and inverse FFT are often adopted instead in commercial systems for the sake of computational efficiency. The general transmission process for an OFDM system in a noisy environment is depicted as follows. Firstly the transmitted symbols $\{X_l[k]\}_{k=0}^{N-1}$ are sent through an N-point IFFT to generate the time-domain summed signal of N subcarriers $\{x[n]\}_{n=0}^{N-1}$. After being corrupted by the zero mean additive noise $w[n]$, the received signal $y[n]$ is denoted as $y[n] = x[n] + w[n]$. Taking the N-point FFT of the received samples $\{y[n]\}_{n=0}^{N-1}$, the noisy version of the transmitted symbols $\{Y_l[k]\}_{k=0}^{N-1}$ can be obtained at the receiver. The above OFDM transmission structure implemented by IFFT/FFT is shown in Figure 3.3.
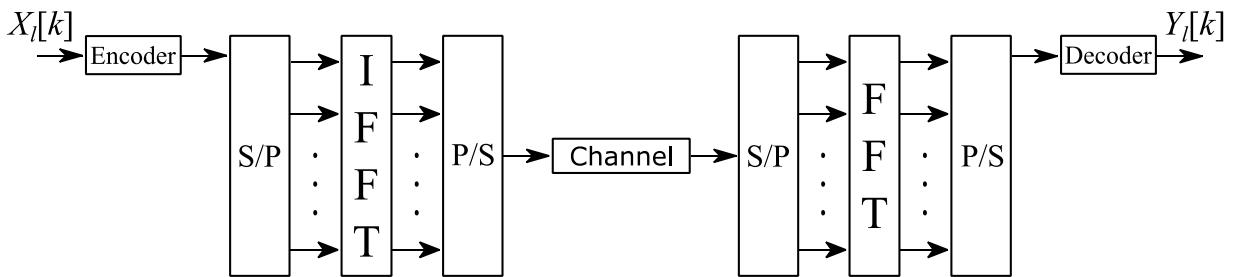
Figure 3.3 A basic OFDM transmission scheme implemented using IFFT/FFT.

Additionally, OFDM scheme often require inserting a guard interval or some sort of guard band in the time domain in order to mitigate the ISI between OFDM symbols. The guard band, cyclic prefix (CP), is added by copying the last part of the OFDM symbol and appending it at the beginning of the OFDM symbol in order to compensate for the time dispersion induced from multipath effect. The ISI can be eliminated by choosing a CP of length equal to or larger than the maximum path delay of the channel. Moreover, due to the insertion of cyclic prefix, the transmitted OFDM symbols are cyclically extended into the guard interval, which makes the transmitted data stream appears periodic. Therefore the effect of the time dispersion becomes equivalent to a cyclic convolution. Details of guard intervals are further explained in section 3.2.3.

The basic principles of OFDM transmission systems is examined first in the next section.

3.2 Basic Principles of OFDM Systems

3.2.1 OFDM Modulation and Demodulation

According to the basic OFDM transmission scheme shown in Figure 3.3, the process for OFDM modulation and demodulation can be expressed mathematically as follows. Consider a stream of OFDM symbols, the information is first converted into N parallel streams. Each of N symbols from serial-to-parallel (S/P) conversion is carried out separately by multiple subcarriers. Let $X_p[k]$ denote the pth transmit OFDM symbol (assume M symbol in total) on the kth subcarrier with $p = 0,1,2..M-1$ and $k = 0,1,2...,N-1$. Note that the duration for transmission of N OFDM symbols is now extended to NT_s which forms a single OFDM symbol with a length $T_{sym} = NT_s$. For demonstration purposes, guard-interval is omitted here for the sake of simplicity. Therefore the pth OFDM signal at the kth subcarrier is given as:

$$\Psi_{p,k}(t) = \begin{cases} e^{j2\pi f_k(t-pT_{sym})}, & 0 < t \leq T_{sym} \\ 0, & otherwise \end{cases} \tag{3.2.0}$$

The corresponding continuous baseband and passband OFDM signals can be expressed respectively as:

$$x_p(t) = \sum_{p=0}^{\infty} \sum_{k=0}^{N-1} X_p[k] \, e^{j2\pi f_k(t-pT_{sym})} \tag{3.2.1}$$

$$x_p(t) = Re\left\{ \frac{1}{T_{sym}} \sum_{p=0}^{\infty} \left(\sum_{k=0}^{N-1} X_p[k]\Psi_{p,k}(t) \right) \right\} \tag{3.2.2}$$

By sampling the continuous baseband OFDM signal at a sampling period $t = pT_{sym} + nT_s$ where $T_s = T_{sym}/N$ and $f_k = k/T_{sym}$, the corresponding discrete-time OFDM symbol can then be obtained as:

$$x_p[n] = \sum_{k=0}^{N-1} X_p[k]e^{\frac{j2\pi kn}{N}}, for \ n = 0,1,...,N-1 \tag{3.2.3}$$

Following the modulation process, the demodulation process is demonstrated next. Consider the received baseband OFDM symbol $y_p(t) = \sum_{k=0}^{N-1} X_p[k]e^{j2\pi f_k(t-pT_{sym})}, pT_{sym} < t \leq$

$pT_{sym} + nT_s$, the transmitted symbol can be reconstructed utilizing the orthogonality among the subcarriers via FFT:

$$
\begin{aligned}
Y_p[k] &= \sum_{n=0}^{N-1} y_p[n]e^{-j2\pi kn/N} \\
&= \sum_{n=0}^{N-1} \left\{ \frac{1}{N} \sum_{i=0}^{N-1} X_p[i]e^{j2\pi in/N} \right\} e^{-j2\pi kn/N} \\
&= \frac{1}{N} \sum_{n=0}^{N-1} \sum_{i=0}^{N-1} X_p[i]e^{j2\pi(i-k)n/N} \\
&= X_p[k]
\end{aligned}
\tag{3.2.4}
$$

From (3.2.4) it is obvious that the transmitted symbols can be recovered as long as the orthogonality of OFDM symbols is retained. However, due to the long delay spreads introduced from the multipath transmission in UWA channels, retaining the orthogonality is often considered as a challenging task in UWA OFDM systems. The effect of multipath and the delay spreads it generated are analyzed next.

3.2.2 Multipath Effect in OFDM systems

Consider the pth OFDM symbol $x_p(t)$, the received signal corrupted by a channel with an impulse response of $h_p(t)$ and additive noise $w_p(t)$ can be represented as:

$$
\begin{aligned}
y_p(t) &= x_p(t) * h_p(t) + w_p(t) \\
&= \int_0^\infty h_p(\tau)x_p(t-\tau)dt + w_p(t), T_{sym} < t \le pT_{sym} + nT_s
\end{aligned}
\tag{3.2.5}
$$

The discrete-time domain signal can be obtained at sampling intervals $nT_s = nT_{sym}/N$ as:

$$
\begin{aligned}
y_p[n] &= x_p[n] * h_p[n] + w_p[n] \\
&= \sum_{m=0}^\infty h_p[m]x_p[n-m] + w_p[n]
\end{aligned}
\tag{3.2.6}
$$

where $x_p[n] = x_p(nT_s)$, $y_p[n] = y_p(nT_s)$, and $w_p[n] = w_p(nT_s)$.

Denote the duration of the effective OFDM symbol without any guard interval as T_{sub}. As the bandwidth can be represented as $= 1/T_s$, therefore the frequency spacing Δf and symbol

duration T_{sub} can be represented as $\Delta f = \frac{BW}{N} = \frac{1}{NT_{sym}}$ and $T_{sub} = NT_s = 1/\Delta f$, respectively. By extending the symbol duration by N times the effect of the multipath fading will have less effect on OFDM symbols. However for a channel with extreme long delay spreads (which is commonly encountered in UWA channels), the effect of multipath fading may still break the orthogonality among OFDM subcarriers. Hence some form of guard interval is always required for successful demodulation in order to reduce the inter-symbol interface.

3.2.3 Guard Intervals

Two types of guard intervals are commonly used in OFDM systems. One is filling the spacing between successive OFDM symbols with zeroes (zero padding technique) and the other is by cyclically extending an OFDM symbol by copying the last samples of the previous symbol (cyclic prefix). Both techniques have their strengths and limitations. Zero padding technique allows for a simple application at the transmitter and saving of the transmitting power by transmitting literately nothing in the guard period. Conversely it requires a complex overlapping and adding process at the receiver in order to recover the transmitted information. On the other hand, systems utilizing CP as guard interval appears periodic and the effect of the time dispersion becomes equivalent to a cyclic convolution, which allows for simple equalization at the receiver. The structure of OFDM symbols utilizing CP is shown in Figure 3.4.
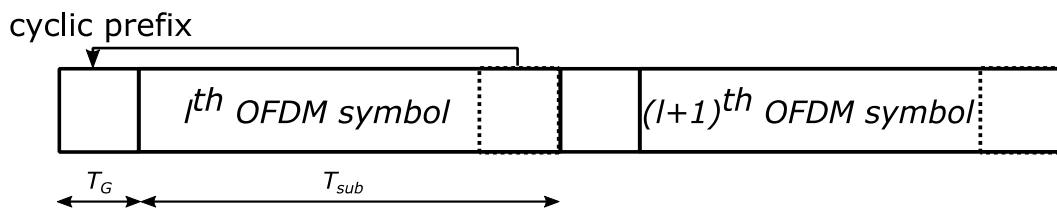
Figure 3.4 OFDM symbols structure with CP.

In order to compensate for the delay spread, the length of CP must be as least equal to or greater than the delay spread. With CP inserted, the corresponding demodulation process of the received OFDM symbol $\{y_p[n]\}_{n=0}^{N-1}$ utilizing FFT become:

$$Y_p[k] = \sum_{n=0}^{N-1} y_p[n]e^{-j2\pi kn/N}$$

$$= \sum_{n=0}^{N-1} \left\{ \sum_{m=0}^{\infty} h_p[m]x_p[n-m] + w_p[n] \right\} e^{-j2\pi kn/N}$$

$$= \sum_{n=0}^{N-1} \left\{ \sum_{m=0}^{\infty} h_p[m] \left\{ \frac{1}{N} \sum_{i=0}^{N-1} X_p[i]e^{j2\pi i(n-m)/N} \right\} \right\} e^{-j2\pi kn/N} + W_p[k] \qquad (3.2.7)$$

$$= \frac{1}{N} \sum_{i=0}^{N-1} \left\{ \left\{ \sum_{m=0}^{\infty} h_p[m]e^{-j2\pi im/N} \right\} X_p[i] \sum_{n=0}^{\infty} e^{-j2\pi(k-i)n/N} \right\} e^{-j2\pi kn/N}$$
$$+ W_p[k]$$

$$= H_p[k]X_p[k] + W_p[k]$$

Where $X_p[k], Y_p[k], H_p[k]$, and $W_p[k]$ denote the kth subcarrier frequency response of the pth transmitted symbol, received symbol, channel frequency response, and FFT of the channel noise, respectively. The simple equalization enabled by CP insertion is clearly shown in the last identity of (3.2.7) where in low noise scenarios $Y_p[k] \cong H_p[k]X_p[k]$ and the transmitted symbol can be detected by one-tap equalization which simply divides the received symbol by the channel frequency response (i.e. $X_p[k] \cong Y_p[k]/H_p[k]$. Note that without CP, $Y_p[k] \neq H_p[k]X_p[k]$ as $DFT\{Y_p[k]\} \neq DFT\{X_p[k]\} \cdot DFT\{H_p[k]\}$ when $y_p[n] = x_p[n] * h_p[n]$, where * denotes the convolution operation; however $Y_p[k] = H_p[k]X_p[k]$ when $y_p[n] = x_p[n] \otimes h_p[n]$ where $\otimes$ denotes the circular convolution.

3.3 OFDM Merits and Challenges

The strengths and weakness of OFDM represented multicarrier modulation is summarized in this section.

3.3.1 Merits

The main advantages of the OFDM technique are listed as follows:

1. *Robustness against Frequency Selective Fading Channel with Simple Channel Equalization*

   In single carrier systems, adaptive equalization techniques with relatively high cost and complexity are required to compensate for the channel effect. Such techniques of channel equalization become difficult to realize and provide inferior performance when the symbol

period becomes shorter with the increased data rate due to an increase in the number of adjacent symbols affected by a single fade. Conversely, in multicarrier systems, the entire available bandwidth is divided into many narrow-band subcarriers. Hence the frequency selective channel can be regarded as flat fading in each sub-band. In such cases, each subcarrier experiences flat fading which can be simply compensated utilizing one-tap equalizer.

2. *Robust to Weak Impulse Noise*

OFDM technique has been widely adopted in many UWA systems, however the performance of such systems has drastically deteriorated as a result of the man-made noises, namely, impulse noise further to AWGN. Due to the utilization of DFT at the receiver, the energy of impulse noise will spread over large number of subcarriers. In addition, due to the long duration of OFDM symbols transmitted over the impulsive channel, the majority of the transmitted information can still be recovered since only a small fraction of each symbol is contaminated by noise. Therefore, extra immunity against impulsive noise is provided.

3.3.2 Challenges

On the other hand, there are certain drawbacks that have a deleterious ramification on the performance of OFDM systems. A selection of the main impairments are addressed below:

1. *Sensitivity Against Deep Fading Channel*

Although OFDM systems provide a certain degree of robustness against frequency selective fading, some subcarriers will still be severely attenuated by deep fades. In such scenarios, OFDM does not offer any improvement in performance since no diversity can be exploited in order to recover the attenuated subcarriers. In recent studies, many techniques have been investigated to increase its resilience to the negative effects of multipath channel dispersion, such as channel coding, adaptive systems and better utilization of channel diversity; although at the cost of added extra cost of computational complexity and data rate sacrifice.

2. *High Peak-to-Average Power Ratio (PAPR)*

One of the major drawbacks of OFDM is its high PAPR. Due to the overlapping subcarriers enabled by IFFT, the peak power of the transmitted signal can be considerably higher compared to its average power. Although occurring only with a low probability, such large peaks still have negative ramifications for the overall system. For instance, to cope with high peak signal, the transmitter power amplifier (PA) requires large linear range, which adds a limitation on the selection of equipment, not to mention the added cost. Furthermore, the PA working in its nonlinear range causes in-band distortion and out-of-band radiation, which may lead to BER degradation and severe interference with the signals transmitted in

adjacent frequency bands.

3. Frequency Offset

In OFDM systems, the ability of suppressing the ISI and ICI introduced from channel is greatly relied on maintaining the orthogonality between subcarriers. However, the carrier frequency mismatch between the transmitter and receiver local oscillators, caused by Doppler effects due to relative motion between the transmitter and receiver, causes frequency offset which greatly degrades the performance of such systems. In this thesis, the Doppler Effect is measured by observing the packet compression/dilation and corrected by sampling rate conversion as in [107].

In order to overcome the above mentioned drawbacks, different techniques have been proposed through the years to make OFDM systems a more valid choice in UWA communication systems. In this thesis, we focus on improve the fast transform utilized in OFDM systems and developing the corresponding sub-systems to work with it. The details of OFDM systems with fast transforms are presented in the next section.

3.4 OFDM Systems with Fast Transforms

Processes describing the conversion of a sequence of information from one domain to another with or without acceptable levels of losses can be defined as a transform [52]. In the meantime, in the case of a fast transform, similar processes can be implemented with lower arithmetic operation by omitting the redundancy of same arithmetic. There are various transforms that are used widely for different engineering applications, such as Discrete Fourier Transform, Walsh-Hadamard Transform, Hartley Transform, Hilbert Transform, Number Theoretic Transform, Fermat Number Transform, and so on. For OFDM systems and the proposed application, this section focuses only on DFT and WHT.

3.4.1 Walsh-Hadamard Transforms (WHT)

The implementation of WHT in the field of well-formulated applications, such as nonlinear problems began in early 1960's with the works by Correngton [55] and Weiser [56]. In the field of signal processing, successful implementation has been achieved in [57] [58]. The Walsh transform can be defined by the Walsh matrix

$$W(n) = \overset{n}{\underset{i=2}{\otimes}} W(2) \qquad\qquad (3.4.1)$$

Where $\otimes$ denotes the Kronecker product and

$$W(2) = \begin{bmatrix} 1 & 1 \\ 1 & -1 \end{bmatrix} \qquad\qquad (3.4.2)$$

Which is the basic Walsh matrix. As depicted in (3.4.11), $W(n)$ is generated by the Kronecker product, hence the Walsh functions (rows of $W(n)$) appear in the Hadamard order (detailed in [62]). Since $W(n)$ is a self-inverse matrix up to the scalar 2^{-n}, the inverse Walsh transform is defined as

$$W^{-1}(n) = 2^{-n}W(n) \qquad\qquad (3.4.3)$$

The Walsh spectrum $S_{f,h} = [S_{f,h}(0), S_{f,h}(1), \dots, S_{f,h}(2^n - 1)]^T$ of a function $f\colon C_2^n$, specified by the function vector $F = [f(0), f(1), \dots, f(2^n - 1)]^T$, is defined as

$$S_{f,h} = W(n)F \qquad\qquad (3.4.4)$$

The spectral coefficients appear in Hadamard ordering, which is indicated by the index h in $S_{f,h}$. The function f is then reconstructed from the Walsh spectrum as

$$F = 2^{-n}W(n)S_{f,h} \qquad\qquad (3.4.5)$$

As a result the Walsh transform pair is formed by (3.4.14) and (3.4.15).

3.4.4 Fast Walsh Transform

The computation of the Walsh transform based on its definition (3.4.14) is inefficient as it expresses the $O(N^2)$ time complexity, where $N = 2^n$ is the size of the input vector. There, a more efficient algorithm, the Fast Walsh transform (FWT) with the time complexity of $O(N \log N)$ is introduced and usually used as a replacement of the original Walsh transform [63] [64]. The FWT can be defined by using the following factorization [64]

$$W(n) = \prod_{i=1}^{n} C_{w_i}(n)_i \qquad\qquad (3.4.6)$$

Where

$$C_{w_i}(n) = \overset{n}{\underset{j\,=\,1}{\otimes}} C_{w_i}^j(1)$$

$$C_{w_i}^j(1) = \begin{cases} W(1), i = j \\ I(1), i \neq j \end{cases}$$

(3.4.7)

The matrix $C_{w_i}(n)$ defines the partial Walsh transform and corresponds to the i-th step of the FWT.

3.4.5 Convolution Theorem

The convolution theorem in Fourier analysis states that the Fourier transform of the convolution function $C = f * g$ is the component product of the Fourier transforms of f and g, thus $S_{f*g} = S_f \cdot S_g$. On the other hand, WHT can operate in conjunction with DFT in the case of certain properties that have previously mentioned, such as orthogonality, Parseval's theorem and symmetry. However, circular convolution theorem cannot be accomplished with WHT. Alternatively, dyadic convolution theorem can be applied with WHT. As established in [59], the WHT of the product of two sequences is equivalent to the dyadic convolution of their WHT. For functions on the finite group C_2^n, the computation of the dyadic convolution through the application of the convolution theorem is conducted as:

$$C_{f*g} = 2^{-n}W^{-1}(n)((W(n)F)(W(n)G))$$

(3.4.8)

Therefore, an efficient algorithm for the computation of the dyadic convolution can be developed in terms of the FWHT, an example is given below in Figure 3.5 with n=2, N=4.
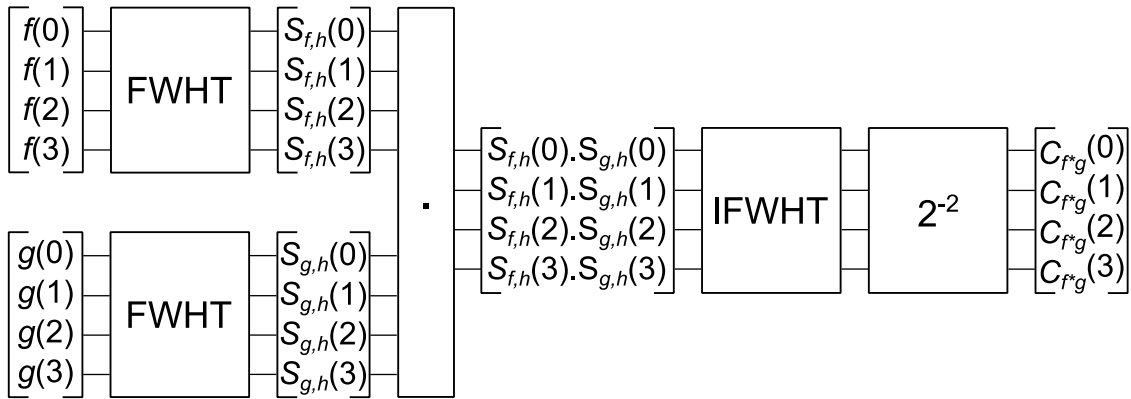
Figure 3.5 Dyadic convolution for n=2, N=4.

The simplified dyadic convolution for WHT can be represented as

$$W[X1.X2] = WX1 \overline{\otimes} WX2 \tag{3.4.9}$$

Where X1 and X2 are any two vectors of discrete data in the frequency domain, and $\overline{\otimes}$ stands for the dyadic convolution. Furthermore, WHT elements can be calculated by,

$$W_N^{k\widehat{m}} = \frac{1}{\sqrt{N}} (-1)^{\sum_{\hat{r}=0}^{\log_2 N-1} k_{\hat{r}} \widehat{m}_{\hat{r}}} \tag{3.4.0}$$

Where $\frac{1}{\sqrt{N}}$ is the normalization factor, $k_{\hat{r}}$ and $\widehat{m}_{\hat{r}}$ are the bits representation of the integer values k and $\widehat{m}$. The normalization factor is utilized with WHT to construct identical matrices in both forward and inverse WHT.

3.4.6 WHT in Matrix Form

The normalized size N inverse WHT (IWHT) matrix can be constructed using lower order matrices as

$$W_N = \overbrace{W_2 \otimes W_2 \otimes \ldots \otimes W_2}^{n} \tag{3.4.11}$$

Where $N = 2^J$, J is an integer value, $\otimes$ denotes the Kronecker product, and matrix W_2 defines the 2-points of the Walsh-Hadamard matrix, which can be written as

$$W_2 = \begin{bmatrix} 1 & 1 \\ 1 & -1 \end{bmatrix} \tag{3.4.12}$$

The size N WHT matrix can be written as a function of lower order matrices as

$$W_N = \frac{1}{\sqrt{N}} \begin{bmatrix} W_{\frac{N}{2}} & W_{\frac{N}{2}} \\ W_{\frac{N}{2}} & -W_{\frac{N}{2}} \end{bmatrix} \tag{3.4.13}$$

3.4.7 WHT Computational Complexity

The direct implementation of a WHT matrix requires $N(N-1)$ complex additions. On the other hand, following the fast implementation represented by the flowcharts structure of WHT in Figure 3.6, there are $\log_2 N$ stages, and an *N/2* butterfly per stage. Therefore, the total butterflies required to implementation a size $N \times N$ WHT matrix is $\frac{N}{2} \log_2 N$. For each

butterfly implementation, two complex additions are required. Consequently, the total number of complex additions required to implement a size $N \times N$ WHT matrix is
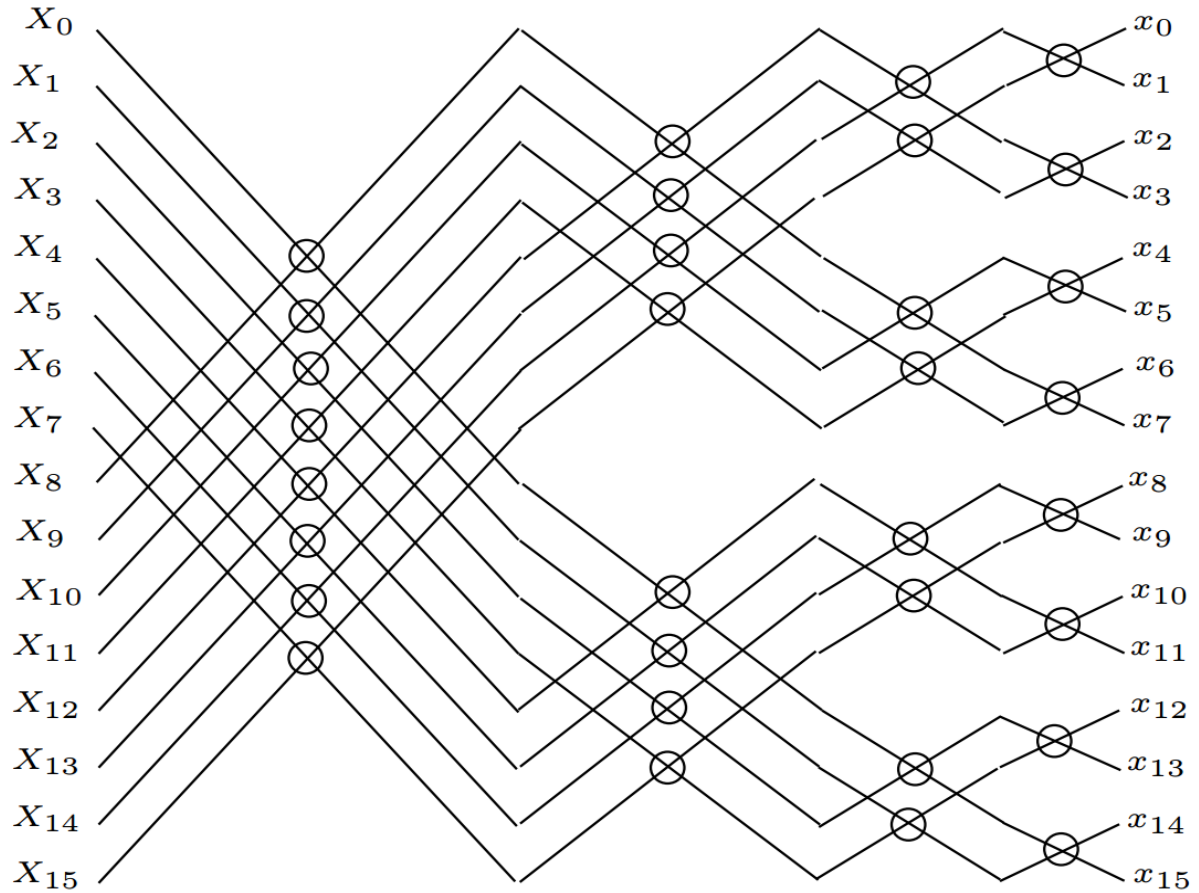
Figure 3.6 The WHT flowchart with N=16.

$$C_A^{WHT} = N \log_2 N \qquad\qquad (3.4.14)$$

3.5 T-transform

As mentioned in the previous section, WHT can be implemented in conjunction with DFT in many applications, however, the computational complexity can be greatly reduced if the DFT and WHT can be performed together using a single fast transform, which was introduced in [51]. The T-transform can be implemented as a replacement in scenarios where DFT and WHT are utilized such as multi-carrier division multiple access (MC-CDMA) and precoded OFDM, providing simpler calculation but still retains the characteristics of both transforms.

3.5.1 Forward T-transform

The size N forward T-transform (FTT), $\mathbf{T}$ is evaluated as [51]

$$\mathbf{T} = \frac{1}{N}\mathbf{F}\mathbf{W} \tag{3.5.1}$$

Where $\mathbf{F}$ and $\mathbf{W}$ are the normalized $N \times N$ DFT matrix rearranged in row reverse order and WHT matrix, respectively. Their elements are $W_{km} = (-1)^{\sum_{r=0}^{\log_2 N-1} k_r m_r}$ where k_r and m_r are the bit representation of the integer values k and m, and $F_{nk} = w^{nk} = e^{-j2\pi\frac{nk}{N}}$, respectively. The rows and columns of the DFT matrix, $\mathbf{F}$ can be recalculated based on $w^{nk} = w^{\langle nk \rangle_N}$ where $<>_N$ stands for the modulo-N operation. Similarly but with a reverse sign, the elements of the first half and the second half of the $\mathbf{F}$ matrix enables us to express the relationship among these elements as $w^{nk} = -w^{(nk-\frac{N}{2})}$ for $\frac{N}{2} \le nk < N$. Consequently, the $\mathbf{F}$ matrix in row reverse order can be rewritten as

$$\mathbf{F} = \begin{bmatrix} \mathbf{A}_{\frac{N}{2}} & \mathbf{A}_{\frac{N}{2}} \\ \mathbf{B}_{\frac{N}{2}} & -\mathbf{B}_{\frac{N}{2}} \end{bmatrix} \tag{3.5.2}$$

Where $\mathbf{A}$ and $\mathbf{B}$ are the sub-matrices of $\mathbf{F}$ and $\mathbf{A}_2 = \begin{bmatrix} 1 & 1 \\ 1 & -1 \end{bmatrix}$, $\mathbf{B}_2 = \begin{bmatrix} 1 & w^4 \\ 1 & -w^4 \end{bmatrix}$,

By quoting the matrix expression of WHT as in (3.4.23), the matrix representation for T-transform can be rewritten as:

$$\begin{aligned} \mathbf{T}_N &= \frac{1}{N}\begin{bmatrix} \mathbf{A}_{\frac{N}{2}} & \mathbf{A}_{\frac{N}{2}} \\ \mathbf{B}_{\frac{N}{2}} & -\mathbf{B}_{\frac{N}{2}} \end{bmatrix}\begin{bmatrix} \mathbf{W}_{\frac{N}{2}} & \mathbf{W}_{\frac{N}{2}} \\ \mathbf{W}_{\frac{N}{2}} & -\mathbf{W}_{\frac{N}{2}} \end{bmatrix} \\ &= \frac{1}{N}\begin{bmatrix} 2\mathbf{A}_{\frac{N}{2}}\mathbf{W}_{\frac{N}{2}} & 0 \\ 0 & 2\mathbf{B}_{\frac{N}{2}}\mathbf{W}_{\frac{N}{2}} \end{bmatrix} \end{aligned} \tag{3.5.3}$$

Therefore the generalized form of a size N T-transform matrix can be obtained as in [51]:

$$
\mathbf{T}_N = \frac{1}{N}
\begin{bmatrix}
\frac{N}{2}\mathbf{A}_2\mathbf{W}_2 & 0 & 0 & \cdots & 0 & 0 \\
0 & \frac{N}{2}\mathbf{B}_2\mathbf{W}_2 & 0 & \cdots & 0 & 0 \\
0 & 0 & \frac{N}{4}\mathbf{B}_4\mathbf{W}_4 & \cdots & 0 & 0 \\
\vdots & \ddots & \ddots & \cdots & \ddots & \ddots \\
0 & 0 & 0 & \cdots & 4\mathbf{B}_{\frac{N}{4}}\mathbf{W}_{\frac{N}{4}} & 0 \\
0 & 0 & 0 & \cdots & 0 & 2\mathbf{B}_{\frac{N}{2}}\mathbf{W}_{\frac{N}{2}}
\end{bmatrix}
\tag{3.5.4}
$$

Take $N = 16$ and $w^n = e^{-j2\pi\frac{n}{N}}$, the size 16 T-transform matrix is

$$
\mathbf{T}_{16}
$$

$$
=
\begin{bmatrix}
\frac{1}{2}\mathbf{A}_2\mathbf{W}_2 & 0 & 0 & 0 & 0 \\
0 & \frac{1}{2}\mathbf{B}_2\mathbf{W}_2 & 0 & 0 & 0 \\
0 & 0 & \frac{1}{4}\mathbf{M}_4\mathbf{W}_4 & 0 & 0 \\
0 & 0 & 0 & \frac{1}{8}(1+w^4)\mathbf{N}_4\mathbf{W}_4 & \frac{1}{8}(1-w^4)\mathbf{U}_4\mathbf{W}_4 \\
0 & 0 & 0 & \frac{1}{8}(1-w^4)\mathbf{N}_4\mathbf{W}_4 & \frac{1}{8}(1+w^4)\mathbf{U}_4\mathbf{W}_4
\end{bmatrix}
\tag{3.5.5}
$$

And

$$
\mathbf{M}_4 =
\begin{bmatrix}
1 & w^2 & w^4 & w^6 \\
1 & -w^2 & w^4 & -w^6 \\
1 & w^6 & -w^4 & w^2 \\
1 & -w^6 & -w^4 & -w^2
\end{bmatrix}
$$

$$
\mathbf{N}_4 =
\begin{bmatrix}
1 & w^1 & w^2 & w^3 \\
1 & -w^1 & w^2 & -w^3 \\
1 & w^5 & -w^2 & -w^7 \\
1 & -w^5 & -w^2 & w^7
\end{bmatrix}
\tag{3.5.6}
$$

$$
\mathbf{U}_4 =
\begin{bmatrix}
1 & w^3 & w^6 & -w^1 \\
1 & -w^3 & w^6 & w^1 \\
1 & w^7 & -w^6 & w^5 \\
1 & -w^7 & -w^6 & -w^5
\end{bmatrix}
$$

Substituting $\mathbf{A}_2, \mathbf{B}_2, \mathbf{M}_4, \mathbf{N}_4$ and $\mathbf{U}_4$ for their values in (3.5.5) yields the T-transform matrix for $N = 16$, we have

$$\mathbf{T_{16}} = \begin{bmatrix} 1 & 0 & 0 & 0 & 0 & 0 & 0 & 0 & 0 & 0 & 0 & 0 & 0 & 0 & 0 & 0 \\ 0 & 1 & 0 & 0 & 0 & 0 & 0 & 0 & 0 & 0 & 0 & 0 & 0 & 0 & 0 & 0 \\ 0 & 0 & a & b & 0 & 0 & 0 & 0 & 0 & 0 & 0 & 0 & 0 & 0 & 0 & 0 \\ 0 & 0 & b & a & 0 & 0 & 0 & 0 & 0 & 0 & 0 & 0 & 0 & 0 & 0 & 0 \\ 0 & 0 & 0 & 0 & ca & da & cb & db & 0 & 0 & 0 & 0 & 0 & 0 & 0 & 0 \\ 0 & 0 & 0 & 0 & da & ca & db & cb & 0 & 0 & 0 & 0 & 0 & 0 & 0 & 0 \\ 0 & 0 & 0 & 0 & eb & fb & ea & fa & 0 & 0 & 0 & 0 & 0 & 0 & 0 & 0 \\ 0 & 0 & 0 & 0 & fb & eb & fa & ea & 0 & 0 & 0 & 0 & 0 & 0 & 0 & 0 \\ 0 & 0 & 0 & 0 & 0 & 0 & 0 & 0 & gca & hca & gda & hda & leb & meb & lfb & mfb \\ 0 & 0 & 0 & 0 & 0 & 0 & 0 & 0 & hca & gca & hda & gda & meb & leb & mfb & lfb \\ 0 & 0 & 0 & 0 & 0 & 0 & 0 & 0 & nda & oda & nca & oca & pfb & qfb & peb & qeb \\ 0 & 0 & 0 & 0 & 0 & 0 & 0 & 0 & gca & nda & oca & nca & qfb & pfb & qeb & peb \\ 0 & 0 & 0 & 0 & 0 & 0 & 0 & 0 & gcb & hcb & gdb & hdb & lea & mea & lfa & mfa \\ 0 & 0 & 0 & 0 & 0 & 0 & 0 & 0 & hcb & gcb & hdb & gdb & mea & lea & mfa & lfa \\ 0 & 0 & 0 & 0 & 0 & 0 & 0 & 0 & ndb & odb & ncb & ocb & pfa & qfa & pea & qea \\ 0 & 0 & 0 & 0 & 0 & 0 & 0 & 0 & gcb & ndb & ocb & ncb & qfa & pfa & qea & pea \end{bmatrix} \qquad (3.5.7)$$

Where $a = \dfrac{1+w^4}{2}$, $b = \dfrac{1-w^4}{2}$, $c = \dfrac{1+w^2}{2}$, $d = \dfrac{1-w^2}{2}$, $e = \dfrac{1+w^6}{2}$, $f = \dfrac{1-w^6}{2}$, $g = \dfrac{1+w^1}{2}$, $h = \dfrac{1-w^1}{2}$, $l = \dfrac{1+w^3}{2}$, $m = \dfrac{1-w^3}{2}$, $n = \dfrac{1+w^5}{2}$, $o = \dfrac{1-w^5}{2}$, $p = \dfrac{1+w^7}{2}$, and $q = \dfrac{1-w^7}{2}$.

3.5.2 Inverse T-transform

Following the principle in constructing the forward T-transform, the inverse T-transform can be computed. The size $N \times N$ inverse T-transform matrix can be expressed as

$$\overline{\mathbf{T}} = \overline{\mathbf{W}}\,\overline{\mathbf{F}} \qquad (3.5.8)$$

Where $\widehat{\mathbf{W}}$ and $\widehat{\mathbf{F}}$ are the normalized $N \times N$ IWHT and the IFFT matrices, respectively. Using the same principles where $w^{-nk} = w^{\langle -nk \rangle_N}$ and $w^{-nk} = -w^{-(nk-\frac{N}{2})}$ for $\frac{N}{2} \le nk < N$, $\widehat{\mathbf{F}}$ will be re-calculated and rearranged according to the column reverse order. Hence we have

$$\widehat{\mathbf{T}} = \frac{1}{N}\begin{bmatrix} 2\overline{\mathbf{W}}_{\frac{N}{2}}\overline{\mathbf{A}}_{\frac{N}{2}} & 0 \\ 0 & 2\overline{\mathbf{W}}_{\frac{N}{2}}\overline{\mathbf{B}}_{\frac{N}{2}} \end{bmatrix} \qquad (3.5.9)$$

Following the same principle, the block diagonal structure of a size 16×16 $\overline{\mathbf{T}}$ matrix can be represented as

$$\overline{\mathbf{T}}_{16}$$

$$= \begin{bmatrix} \frac{1}{2}\overline{\mathbf{W}}_2\overline{\mathbf{A}}_2 & 0 & 0 & 0 & 0 \\ 0 & \frac{1}{2}\overline{\mathbf{W}}_2\overline{\mathbf{B}}_2 & 0 & 0 & 0 \\ 0 & 0 & \frac{1}{4}\overline{\mathbf{W}}_4\overline{\mathbf{M}}_4 & 0 & 0 \\ 0 & 0 & 0 & \frac{1}{8}(1+w^4)\overline{\mathbf{W}}_4\overline{\mathbf{N}}_4 & \frac{1}{8}(1-w^4)\overline{\mathbf{W}}_4\overline{\mathbf{U}}_4 \\ 0 & 0 & 0 & \frac{1}{8}(1-w^4)\overline{\mathbf{W}}_4\overline{\mathbf{U}}_4 & \frac{1}{8}(1+w^4)\mathbf{U}_4\mathbf{W}_4 \end{bmatrix} \quad (3.5.10)$$

Substituting the sub-matrices with their values, the size 16×16 inverse T-transform matrix can be written as

$$\overline{\mathbf{T}}_{16} = \begin{bmatrix} 1 & 0 & 0 & 0 & 0 & 0 & 0 & 0 & 0 & 0 & 0 & 0 & 0 & 0 & 0 & 0 \\ 0 & 1 & 0 & 0 & 0 & 0 & 0 & 0 & 0 & 0 & 0 & 0 & 0 & 0 & 0 & 0 \\ 0 & 0 & a & b & 0 & 0 & 0 & 0 & 0 & 0 & 0 & 0 & 0 & 0 & 0 & 0 \\ 0 & 0 & b & a & 0 & 0 & 0 & 0 & 0 & 0 & 0 & 0 & 0 & 0 & 0 & 0 \\ 0 & 0 & 0 & 0 & ac & ad & bc & bd & 0 & 0 & 0 & 0 & 0 & 0 & 0 & 0 \\ 0 & 0 & 0 & 0 & ad & ac & ba & bc & 0 & 0 & 0 & 0 & 0 & 0 & 0 & 0 \\ 0 & 0 & 0 & 0 & be & bf & ae & af & 0 & 0 & 0 & 0 & 0 & 0 & 0 & 0 \\ 0 & 0 & 0 & 0 & bf & be & af & ae & 0 & 0 & 0 & 0 & 0 & 0 & 0 & 0 \\ 0 & 0 & 0 & 0 & 0 & 0 & 0 & 0 & acg & ach & adg & adh & bel & bem & bfl & bfm \\ 0 & 0 & 0 & 0 & 0 & 0 & 0 & 0 & ach & acg & adh & adg & bem & bel & bfm & bfl \\ 0 & 0 & 0 & 0 & 0 & 0 & 0 & 0 & adn & ado & acn & aco & bfp & bfq & bep & beq \\ 0 & 0 & 0 & 0 & 0 & 0 & 0 & 0 & acg & adn & aco & acn & bfq & bfp & beq & bep \\ 0 & 0 & 0 & 0 & 0 & 0 & 0 & 0 & bcg & bch & bdg & bdh & ael & aem & afl & afm \\ 0 & 0 & 0 & 0 & 0 & 0 & 0 & 0 & bch & bcg & bdh & bdg & aem & ael & afm & afl \\ 0 & 0 & 0 & 0 & 0 & 0 & 0 & 0 & bdn & bdo & bcn & bco & afp & afq & aep & aeq \\ 0 & 0 & 0 & 0 & 0 & 0 & 0 & 0 & bcg & bdn & bco & bcn & afq & afp & aeq & aep \end{bmatrix} \quad (3.5.11)$$

Obviously, the arithmetic operations required to implement the inverse T-transform matrix and the forward T-transform matrix are identical.

Observing (3.5.7) and (3.5.11) it is clear that the T-transform matrix has a block diagonal structure with more than two thirds of the elements being zero. The number of arithmetic operations to multiply by the T-transform matrix are only 1/3 of those involved in multiplying by the DFT or IDFT matrices. Moreover, the T-transform matrix can be transformed into a product of sparse matrices leading to a much faster algorithm for calculating the T-transform and the corresponding inverse T-transform. Following the above process, the sparse matrices for both forward T-transform and inverse T-transform can be extended to any given length. A flowchart of the T-transform for $N = 16$ is given in Figure 3.7, where S_0, S_1 and S_2 represent the sections of this transform.
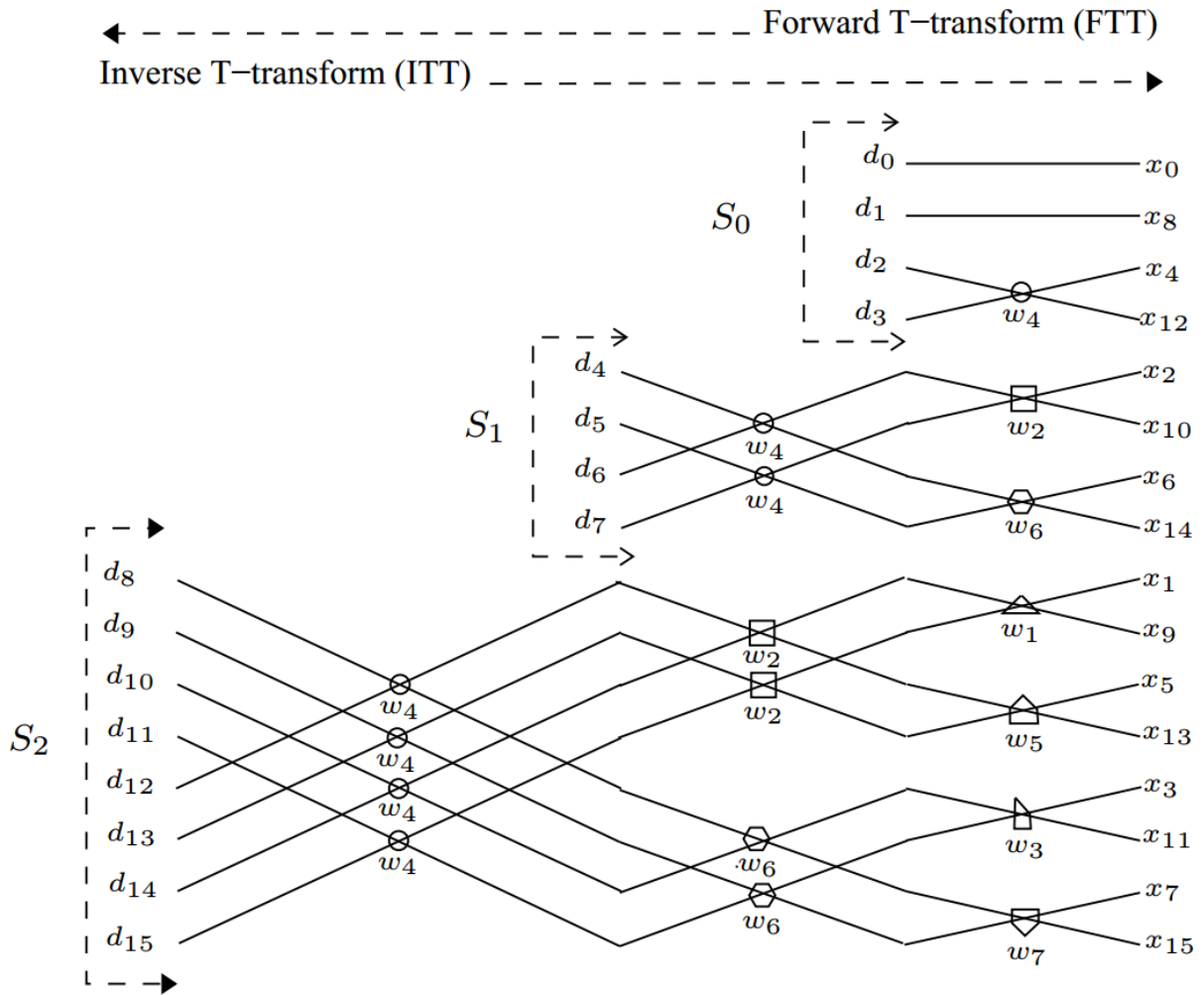
Figure 3.7: A flowchart for T-transform with $N = 16$ [51].

3.5.3 Computational Complexity

The computational complexity is one key aspect when it comes to judging whether a transform is eligible for use in practical communication systems. This section evaluates the computational costs of the T-transform. Equation (3.5.7) and (3.5.11) reveals that the forward T-transform and inverse T-transform matrices are sparse matrices with two thirds of their elements being zero. Consequently, the direct calculation of each individual matrix requires $N^2/3$ multiplications and $N(N - 1)/3$ additions, while the direct calculation of WHT and IDFT in cascaded form need N^2 complex multiplications and $2N(N - 1)$ complex additions. The real operations can be computed based on the fact that the complexity of a single complex multiplication is equivalent to either the complexity of four real multiplications and two real additions (4/2) or to the complexity of three real multiplications and three real additions (3/3) [65]. Here the (4/2)

version is adopted. Note that one complex addition is equivalent to two real additions. Therefore, the arithmetic operations required for the direct implementation of T-transform requires

$$R_M^T = \frac{4}{3} N^2 \tag{3.5.12}$$

$$R_A^T = \frac{4}{3} N^2 - \frac{4}{3} N \tag{3.5.13}$$

Where R_M and R_A represents the real multiplications and real additions, respectively. Conversely, the arithmetic operations required for the direct implementation of IDFT and WHT-IDFT in cascaded forms are

$$R_M^{IDFT} = 4N^2 \tag{3.5.14}$$

$$R_A^{IDFT} = 4N^2 - 2N \tag{3.5.15}$$

$$R_M^{WHT-IDFT} = 4N^2 \tag{3.5.16}$$

$$R_A^{WHT-IDFT} = 6N^2 - 4N \tag{3.5.17}$$

Moreover, the total computational complexity in terms of real additions is expressed based on [66] and [67] as

$$R_{total} = R_A + f R_M \tag{3.5.18}$$

where f denotes the real additions required for each operation involving multiplication. Assume a four-bit representation if utilized, hence the value $f = 4$ is taken for this evaluation. The total number of real additions required for all three considered transforms are evaluated as

$$R_{Total}^T = \frac{N}{3}(20N - 2) \tag{3.5.19}$$

$$R_{Total}^{IDFT} = N(20N - 2) \tag{3.5.20}$$

$$R_{Total}^{WHT-IDFT} = N(22N - 4) \tag{3.5.21}$$

3.6 T-transformed OFDM Systems

As discussed in the above sections, conventional OFDM system has great potential in UWA systems albeit its limitations. In order to deal with those detrimental aspects of conventional OFDM systems, this section introduces a new multicarrier system using the low computational

complexity T-transform that was first presented in [51] and discussed in the above sections as a single fast orthonormal unitary transform. The combined Walsh-Hadamard transform and discrete Fourier transform providing high frequency diversity gain by spreading the transmitted data onto all subcarriers therefore increasing the robustness of OFDM systems against frequency selective fading channels. By spreading each symbol's energy onto all the subcarriers, it is also found that T-OFDM reduces the problematic high PAPR significantly [69]. With all the stated advantages, this thesis examines the performance of T-OFDM in UWA channel with the comparison to conventional OFDM focusing on the design, testing of a novel channel equalization technique and analyzing then selecting the optimal PAPR reduction technique for use in UWA channels. The proposed system implements bit interleaved coded modulation with iterative decoding (BICM-ID) as FEC code to handle burst errors encountered through transmission. The bit interleaving provides large diversity order and soft bit decisions are employed to improve the conditional inter-signal Euclidean distance [70] [71]. The performance of the T-OFDM system for underwater acoustic communication is tested in the following chapters and a block diagram of the proposed system is shown in Figure 3.8.

Doppler shift is measured and compensated by a pre-processor at the receiver as in [72]. The channel estimation process is accomplished using pilot aided channel estimation techniques. However, due to the characteristics of the T-transform, the channel coefficient on each subcarrier affects all transmitted symbols, hence the channel estimation problem in the proposed T-OFDM system is different and requires further investigation beyond existing OFDM methods. Detailed analysis is presented in the following chapters. The training symbol based channel estimation methods adopted in conventional OFDM systems are presented first in the next section.
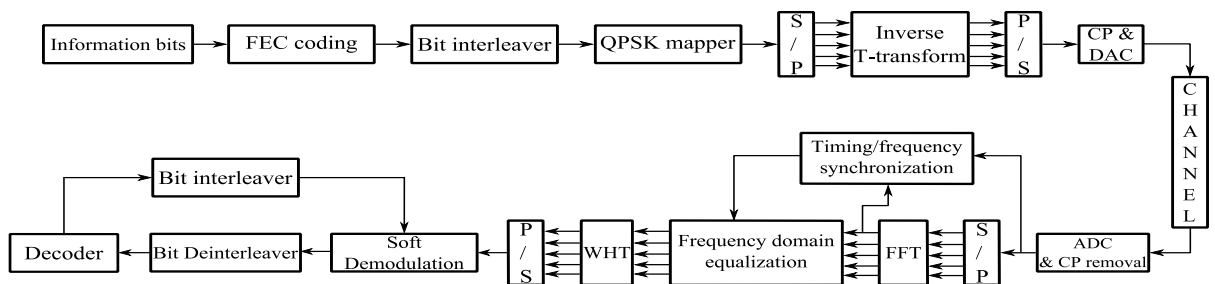
Fig. 3.8: Block diagram of the T-OFDM system used in following experiments.

3.7 Training Symbol Based Channel Estimation

Training symbols can often be used for channel estimation in OFDM systems, however at a cost of reduced transmission efficiencies due to the required overhead of training symbols such as pilot tones that are transmitted alongside with data symbols. The two most common types of training symbol based equalizers are zero-forcing (ZF) and minimum-mean-square-error (MMSE) technique. Assume there is no ICI among subcarriers, the training symbols for N subcarriers can be represented by the following diagonal matrix:

$$\mathbf{X} = \begin{bmatrix} X[0] & 0 & \cdots & 0 \\ 0 & X[1] & \cdots & \vdots \\ \vdots & \vdots & \ddots & 0 \\ 0 & \cdots & 0 & X[N-1] \end{bmatrix} \tag{3.7.0}$$

Where $X[k]$ denotes the pilot at the kth subcarrier. Assume that all subcarriers are orthogonal, hence $\mathbf{X}$ is a diagonal matrix. Denote the channel response on each subcarrier k as $H[k]$, the received signal R in the frequency-domain can be represented as

$$\mathbf{R} \triangleq \begin{bmatrix} R[0] \\ R[1] \\ \vdots \\ R[N-1] \end{bmatrix}$$

$$= [H[0]H[1]\cdots H[N-1]] \begin{bmatrix} X[0] & 0 & \cdots & 0 \\ 0 & X[1] & \cdots & \vdots \\ \vdots & \vdots & \ddots & 0 \\ 0 & \cdots & 0 & X[N-1] \end{bmatrix} + \begin{bmatrix} Z[0] \\ Z[1] \\ \vdots \\ Z[N-1] \end{bmatrix} \tag{3.7.1}$$

$$= \mathbf{HX} + \mathbf{Z}$$

Where $\mathbf{H}$ is a channel vector given as $\mathbf{H} = [H[0], H[1], \dots, H[N-1]]^T$ and $\mathbf{Z}$ is a noise vector given as $\mathbf{Z} = [Z[0], Z[1], \dots, Z[N-1]]^T$. Therefore, the kth element of $\mathbf{R}$ can be calculated as,

$$\mathbf{R}[k] = \frac{1}{\sqrt{N}} \sum_{n=0}^{N-1} r_n e^{\frac{-j2\pi nk}{N}} \tag{3.7.2}$$

$$= H[k]X[k] + Z[k], \forall k \in \{0, \dots, N\}$$

Using the equalizer sequence, the receiver sequence at the output of the equalizer can be expressed as

$$\hat{\mathbf{X}} = \mathbf{QR} \tag{3.7.3}$$

Where the diagonal equalizer matrix $\mathbf{Q}$ is:

$$\mathbf{Q} = \begin{bmatrix} Q_{0,0} & 0 & \cdots & 0 \\ 0 & Q_{1,1} & \cdots & 0 \\ \vdots & \vdots & \ddots & \vdots \\ 0 & 0 & \cdots & Q_{N,N} \end{bmatrix} \tag{3.7.4}$$

The elements of the equalizer matrix $\mathbf{Q}$ are therefore evaluated based on the chosen equalizer technique.

3.7.1 Zero-Forcing Channel Estimation

As in [113], under the assumption of no ICI, the ZF estimate for each of the subcarrier can be written as:

$$\hat{H}_{ZF}[\text{k}] = \frac{R[\text{k}]}{X[\text{k}]}, \quad k = 0,1,2,\dots,N-1 \tag{3.7.5}$$

And the corresponding equalizer sequence Q_{ZF} is:

$$Q_{ZF}[\text{k}] = \frac{1}{\hat{H}_{ZF}[k]}, \quad k = 0,1,2,\dots,N-1 \tag{3.7.6}$$

As can be seen from (3.7.5) and (3.7.6) that the main advantage of using ZF equalizer over other criterion is its low computational complexity, as it does not require any prior knowledge of the channel. However, in most real world scenarios, the received signal is often corrupted with noise. In those cases, adopting ZF equalizer without any noise compensation technique will introduce severe noise enhancement onto the received signal, leading to inferior performance. With the appearance of noise, the equalized signal using ZF equalizer can be expressed as:

$$\hat{X}[\text{k}] = X[\text{k}] + \frac{Z[k]}{H[k]}, \quad k = 0,1,2,\dots,N-1 \tag{3.7.7}$$

3.7.2 Minimum Mean Square Error (MMSE) Equalizer

The MMSE technique is introduced in order to overcome the noise enhancement encountered in ZF equalizers. The MMSE criterion is based on obtaining the mean square error (MSE)

between the transmitted and received signal. The equalizer minimizes the MSE by evaluating the optimal equalizer sequence $\mathbf{Q}_{MMSE}$. Therefore (3.7.3) can be re-written as:

$$\hat{\mathbf{X}} = \mathbf{Q}_{MMSE}\mathbf{R} \tag{3.7.8}$$

The MSE between $\mathbf{X}$ and $\hat{\mathbf{X}}$ can therefore be calculated as [73]:

$$e = [1 - \mathbf{Q}_{MMSE}\mathbf{H}][1 - \mathbf{Q}_{MMSE}\mathbf{H}]^* E\{|\mathbf{X}|^2\} + \mathbf{Q}_{MMSE}\mathbf{Q}_{MMSE}{}^* E\{|\mathbf{Z}|^2\} \tag{3.7.9}$$

Note that $\sigma_X^2 = E\{|\mathbf{X}|^2\}$ is the variance of the transmitted signal and $\sigma_Z^2 = E\{|\mathbf{Z}|^2\}$ denotes the variance of the noise. The optimal value of $\mathbf{Q}_{MMSE}$ is obtained by differentiating e with respect to $\mathbf{Q}_{MMSE}$ and set the equation to zero as,

$$\frac{\delta e}{\delta \mathbf{Q}_{MMSE}} = \mathbf{Q}_{MMSE}{}^* \sigma_Z^2 - \mathbf{H}[\mathbf{1} - \mathbf{Q}_{MMSE}\mathbf{H}]^* \sigma_X^2 = 0 \tag{3.7.10}$$

According to (3.7.9), the MMSE equalizer sequence can be computed as

$$\mathbf{Q}_{MMSE} = \frac{\mathbf{H}^* \sigma_X^2}{|\mathbf{H}|^2 \sigma_X^2 + \sigma_Z^2} \tag{3.7.11}$$

Therefore, the kth element of equalizer sequence $\mathbf{Q}$ based on the MMSE criterion can be

computed as

$$\begin{aligned}\mathbf{Q}_{MMSE} &= \frac{\mathbf{H}^* \sigma_X^2}{|\mathbf{H}|^2 \sigma_X^2 + \sigma_Z^2} \\ &= \frac{\lambda_0 H_k^*}{\lambda_0 |H_k|^2 + 1}\end{aligned} \tag{3.7.12}$$

Where λ_0 represents the signal-to-noise ratio (SNR) value of the received signal. Also note that, the MMSE criterion requires calculation of the noise variance σ_Z^2.

3.8 Chapter Conclusion

This chapter has outlined the key concepts of OFDM represented multicarrier transmission systems with an emphasis on the effect of multipath transmission and the design of guard intervals. This chapter also discussed the fast transforms associated with OFDM systems, namely, discrete Fourier transform (DFT) and Walsh-Hadamard transform (WHT) in terms of

the basic ideas and computational complexity. Moreover, the T-transform that combines the WHT and DFT into a single fast orthogonal unitary transform is also discussed in this chapter. This chapter serves as a building block for the proposed systems in the next chapters as the performance of T-OFDM systems is compared to conventional OFDM systems in terms of channel equalization and PAPR reduction.

CHAPTER 4

Performance comparison of T-OFDM and OFDM in underwater channels

In a UWA OFDM system, the transmitter modulates the message sequence into symbols then converts them into time-domain signals via IFFT. The time-domain signal is then sent out through a wireless acoustic channel. The received signal is usually distorted by multipath delay spread and Doppler Effect. As a result, in order to recover the transmitted sequence, the channel effects must be estimated and compensated for in the receiver. As discussed in Chapter 3, each subcarrier can be regarded as an independent channel, as long as the orthogonality among subcarriers is preserved. The orthogonality allows each subcarrier component of the received signal to be expressed as the product of the transmitted signal and channel frequency response at the subcarrier, consisting of a single complex valued coefficient. Therefore, the transmitted signal can be recovered by estimating the channel response at individual subcarriers. In general, the channel can be estimated by using signal known to both transmitter and receiver (preamble or pilot signals), which employ various interpolation techniques to estimate the channel response of the subcarriers between pilot tones. In order to choose the most suited channel estimation technique for the T-OFDM system under consideration, various aspects of implementation, including required performance, computational complexity, and time-variation of the channel must be taken into account. This chapter evaluates typical channel estimation techniques for UWA OFDM systems. Due to the fact that each channel coefficient affects all of the transmitted symbols in T-OFDM systems, a modified zero-forcing (ZF) channel equalizer

is introduced instead of existing OFDM methods. Details is explained in the following sections, along with performance of T-OFDM and OFDM systems with the proposed equalizer gathered in both water tank and the North Sea.

4.1 T-OFDM System Model

4.1.1 Transmitter

The block diagram of a typical uncoded T-OFDM transmitter is shown in Figure 4.1.

The information bits are first mapped to a $N \times 1$ data sequence, $\mathbf{X} = [X_0, X_1, \ldots, X_{N-1}]^T$ which is then fed into the inverse T-transform block to obtain the discrete-time baseband signal
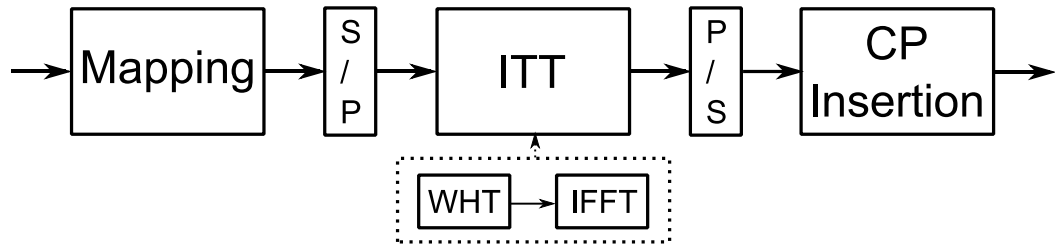
Figure 4.1: T-OFDM transmitter.

$$\mathbf{x} = \overline{\mathbf{T}}\mathbf{X} \tag{4.1.0}$$

Where $\overline{\mathbf{T}}$ represents the inverse T-transform matrix. The signal is the padded with CP and sent through the channel. Note that the length of CP, N_g is chosen based on a constraint equal to or greater than the maximum delay spread of the channel. After synchronization, the received time-domain data sequence is expressed as:

$$\mathbf{R} = \mathbf{D}\mathbf{x} + \mathbf{Z} \tag{4.1.1}$$

Where $R = [r_0, r_1, \ldots, r_{N-1}]^T$, $Z = [z_0, z_1, \ldots, z_{N-1}]^T$ denotes the received signal vector and the noise vector with variance σ_Z^2 and zero mean, and $\mathbf{D}$ is the circulant channel matrix.

4.1.2 Receiver

The received signal vector **r** need to be equalized in order to recover the transmitted information. The equalization process in a conventional OFDM system is performed in the frequency-domain by multiplying the received sequence with the equalizer sequence. For the proposed system, two types of receiver based on different channel equalization process can be utilized instead.

4.1.2.1 Receiver Type I

As established in the dyadic convolution theorem [59], the WHT of the product of two sequences is equivalent to the dyadic convolution of their WHT. As a result, the channel equalization process in conventional OFDM system can be replaced utilizing dyadic convolution between the output of the FFT block **Y** and the WHT of equalizer sequence, as shown in Figure 4.2. Consequently, the output of the dyadic convolution process is

$$\hat{X}_k = \sum_{m=0}^{N-1} Y_{m \oplus k} \hat{Q}_m \qquad (4.1.2)$$
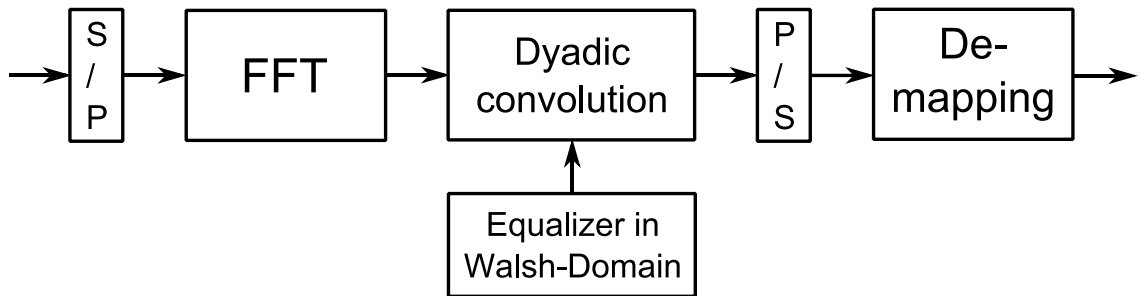
Figure 4.2: Block diagram of Type I receiver

Where $m \oplus k$ denotes the bit-by-bit modulo 2 sum of the integers *m* and *k* (exclusive OR operation between the bits of the binary representation of *m* and *k*) and $\hat{\mathbf{Q}}$ is the equalizer sequence in the Walsh-domain, which can be computed as

$$\hat{\mathbf{Q}} = \mathbf{W}\,\mathbf{Q} \qquad (4.1.3)$$

Where **Q** is the equalizer sequence in the frequency-domain.

However, due to the relatively high computational cost of Dyadic convolution, alternative receiver schemes were proposed in [69] with reduced computational complexity which will be described below.

4.1.2.2 Receiver Type II

The block diagram of the receiver type II is shown in Figure 4.3.
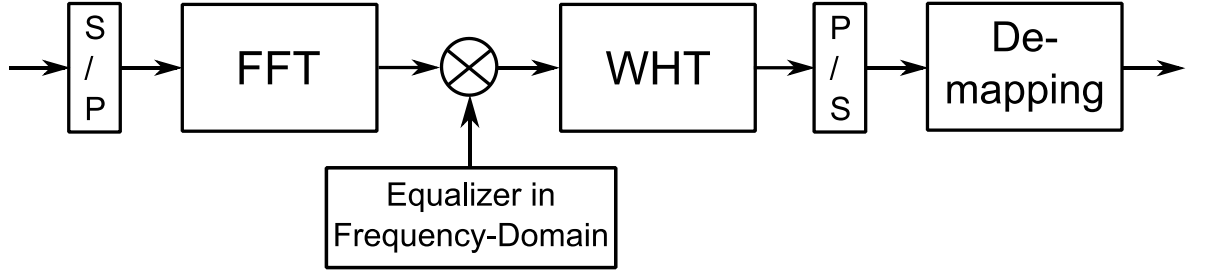
Figure 4.3: Block diagram of Type II receiver.

The channel equalization process in this type of receiver is similar to the frequency-domain equalization in conventional OFDM systems. The output of the frequency equalization is followed by a WHT of the equalized signal. Following the above process, the equalized signal can be expressed as:

$$\mathbf{R} = \widehat{\mathbf{R}} \cdot \mathbf{Q} \tag{4.1.4}$$

Where $\{\cdot\}$ denotes point-by-point multiplication of the two vectors. The vector $\widehat{\mathbf{R}} = [\widehat{R}_0, \widehat{R}_1, \ldots, \widehat{R}_{N-1}]^T$ vector is equivalent to $[\mathbf{F}\,\mathbf{r}]$ where $\mathbf{F}$ denotes the $N \times N$ normalized FFT matrix. Finally, the resultant signal is given as

$$\widehat{\mathbf{X}} = \mathbf{W}\,\mathbf{R} \tag{4.1.5}$$

4.1.2.3 Receiver Type III

By adopting the fast T-transform, the proposed system can utilized the traditional channel equalizer in the frequency domain, as demonstrated in the block diagram in Figure 4.4.
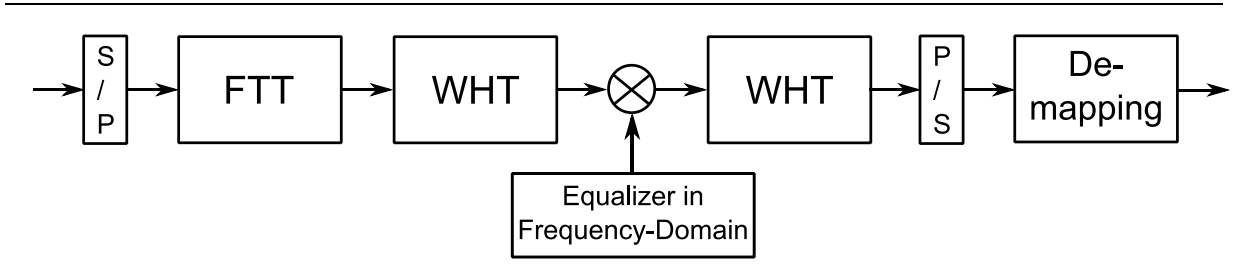
Figure 4.4: Block diagram of Type III receiver.

The channel equalization process in this receiver type is executed by sending the vector $\mathbf{r} = [r_0, r_1, \ldots, r_{N-1}]^T$ to the FTT block to acquire the signal as

$$\mathbf{Y} = \mathbf{T}\,\mathbf{r} \tag{4.1.6}$$

Then, the WHT of the FTT block output is computed as

$$\widehat{\mathbf{R}} = \mathbf{W}\,\mathbf{Y}^T \tag{4.1.7}$$

Afterwards, the resultant symbols are multiplied element-by-element, together with the frequency-domain equalizer sequence. Hence, the equalized signal is then expressed as

$$\mathbf{R} = \widehat{\mathbf{R}} \cdot \mathbf{Q} \tag{4.1.8}$$

Eventually, the equalized signal is transformed back to Walsh-domain through WHT.

This type of receiver allows the co-existence of OFDM and T-OFDM as the equalization process can both be performed in the frequency domain. The computational complexity of all three receiver types are analyzed next.

4.2 Computational Complexity

This section analyzes the computational costs of all three receiver types involved with the proposed T-OFDM system. The computational complexity of the WHT-OFDM system is also evaluated as a comparison.

4.2.1 Computational Cost of WHT-OFDM system

The total number of complex operations required to implement the WHT-OFDM system with the frequency domain equalizer is first considered. The operations includes the computation of the WHT and IFFT at the transmitter, FFT and WHT at the receiver, and the N multiplications

for the channel equalization process. As a result, the total number of complex multiplications C_M and complex additions C_A for this system is calculated as:

$$C_M^{WHT-OFDM} = N \log_2 N + N \tag{4.2.0}$$

$$C_A^{WHT-OFDM} = 4N \log_2 N \tag{4.2.1}$$

The corresponding calculations for the total number of real multiplications R_M and real additions R_A can be evaluated as

$$R_M^{WHT-OFDM} = 4[N \log_2 N + N] \tag{4.2.2}$$

$$R_A^{WHT-OFDM} = 10N \log_2 N + 2N \tag{4.2.3}$$

Hence, the overall computational complexity of the WHT-OFDM system in terms of real additions and multiplications can be calculated based on

$$R_{Total}^{WHT-OFDM} = R_A^{WHT-OFDM} + 4R_M^{WHT-OFDM} \tag{4.2.4}$$

Eventually, the total number of real operations required in the WHT-OFDM system is

$$R_{Total}^{WHT-OFDM} = 26N \log N + 18N \tag{4.2.5}$$

This number will serve as a comparison in the following evaluations of the three receiver types for the T-OFDM system.

4.2.2 Computational Cost of T-OFDM System with Receiver Type I

As shown in Figure 4.2, the type I receiver involves equalization in the Walsh-domain, therefore the computational complexity of dyadic convolution should be considered correspondingly when ITT and FTT is present. Recall that the number of complex multiplications and additions for dyadic convolution is N^2 and $(N-1)N$, respectively. Therefore, the total number of complex operations required with the implementation of receiver Type I can be expressed as [43]

$$C_M^{Receiver\ Type\ I} = N \log_2 N - (2N - 2) + N^2 \tag{4.2.6}$$

$$C_A^{Receiver\ Type\ I} = 3[N \log_2 N - (2N - 2)] + (N - 1)N \tag{4.2.7}$$

This type of receiver structure has similar computational cost comparing to WHT-OFDM system due to the dyadic convolution operations involved in both schemes.

4.2.3 Computational Cost of T-OFDM System with Receiver Type II

The type II receiver requires $\frac{1}{2}N \log_2 N + N$ (the extra N complex multiplications considered are for the channel equalization process) and $2N \log_2 N$ complex multiplications and complex additions, respectively. As a result, the total computational costs for this receiver type can be calculated as

$$C_{\mathrm{M}}^{Receiver\ Type\ II} = N \log_2 N + 1 \tag{4.2.8}$$

$$C_{\mathrm{A}}^{Receiver\ Type\ II} = \frac{7}{2}N \log_2 N - (3N - 3) \tag{4.2.9}$$

Consequently, the corresponding real multiplications and additions are calculated as:

$$R_{\mathrm{M}}^{Receiver\ Type\ II} = 4[N \log_2 N + 1] \tag{4.2.10}$$

$$R_{\mathrm{A}}^{Receiver\ Type\ II} = 9N \log_2 N - (6N - 8) \tag{4.2.11}$$

Eventually, the total number of real operations required to implement the T-OFDM system with Receiver II is

$$R_{Total}^{Receiver\ Type\ II} = 25N \log N - 6N + 24 \tag{4.2.12}$$

4.2.4 Computational Cost of T-OFDM System with Receiver Type III

The type III receiver requires $\frac{1}{2}[N \log_2 N + 2]$ and $\frac{7}{2}N \log_2 N - (3N - 3)$ complex multiplications and complex additions, respectively. Therefore the overall complexity of the T-OFDM system with Receiver III including the calculations of ITT at the transmitter can be evaluated as

$$C_{\mathrm{M}}^{Receiver\ Type\ III} = N \log_2 N - (N - 2) \tag{4.2.13}$$

$$C_{\mathrm{A}}^{Receiver\ Type\ III} = 5N \log_2 N - (6N - 6) \tag{4.2.14}$$

Therefore the total number of real multiplications, R_M and real additions, R_A of the type III receiver system can be calculated as

$$R_M^{Receiver\ Type\ III} = 4[N \log_2 N - (N - 2)] \tag{4.2.15}$$

$$R_A^{Receiver\ Type\ III} = 12N \log_2 N - (14N - 16) \tag{4.2.16}$$

And the corresponding real additions required in total for this type of receiver is

$$R_{Total}^{Receiver\ Type\ III} = 28N \log_2 N - (30N - 48) \tag{4.2.17}$$

Table 4.1 summarizes the total real arithmetic operations required for all three receiver types with comparison to WHT-OFDM systems.

Table 4.1: Total real arithmetic operations in the proposed receivers.

NUMBER OF REAL OPERATIONS

N	WHT-OFDM	Receiver Type II	Receiver Type III
64	11136	9240	8880
256	57856	49688	49712
1024	284672	249880	256048

As can be seen from Table 4.1, although the Receiver Type II and Type III revealed slightly lower computational burden, however this difference will not make a huge deal for any practical purposes.

4.3 Theoretical Performance Analysis

This section evaluates the BER performance of the proposed T-OFDM system. The performance analysis is conducted between conventional OFDM and T-OFDM systems with different channel model.

The performance of M-PSK systems over AWGN channel in terms of probability of errors (P_e) can be expressed as [73]:

$$P_{eM-PSK} = \frac{\varepsilon}{m} Q\left(\sqrt{2SNR} \sin\left(\frac{\pi}{M}\right)\right) \tag{4.3.0}$$

Where ε denotes the average number of nearest neighbor signal points, $m = \log_2 M$ stands for the number of bits in each constellation sample. SNR stands for the signal-to-noise ratio which is composed as σ_X^2 / σ_Z^2, where σ_X^2 is the desired average signal power, and σ_Z^2 stands for the Gaussian noise power. The Q-function of variable x is computed as [43] $Q(x) = \frac{1}{\sqrt{2\pi}} \int_x^\infty e^{-t^2/2} \, dt$.

As a result, the BER performance of conventional OFDM system and the proposed T-OFDM system over various channel models can be analyzed based on (4.3.0). Consequently, the general formula for computing the average SNR of the receiver signal can be calculated:

$$SNR = \frac{Desired\ Signal\ Average\ Power}{Noise\ Average\ Power} = \frac{\sigma_X^2}{\sigma_Z^2} \qquad (4.3.1)$$

4.3.1 Performance Analysis of the Conventional OFDM Systems

The performance of OFDM system can be analyzed in different impairments in terms of receiver distortion or transmission media obstacles [74] [75] [76] [77]. In this chapter, the performance analysis is presented based on the calculation of the ratio σ_X^2 / σ_Z^2 over the various channel models (AWGN channel, flat-fading channel, and quasi-static frequency selective fading channel).

4.3.1.1 AWGN Channel

The performance of M-PSK OFDM over the AWGN channel is similar to the performance of M-PSK systems. For a conventional OFDM system across an AWGN channel, let $\mathbf{X}$ denotes the data vector with the assumption that each independent subcarrier has a variance σ_X^2, so that $E\{\mathbf{X}\mathbf{X}^*\} = \sigma_X^2 \mathbf{I}$, where $\mathbf{I}$ is the identity matrix, $\mathbf{Z}$ denotes the frequency domain representation of the uncorrelated Gaussian random variables $\mathbf{z}$ with average power σ_Z^2, and $\overline{X}$ is the received data sequence. Hence, the received data sequence can be represented as:

$$\overline{X} = \mathbf{X} + \mathbf{Z} \qquad (4.3.2)$$

The SNR for $\overline{X}$ can be calculated as:

$$SNR = \frac{E\{|\mathbf{X}|^2\}}{E\{|\mathbf{Z}|^2\}} = \frac{\sigma_X^2}{\sigma_Z^2} \tag{4.3.3}$$

Where $E\{.\}$ denotes the expectation operation. Finally, the BER performance of OFDM system across AWGN channels can be calculated by substituting equation (4.3.3) into (4.3.0) for M-PSK.

4.3.1.2 Flat Fading Channel

For a flat fading channel, the received signal with ZF equalizer can be calculated as

$$\widehat{\mathbf{X}} = \mathbf{X} + \boldsymbol{Q}^{ZF}\mathbf{Z} \tag{4.3.4}$$

Where $Q_k^{ZF} = 1/H_k$, and H_k is the k-th frequency domain channel coefficient. The SNR of k-th subcarrier can then be represented as:

$$SNR_k^{Flat} = \frac{|X_k|^2}{|Z_k|^2|Q_k^{ZF}|^2} \tag{4.3.5}$$

Consequently, for a flat fading channel, the average SNR for the OFDM system across every received symbols can be expressed as:

$$SNR^{Flat} = \frac{\sigma_X^2}{\sigma_Z^2|Q^{ZF}|^2} \tag{4.3.6}$$

Eventually, by substituting (4.3.6) into (4.3.0), the theoretical BER of an OFDM system in a flat fading channel can be computed as:

$$P_{eM-PSK}^{Flat} = \frac{\varepsilon}{m}Q(\sqrt{2SNR^{Flat}}\sin(\pi/M)) \tag{4.3.7}$$

On the other hand, the same received signal equalized with a MMSE equalizer is expressed as:

$$\bar{X}_k = \Omega_k^{MMSE}X_k + \Omega_k^{MMSE}Z_k \tag{4.3.8}$$

Where $\Omega_k^{MMSE} = \frac{\lambda_0 H_k^*}{\lambda_0|H_k|^2+1}$ is an approximation of the MMSE equalizer sequence and $\Omega_k^{MMSE} = Q_k^{MMSE}H_k = \frac{\lambda_0|H_k|^2}{\lambda_0|H_k|^2+1}$. Consequently, the SNR of the k-th subcarrier in (4.3.8) can be computed as:

$$SNR_k = \frac{(\Omega_k^{MMSE})^2 |X_k|^2}{|Q_k^{MMSE}|^2 |Z_k|^2}$$

$$= \frac{|X_k|^2 |H_k|^2}{|Z_k|^2} \tag{4.3.9}$$

This verifies that the performance of a conventional OFDM system over a flat fading channel is identical utilizing either a ZF or MMSE equalizer.

4.3.1.3 Frequency Selective Fading Channel

Over a quasi-static frequency selective channel, each subcarrier suffers according to its own channel coefficient H_k. As a result, the SNR for each subcarrier can be written as:

$$SNR_k^{FS} = \frac{|X_k|^2 |H_k|^2}{|Z_k|^2} \tag{4.3.10}$$

By substituting (4.3.10) into (4.3.0), the average BER of OFDM system with frequency selective fading channel can be expressed as:

$$P_{eOFDM_{M-PSK}}^{FS} = \frac{\varepsilon}{mN} \sum_{k=0}^{N-1} Q\left(\sqrt{2\lambda_k^{FS}} \sin(\pi/M)\right) \tag{4.3.11}$$

Similar to equation (4.3.9), the performance of the OFDM system utilizing MMSE over frequency selective fading channel is similar to that when ZF equalizer is utilized.

4.3.2 Performance Analysis of the Proposed T-OFDM System

This section investigates the BER performance of T-transform based OFDM systems. For the sake of simplicity, receiver type II as shown in Figure 4.3 will be analyzed.

4.3.2.1 AWGN Channel

With added Gaussian noise, the received signal at the type II receiver shown in Figure 4.3 can be expressed as:

$$\bar{\mathbf{X}} = \mathbf{X} + \mathbf{W} \mathbf{Z} \tag{4.3.12}$$

In equation (4.3.12), each element of the noise vector can be expressed as $\rho_n = \frac{1}{\sqrt{N}} \sum_{k=0}^{N-1} Z_k W_{k,n}$. Consequently, the variance of ρ can be written as:

$$E\{|\rho_n|^2\} = \frac{1}{N^2} \sum_{n=0}^{N-1} \left(\sum_{k=0}^{N-1} Z_k W_{n,k} \sum_{k=0}^{N-1} Z_k^* W_{k,n}^* \right) \tag{4.3.13a}$$

$$= \frac{1}{N^2} \sum_{n=0}^{N-1} \left(\sum_{k=0}^{N-1} |Z_k|^2 |W_{n,k}|^2 \right)$$

$$+ \frac{1}{N^2} \sum_{n=0}^{N-1} \left(\sum_{k=0}^{N-1} \sum_{g=0,g \neq k}^{N-1} Z_k Z_g^* W_{k,n} W_{g,n}^* \right) \tag{4.3.13b}$$

As explained in [43], due to the orthogonality of WH transform, the second term of the right hand side of (4.3.13b) is equal to zero. As a result,

$$E\{|\rho_n|^2\} = \frac{1}{N^2} \sum_{k=0}^{N-1} |Z_k|^2 \sum_{n=0}^{N-1} |W_{n,k}|^2 \tag{4.3.14a}$$

$$= \frac{1}{N} \sum_{k=0}^{N-1} |Z_k|^2 \tag{4.3.14b}$$

$$= \sigma_Z^2 \tag{4.3.14c}$$

From (4.3.14a-4.3.14c), the performance of T-OFDM and conventional OFDM systems over AWGN channel are identical.

4.3.2.2 Flat Fading Channel

The received T-OFDM signal in a flat fading channel can be expressed accordingly as:

$$\overline{\mathbf{X}} = \mathbf{WQF}(\mathbf{D}\overline{\mathbf{T}}\mathbf{X}) + \mathbf{WQFz}$$

$$= \mathbf{W\Omega}\overline{\mathbf{R}} + \mathbf{WQZ} \tag{4.3.15}$$

Where $E[|\overline{\mathbf{R}}|^2] = E[|\mathbf{X}|^2] = \sigma_X^2$.

Due to flat fading channel, the value of the equalizer sequence Ω_k for all k are identical. Therefore, for MMSE equalizer, the average power of the desired signal can be computed as

$$E|\mathbf{W\Omega}\overline{\mathbf{R}}|^2 = a^2 \sigma_X^2$$

$$= \sigma_X^2 (\Omega_k^{\text{MMSE}})^2 \tag{4.3.16}$$

Where $a = \frac{1}{N} \sum_{k=0}^{N-1} \Omega_k^{\text{MMSE}}$. The noise variance can then be computed as:

$$E\{\overline{\mathbf{X}}\overline{\mathbf{X}}^*\} - E|\mathbf{W}\Omega\overline{\mathbf{R}}|^2$$

$$= \sigma_X^2 \frac{1}{N} \sum_{k=0}^{N-1} \left(\Omega_k^{\mathrm{MMSE}}\right)^2 + \sigma_Z^2 \frac{1}{N} \sum_{k=0}^{N-1} \left|Q_k^{\mathrm{MMSE}}\right|^2 - \sigma_X^2 (\Omega_k^{\mathrm{MMSE}})^2$$

$$= \sigma_X^2 \left|\Omega_k^{\mathrm{MMSE}}\right|^2 + \sigma_Z^2 \left|Q_k^{\mathrm{MMSE}}\right|^2 - \sigma_X^2 (\Omega_k^{\mathrm{MMSE}})^2$$

$$= \sigma_Z^2 \left|Q_k^{\mathrm{MMSE}}\right|^2$$

(4.3.17)

Where $k \in \{0 \ldots N-1\}$. Substituting (4.3.16) and (4.3.16) into (4.3.3), hence:

$$SNR_k^{flat-TOFDM} = \frac{\sigma_X^2 \left(\Omega_k^{\mathrm{MMSE}}\right)^2}{\sigma_Z^2 \left|Q_k^{\mathrm{MMSE}}\right|^2}$$

$$= \frac{\sigma_X^2 H_X^2}{\sigma_Z^2}$$

(4.3.18)

Equation (4.3.18) verified that the performance of conventional OFDM and the proposed T-OFDM system over flat fading channel are identical with both ZF and MMSE equalization scheme.

4.3.2.3 Frequency Selective Fading Channel

Although the equalization scheme does not affect the performance of T-OFDM system in AWGN or flat fading channels, the performance alters drastically for T-OFDM in frequency selective fading channels with different equalizer techniques. This will be verified in the following. Based on the ZF criterion, the received signal after equalization process can be written as:

$$\overline{\mathbf{X}} = \mathbf{W}\mathbf{Q}^{\mathbf{ZF}}\mathbf{F}(\mathbf{D}\overline{\mathbf{T}}\mathbf{X}) + \mathbf{W}\mathbf{Q}^{\mathbf{ZF}}\mathbf{F}\mathbf{z}$$

$$= \mathbf{X} + \mathbf{W}\mathbf{Q}^{\mathbf{ZF}}\mathbf{Z}$$

(4.3.19)

Following the same procedure, the SNR for the received signal can be evaluated as

$$SNR_{\mathrm{T-OFDM}}^{\mathrm{ZF}} = \frac{\sigma_X^2}{\sigma_Z^2 \underbrace{\frac{1}{N} \sum_{k=0}^{N-1} |Q_k^{ZF}|^2}_{\Delta}}$$

(4.3.20)

Equation (4.3.20) verifies that the T-transform will average the value Δ onto all subcarriers, which in some scenarios may be helpful, but when there is a presence of null spectral in the

channel response, i.e. $H_k = 0$, the value of Δ will be infinity, leading to destruction of the received samples. Consequently, the BER performance of the T-OFDM system will degrade drastically implementing the ZF equalizer when channel nulls are present.

Conversely, the MMSE criterion can be implemented in order to alleviate the effect of null spectral. The received T-OFDM signal with MMSE equalizer can be expressed as:

$$\overline{\mathbf{X}} = \mathbf{W}\boldsymbol{\Omega}^{\text{MMSE}}\overline{\mathbf{R}} + \mathbf{W}\mathbf{Q}^{\text{MMSE}}\mathbf{Z} \tag{4.3.21}$$

Recalculating part of (4.3.3) as

$$E\left|\mathbf{W}\boldsymbol{\Omega}^{\text{MMSE}}\overline{\mathbf{R}}\right|^2 = a^2\sigma_X^2 \tag{4.3.22}$$

Also, the noise variance can be calculated as

$$\begin{aligned}
E\{|\overline{\mathbf{X}}|^2\} &- E\left|\mathbf{W}\boldsymbol{\Omega}^{\text{MMSE}}\overline{\mathbf{R}}\right|^2 \\
&= \sigma_X^2 \frac{1}{N}\sum_{k=0}^{N-1}\left(\Omega_k^{\text{MMSE}}\right)^2 + \sigma_Z^2 \frac{1}{N}\sum_{k=0}^{N-1}\left|Q_k^{\text{MMSE}}\right|^2 - a^2\sigma_X^2 \\
&= \sigma_X^2 \frac{1}{N}\sum_{k=0}^{N-1}\frac{(\lambda|H_k|^2)^2}{(\lambda|H_k|^2 + 1)^2} + \sigma_X^2 \frac{1}{N}\frac{1}{\lambda}\sum_{k=0}^{N-1}\frac{\lambda^2|H_k|^2}{(\lambda|H_k|^2 + 1)^2} - a^2\sigma_X^2 \\
&= \sigma_X^2 \frac{1}{N}\sum_{k=0}^{N-1}\frac{\lambda|H_k|^2(1 + \lambda|H_k|^2)}{(\lambda|H_k|^2 + 1)^2} - a^2\sigma_X^2 \\
&= \sigma_X^2 \frac{1}{N}\sum_{k=0}^{N-1}\frac{\lambda|H_k|^2}{(\lambda|H_k|^2 + 1)} - a^2\sigma_X^2 \\
&= \sigma_X^2(a - a^2)
\end{aligned} \tag{4.3.23}$$

After obtaining (4.3.23), we get:

$$\begin{aligned}
SNR_{\text{T-OFDM}}^{\text{MMSE}} &= \frac{a^2}{a - a^2} \\
&= \frac{a}{1 - a} \\
&= \frac{\sum_{k=0}^{N-1}\dfrac{\lambda|H_k|^2}{\lambda|H_k|^2 + 1}}{N\left(1 - \dfrac{1}{N}\sum_{k=0}^{N-1}\dfrac{\lambda|H_k|^2}{\lambda|H_k|^2 + 1}\right)}
\end{aligned} \tag{4.3.24}$$

Denote $\Lambda_k = \lambda|H_k|^2$, hence (4.3.24) can be rewritten as

$$SNR_{\text{T-OFDM}}^{\text{MMSE}} = \frac{\sum_{k=0}^{N-1} \frac{\Lambda_k}{\Lambda_k + 1}}{N(1 - \frac{1}{N}\sum_{k=0}^{N-1} \frac{\Lambda_k}{\Lambda_k + 1})} \tag{4.3.25}$$

Due to the fact that

$$\sum_{k=0}^{N-1} \frac{\Lambda_k}{\Lambda_k + 1} + \sum_{k=0}^{N-1} \frac{1}{\Lambda_k + 1} = N \tag{4.3.26}$$

Thus, the denominator of (4.6.25) can be expressed as

$$N\left(1 - \frac{1}{N}\sum_{k=0}^{N-1} \frac{\Lambda_k}{\Lambda_k + 1}\right) = \sum_{k=0}^{N-1} \frac{1}{\Lambda_k + 1} \tag{4.3.27}$$

Therefore, by substituting (4.3.26) into (4.3.25), we can obtain the average SNR of T-OFDM system with MMSE equalizer in a frequency selective fading channel as

$$SNR_{\text{T-OFDM}}^{\text{MMSE}} = \frac{\sum_{k=0}^{N-1} \frac{\Lambda_k}{\Lambda_k + 1}}{\sum_{k=0}^{N-1} \frac{1}{\Lambda_k + 1}} \tag{4.3.28}$$

Eventually, the BER performance of the T-OFDM over frequency selective fading channel with M-PSK implementing MMSE equalizer can be evaluated as:

$$P_{eTOFDM_{M-PSK}}^{FS} = \frac{\varepsilon}{m} Q(\sqrt{2SNR_{TOFDM}^{MMSE}} \sin(\pi/M) \tag{4.3.29}$$

In order to deal with the detrimental noise enhancement effect, a modified ZF equalizer is proposed. Detail on the proposed equalizer is presented in the next chapter. Note that, the performance of the proposed modified ZF equalizer depends only on the accuracy of outlier identification. Hence, only real world test performance is considered and presented in Chapter 5. The numerical results are presented in the following section.

4.4 Numerical Results

The performance of the proposed T-OFDM system implementing different equalizer criteria in comparison to conventional OFDM system is validated in this section. The tested system is designed based on the block diagram as shown in Figure 4.5.
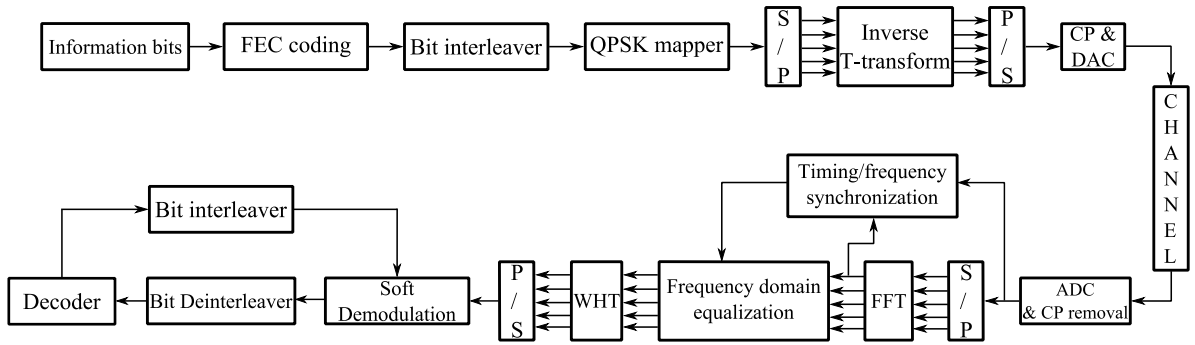
Figure 4.5: Proposed system diagram.

4.4.1 Experiment Design

As stated in [80], the performance of an OFDM system varies with its FFT size. Systems with larger FFT sizes can better utilize the channel's frequency diversity as the subcarrier spacing is inversely proportional to the FFT size. However, the symbol duration increases with the FFT size which endangers the performance of the channel estimator as the assumption that the channel is quasi-static within the transmission of one OFDM symbol no longer stands true. Keeping this in mind, the corresponding OFDM packets are generated with FFT size of 512, 1024 and 2048, respectively. The bandwidth of the OFDM signal used in the following experiment is $B = 8$ kHz, and the carrier frequency is $f_c = 12$ kHz. Therefore the transmitted signal occupies the frequency band between 8 and 16 kHz. A guard interval of $T_g = 20 \, ms$ per OFDM block is utilized. As the respective numbers of subcarriers used in the experiment are $K = 512, 1024 \, and \, 2048,$ the subcarrier spacing is $\Delta f = 15.63, 7.81$ and 3.91 Hz, and the OFDM block duration is $T = 1/\Delta f = 63.98, 128.04$ and 255.75 ms. Rate 2/3 convolutional coding is chosen as the code rate for this experiment. It is obtained by puncturing a rate 1/2 code with the generator polynomial expressed in octal as [23,35] with a minimal free distance d_{free} of 7 and a upper bound on d_{free} of 8, with a constraint length of 5. This value was selected from a table of optimum polynomials, chosen for exhibiting the largest minimum free distance, d_{min} [114, pp517, Table 8.3-1]. The coding is applied within the date stream for each OFDM block. The packet structure is shown in Fig 4.6. For one transmitted packet, the total number of information bits per packet is 30976. Table 4.2 summarizes the system parameters. The factor BT_g/K determines the bandwidth efficiency, $\frac{R}{B} = (1 + \alpha)$

symbols/s/Hz. Bit rates based on the generated packet structure are calculated accordingly in Table 4.3, where pilots of size $N_p = N/4$ are accounted for.
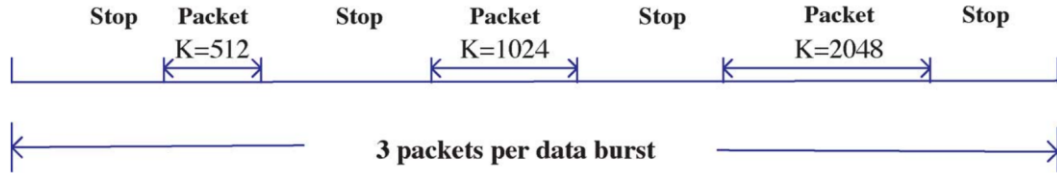
Figure 4.6: Packet structure of a data burst consists of three FFT sizes.

Table 4.3 also shows the system throughput with and without coding. Packets within burst are generated by concatenating blocks of T-OFDM signal with OFDM signal. Those three blocks are separated by different type/length header chips. Silent periods of 20ms are inserted between neighboring packets which not only serve as guard bands but also can be used to measure noise variance. Data bursts are sent through the channel continuously during the test.

Table 4.2 Signal Parameters for the tested T-OFDM and OFDM systems

B=8kHz	FFT size K	Δf(Hz)	T(ms)	BT_g/K
$f_c = 12kHz$	512	15.63	63.98	0.31
$T_g = 20ms$	1024	7.81	128.04	0.16
QPSK	2048	3.91	255.75	0.08

Table 4.3 Bit rates of the proposed system

N	# of pilots N_g	Block duration $T+T_g$	Bit rate without coding $\frac{2(N-N_g)}{T+T_g}$	Bit rate with rate ½ channel coding	Bit rate with rate 2/3 channel coding
512	128	83.98 ms	9.15 kb/s	4.58 kb/s	6.1 kb/s
1024	256	148.04 ms	10.38 kb/s	5.18 kb/s	6.92 kb/s
2048	512	275.75 ms	11.14 kb/s	5.57 kb/s	7.43 kb/s

4.4.2 Water Tank Test Results

The proposed system is first tested in a water tank with approximate dimensions of 3m long, 2m wide and 2m deep. A certain degree of channel variability is attained by stirring the tank water. Figure 4.7 offers an overall view of the anechoic testing tank.

Figure 4.7: Newcastle University Sensors Electromagnetics and Acoustics Laboratory (SEA Lab) Anechoic Testing Tank.

Two data packets are generated for this experiment. The first packet is generated with the aim of illustrating T-OFDM system's ability of improving the BER performance without sacrificing any system throughput. In order to fully reveal the aforementioned potential, T-OFDM with FFT size of 1024 is compared to OFDM with both 1/2 code rate and approximately 9/10 code rate obtained by puncturing. The corresponding puncturing matrix P for code rate 2/3 with a constraint length of 5 and $d_{\text{free}} = 4$ is $p = \begin{bmatrix} 1 & 1 \\ 1 & 0 \end{bmatrix}$, and the puncture matrix for approximate code rate of 9/10 with a constraint length of 5 and $d_{\text{free}} = 3$ is $p = \begin{bmatrix} 1 & 0 & 1 & 0 & 0 & 1 & 1 \\ 1 & 1 & 0 & 1 & 1 & 0 & 0 \end{bmatrix}$ [114, pp522, Table8.4-1]. Rate 9/10 is chosen representing an extreme case where maximal throughput is achieved. Take FFT size of 1024 as an example, the BER results are shown in Figure 4.8.

It is clear that with enough added redundancy, conventional OFDM system marginally outperforms the proposed T-OFDM system. On the other hand, T-OFDM system with rate 9/10 convolutional code outperforms the corresponding OFDM systems significantly as the spectral diversity introduced by the T-transform offers a substantial performance gain with minimal redundancy.
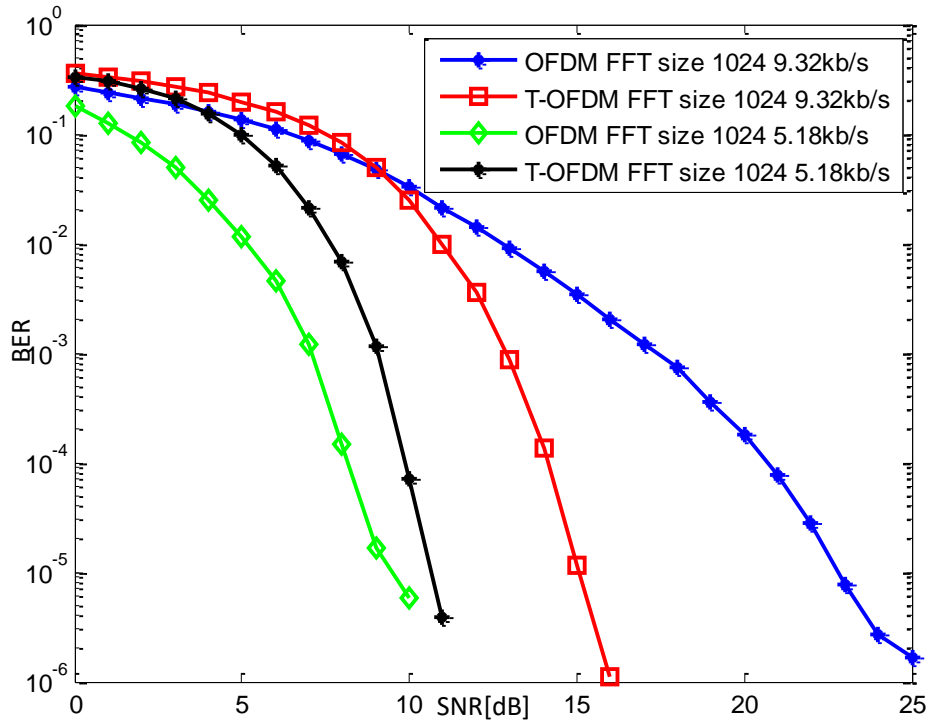
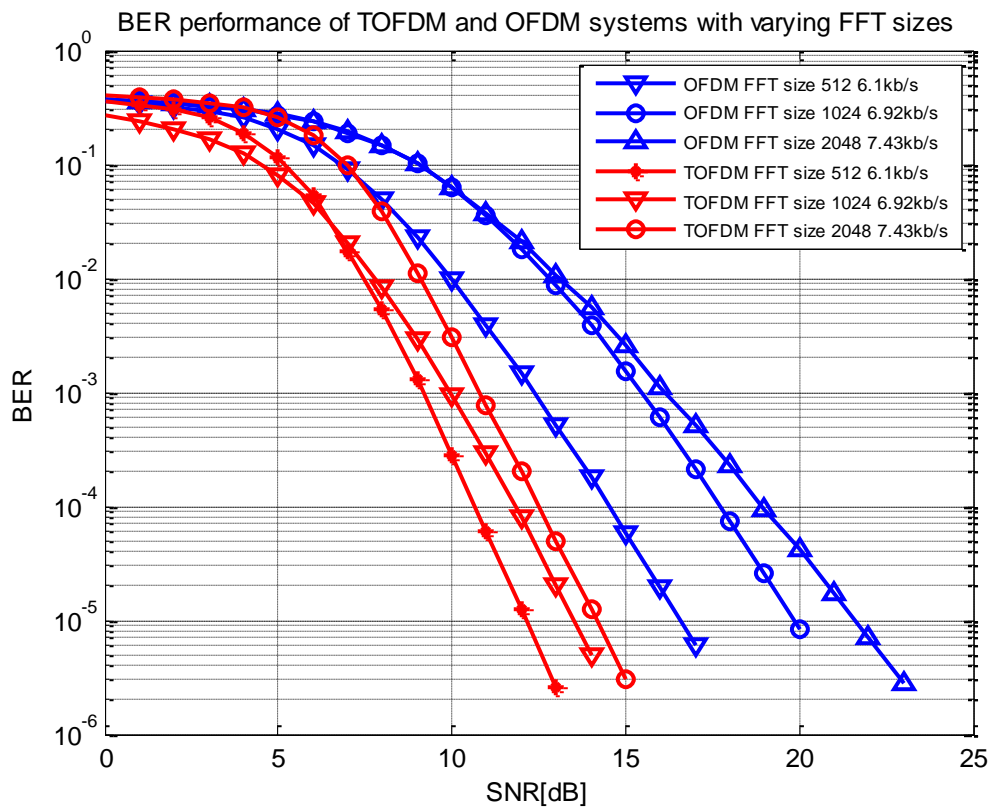Figure 4.8: BER performance between systems with different throughputs.

Figure 4.9: BER performance of the proposed system with varying FFT sizes.

However, considering the challenging nature of realistic UWA channels, code rate 2/3 is chosen in the final systems as it provides a balance point between robustness with enough added redundancy and data rate. The corresponding BER results are shown in Figure 4.9. It is clear that with reduced redundancy (comparing to rate 1/2 systems), the proposed T-OFDM systems outperform conventional OFDM systems for all FFT sizes. The BER results in Figure 4.8 and 4.9 together summarizes that T-OFDM can be used with much lower redundancy (high throughput) than OFDM, as a result, spectral efficiency is greatly increased.

Conversely, due to the spreading property of the T-transform, the equalizer technique required in order to achieve this advantage in realistic channels is different than those in conventional OFDM systems. Note that, a proposed modified ZF equalizer is used here for generating the above results. Detailed analysis is presented in the next chapter.

4.5 Chapter Conclusion

This chapter focused on the performance of T-OFDM and OFDM systems in underwater channels. Three receiver structures that can be used with T-OFDM were presented. Furthermore, the complexity calculations relating to the proposed system and the three receiver schemes were provided and compared with those for the WHT-OFDM system. Moreover, the theoretical analysis of the proposed system given over three channel models (AWGN, flat fading, and frequency selective fading) was introduced in this chapter. On the other hand, although the computational burden across three receiver types varies, the performance remains the same for all three receiver types, not to mention that the difference in computational cost will have much less an effect in any practical systems. As a result, testing shown later in this thesis are all conducted using receiver type II for simplicity purpose. Analytic results revealed that the proposed T-OFDM system achieves the same BER as a conventional OFDM over AWGN and flat fading channels. The BER performance of T-OFDM system is verified by a water tank test. Different data throughputs were achieved by using various code rates. The BER results demonstrated that T-OFDM systems can provide a substantial performance gain with minimal redundancy. Conversely, due to the WHT involved in T-OFDM systems, the equalizer technique required is different than those used in conventional OFDM systems. Detailed analysis including real world test is presented in the next chapter.

CHAPTER 5

Equalization techniques for T-OFDM

As stated in section 4.3.2.3, due to the spreading property of the T-transform, each channel coefficient affects all of the transmitted symbols. As a result, one bad coefficient will have an effect on the BER performance of the entire received signal as it creates an extra 'noise floor'. This chapter focus on the design of a novel modified ZF equalizer which deals with the pernicious noise enhancement effect, along with real world test results.

5.1 Modified ZF Equalizer with Outlier Deletion

MMSE channel equalizer provides a good level of noise suppression in UWA channels. However in order to reach its full potential, an accurate estimate of the noise variance need to be provided with the received signal. Due to the fast-changing nature of UWA channels, it is difficult to track the channel variation and measure the noise variance at the same time. In this thesis, we proposed a modified ZF channel equalizer which eliminates the noise enhancement by identifying and replacing the null channel taps. General channel nulls will result in extreme values in the reciprocal of the estimated channel vector. Hence the extreme values can be identified as outliers and then be eliminated. However, as the accuracy of outlier detection methods is heavily determined by its statistical distribution model, therefore choosing the appropriate outlier detection algorithm is key in this case [78] [79]. The Walsh's Outlier [78] is chosen as it does not require a normally distributed set of data input (other tests such as Grubb's outlier test require normal distribution on the input). When calculating outlying observations,

tables of critical values are usually given for several different significance levels, for example, 5%, 1%. For statistical tests of outlying observations, it is generally recommended that a low significance level, such as 1%, be used and that significance levels greater than 5% should not be common practice [115]. In our application, the significance level should not be set too low, as such low significance level will take out too many coefficients from the channel estimate, resulting in a severe degradation in BER performance. Although it requires at least 60 samples to be performed at a significance level of $\alpha = 0.05$ (A Type I error occurs when the researcher rejects a null hypothesis when it is true. The probability of committing a Type I error is called the significance level, and is often denoted by α). Those requirements are well justified in this case as the length of the estimated channel responses are much longer than 220 samples (requirement for calculating outlier with Walsh's outlier model [78]) with a FFT size of at least 512. Bear in mind that in order to compute the Walsh's outlier test, a number of k suspected outliers has to be given. In the proposed system, we pre-set the number of k from 0-100 and calculates the following equations:

$$c = ceiling\left(\sqrt{2n}\right)$$

$$r = k + c$$

$$b^2 = \frac{1}{\alpha} \tag{5.1.0}$$

$$a = \frac{1 + b\sqrt{\dfrac{(c - b^2)}{c - 1}}}{c - b^2 - 1}$$

Where $ceiling(.)$ indicates rounding the value to the next largest integer. The k largest points of the input X are outliers with an α level of significance if

$$X_{(n+1-k)} - (1 + a)X_{(n-k)} + aX_{(n+1-r)} > 0 \tag{5.1.1}$$

After trying all number of k, the outlier set with largest k is selected and the outliers are replaced by interpolating the neighboring taps. The equalizer taps are updated correspondingly and the equalized signal is then passed to the soft decoder. By identifying and replacing the channel nulls, the modified ZF channel equalizer greatly reduces the noise enhancement effect. The performance of the modified ZF equalizer is verified in the next section.

5.2 Numerical Results

The performance of the proposed T-OFDM system with modified ZF channel equalizer in comparison to conventional OFDM system is validated in this section. Note that although the T-transform reduces the computational cost at the transmitter side as it no longer requires a separate calculation of WHT and IFFT, however, the performance of both WHT precoded OFDM and T-OFDM is identical as the performance improvement in T-OFDM systems is provided by WHT. Also note that, by implementing the T-transform at the transmitter, conventional pilot based channel estimation can no longer be performed as pilot symbols can only be inserted in the Walsh domain instead of frequency domain as in conventional techniques. As a result, in order to establish a fair comparison between T-OFDM and OFDM systems with the modified ZF equalizer, WHT-OFDM is adopted in all testing sections, as pilots can be inserted in the frequency domain after WHT as it was in conventional OFDM systems. Also, the WHT-OFDM system is tested compared to a code-spread OFDM system which adopts the discrete cosine transform (DCT) as a precoder. The DCT-OFDM is chosen here as it also provides some level of extra frequency diversity without sacrificing any bandwidth efficiency through frequency domain spreading [40] [108]. The basic structure of DCT is presented next.

5.2.1 Discrete Cosine Transform

A discrete cosine transform expresses a finite sequence of data points in terms of a sum of cosine functions oscillating at different frequencies. In UWA channels, this characteristic makes DCT especially effective at de-correlating the transmitted signal, leaving an output with maximum variance in the last number of transform coefficients [108]. The even symmetric DCT (also known as DCT II) is the most commonly used form. The DCT of $x[n]$ is defined as follows [108]:

$$w(k) = \begin{cases} 1/2; & k = 0 \\ 1; & 1 \le k < N \end{cases}$$

$$C_x[k] = \begin{cases} \sum_{n=0}^{N-1} 2x[n]\cos(\dfrac{\pi}{2N}k(2n+1)); & 0 \le k < N \\ 0; & otherwise \end{cases}$$

$$x[n] = \begin{cases} \dfrac{1}{N}\sum_{n=0}^{N-1} w[k]C_x[k]\cos(\dfrac{\pi}{2N}k(2n+1)); & 0 \le k < N \\ 0; & otherwise \end{cases} \tag{5.2.0}$$

One advantage of using the DCT as spreading code is that it enables computational efficient demodulation due to the use of efficient DCT at the receiver. Next, performance comparison of the WHT-OFDM to conventional OFDM and DCT-OFDM with modified ZF equalizer is presented in the following section.

5.2.2 Experimental Design

The tested system is designed based following the principles as in section 4.4.1, where the transmitted packet is generated in a burst fashion as shown in Figure 5.1.

| silent period | Packet N = 512 | silent period | Packet N = 1024 | silent period | Packet N = 2048 | silent period |

| Up-chirp | T-OFDM | Down-chirp1 | DCT-OFDM | Down-chirp2 | OFDM | Up-chirp |
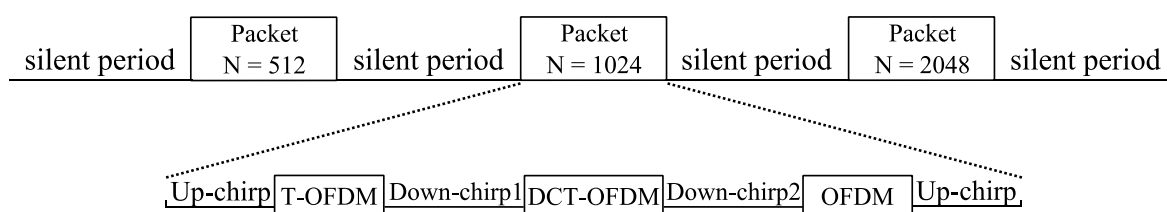
Figure 5.1: Burst data structure.

Packets within burst are generated by concatenating blocks of T-OFDM signal with OFDM signal. Those three blocks are separated by different type/length header chips as depicted in Figure 5.1. Silent periods of 20ms are inserted between neighboring packets which not only serve as guard bands but also can be used to measure noise variance. Data bursts are sent through the channel continuously during the test. The header chips are also used for Doppler spread compensation. The details are explained next.

5.2.3 Doppler Spread Computation

In order to successfully decode the received signal, the Doppler spread must be dealt with first. As the method of measuring the Doppler spread by observing the packet compression/dilation is proven to be efficient in the previous systems ([107] etc.), similar block estimation technique is used here. Packet structure is shown in Figure 5.2. Chirp signal is implemented as headers of each packet due to its strong Doppler tolerant property. The length of the received block can

then be measured from the cross-correlation output of the chirp signal and the received data packet as in Figure 5.2.

As can be seen from the cross-correlation output, multiple peaks appear with the existence of multipath propagation. Distances between the corresponding peaks manifest the Doppler rate for each path. Here the distance between the first arrivals is measured as the dominant Doppler

| Chirp Signal | kth Data Packet | Chirp Signal | · ···· | Chirp Signal | (k+m)th Data Packet |
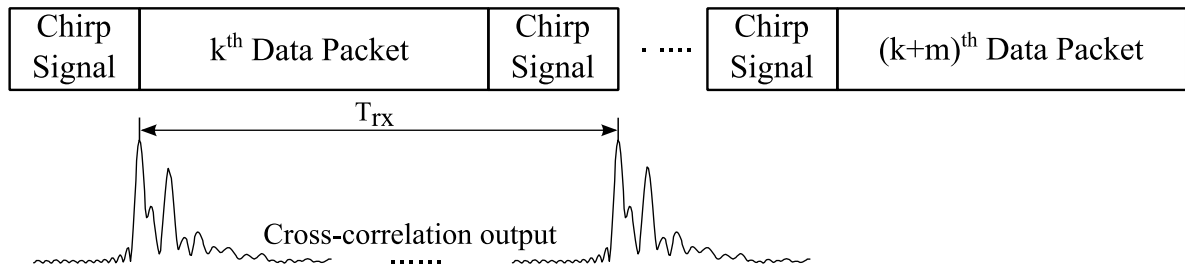
Figure 5.2: Cross-correlation output

shift. When compared to the a prior information of the transmitted packet length T_{tr} , the estimated Doppler shift can be represented as

$$\hat{a} = \frac{T_{rx}}{T_{tr}} - 1 \qquad (5.2.1)$$

This measured Doppler is then utilized to perform the sampling rate conversion. This process is performed on the passband signal, although resampling on the baseband is also viable. The designed system is then tested in a water tank.

5.2.4 Water Tank Test Results

The proposed system is first tested in a water tank with approximate dimensions of 3m long, 2m wide and 2m deep. A certain degree of channel variability is attained by stirring the tank water. Two data packets are generated for this experiment. Data packet is generated following Figure 5.1. Performance alteration between T-OFDM. DCT-OFDM and OFDM are further investigated. During the test, a two-minute long wav file is recorded which contains roughly 30 packets for each FFT size. Since the proposed receiver works on a block-by-block base, each packet is then treated separately. BER plots are generated by adding additive white Gaussian noise onto the received packets based on the measured symbol energy. First, a measured channel
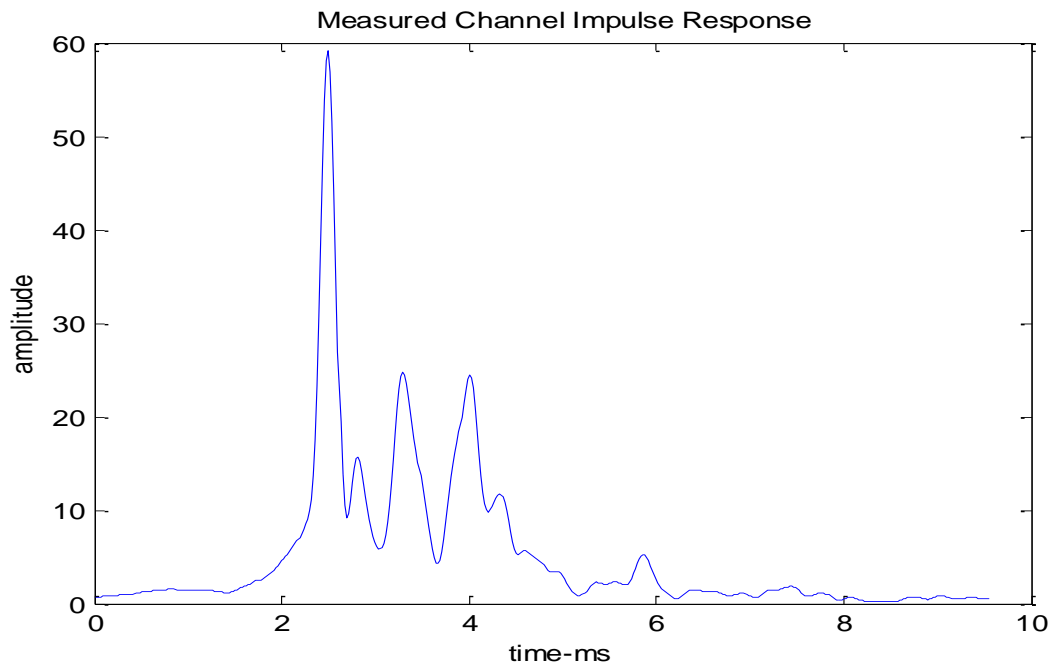
Figure 5.3: Measured channel impulse response of the tank.
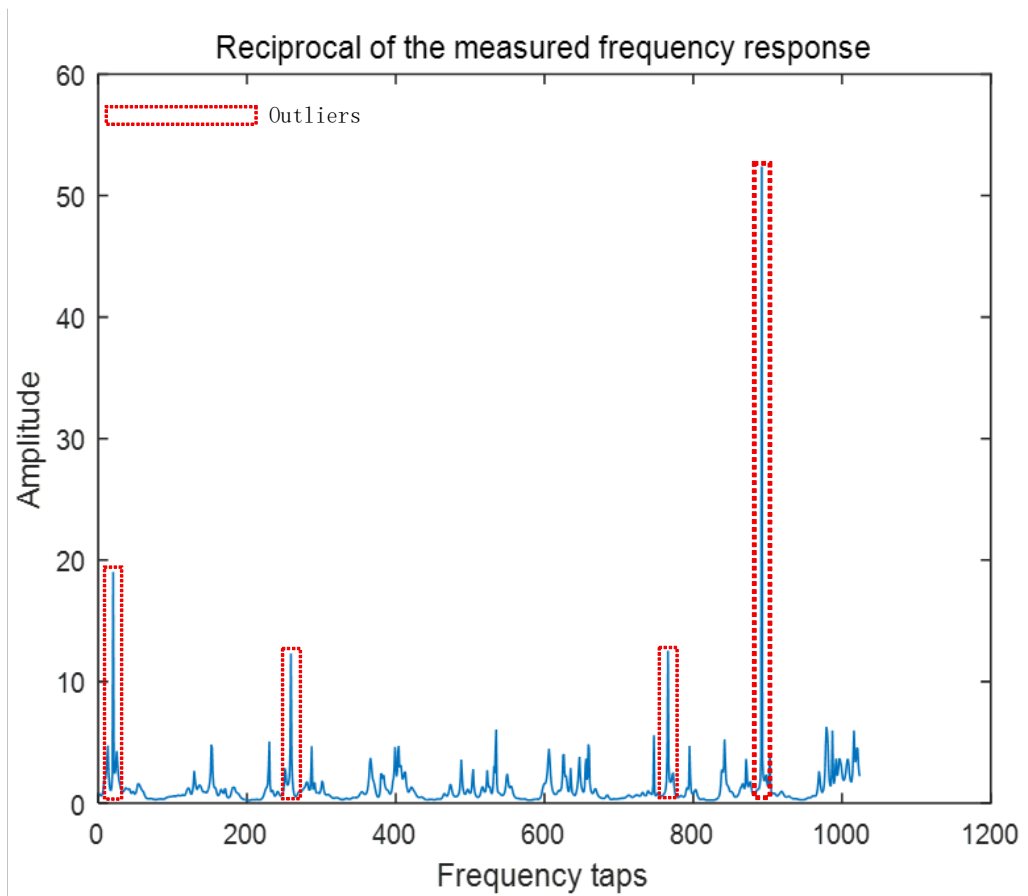
Figure 5.4: Outliers in reciprocal of measured channel frequency response.

impulse response is given in Figure 5.3. The effectiveness of the proposed channel equalizer with outlier deletion is demonstrated next. For the typical impulse response measured in Figure 5.3, the reciprocal of the corresponding measured channel frequency response is shown in Figure 5.4.

Those outliers are generated from channel nulls in the channel frequency response. After identifying those outliers, a modified version of channel frequency response is generated by replacing outliers in the reciprocal by the mean values of the taps before and after the outlier. The corresponding response of Figure 5.4 after replacing the outliers is shown in Figure 5.5.
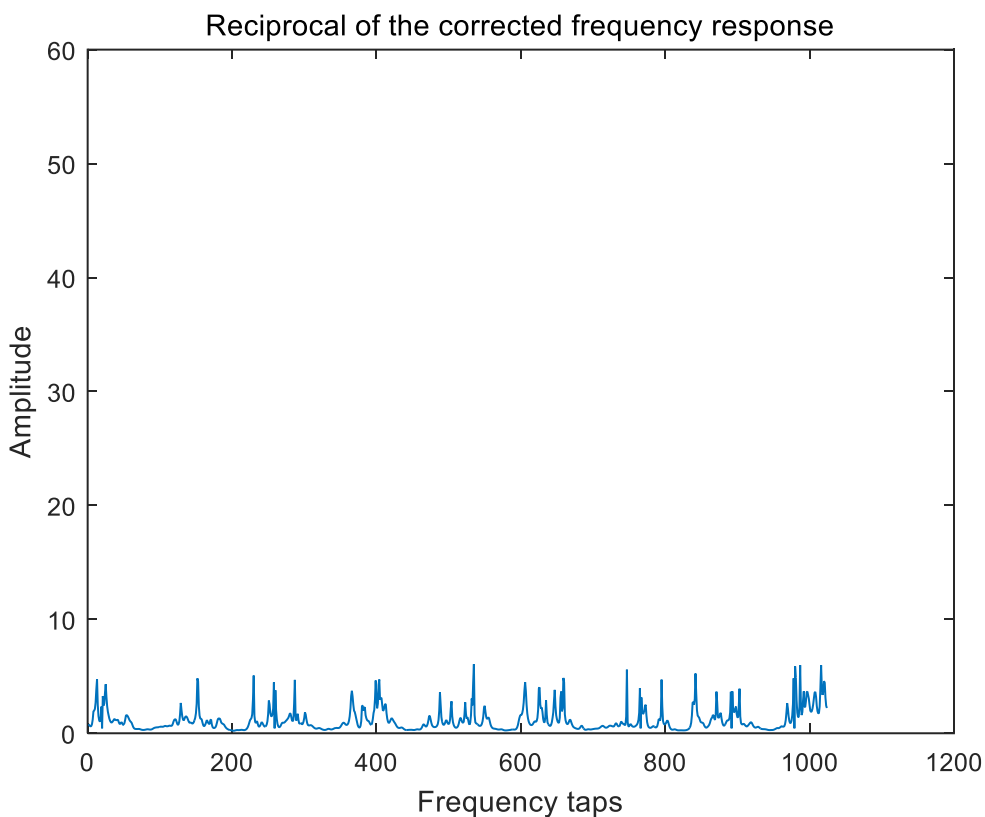
Figure 5.5: Reciprocal of corrected channel frequency response.

Next, the BER performance of OFDM and TOFDM systems with and without the modified ZF equalizer are compared. Packets containing both OFDM and T-OFDM systems with three different FFT sizes are transmitted through the water tank. For each FFT size, systems with the perfect channel estimate (artificially derived from the noise free signal) are used as a reference in order to indicate how far away does the modified ZF equalizer get to the performance with a perfect channel estimate. The results are presented in Figure 5.6-5.8.
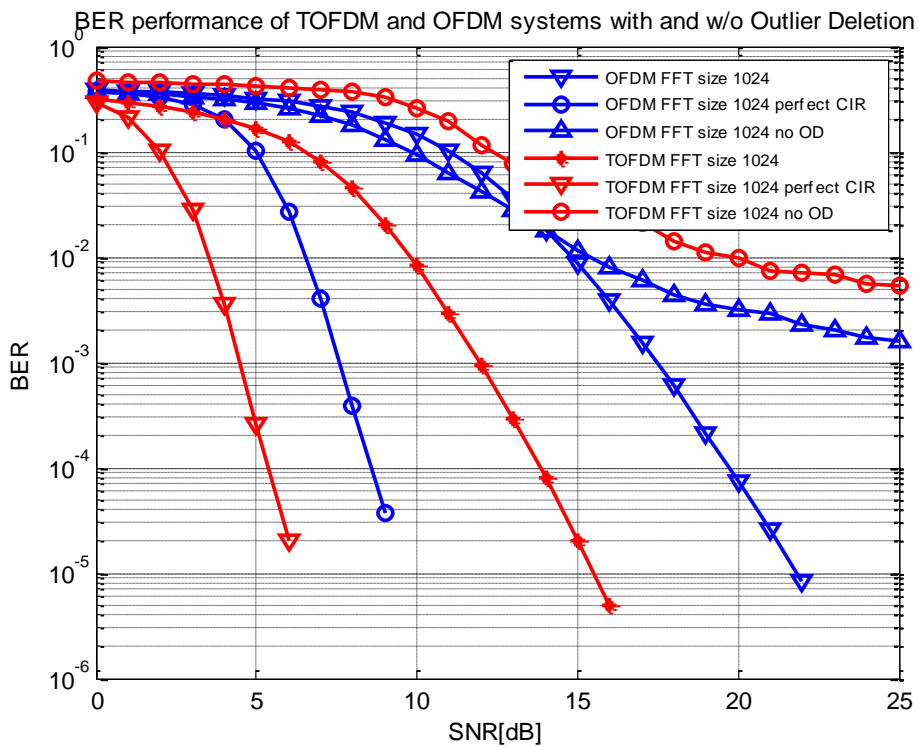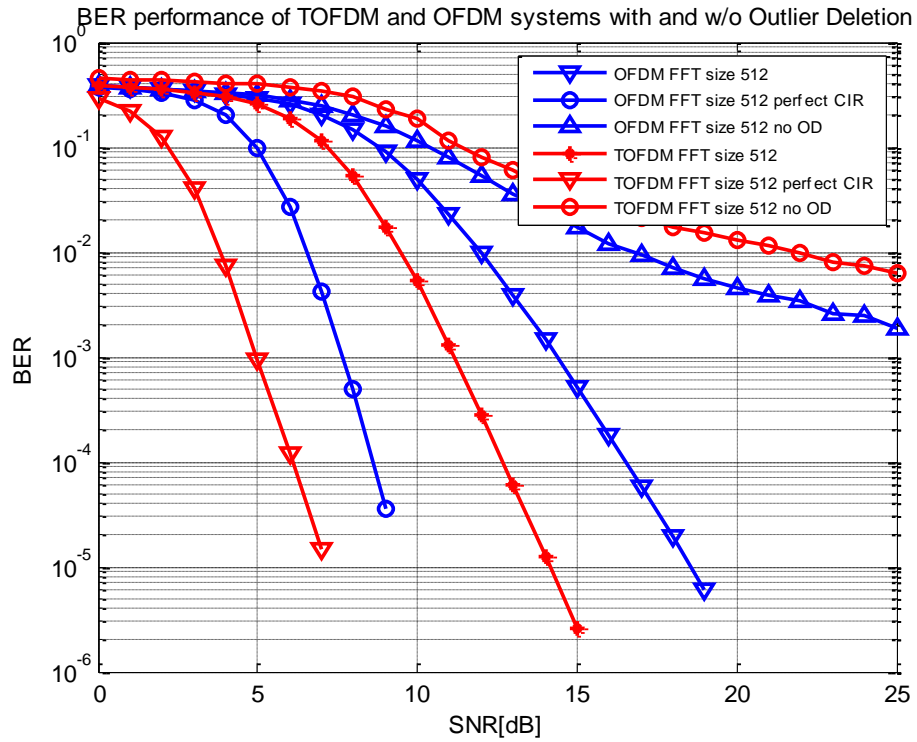
Figure 5.6/5.7: BER performance of OFDM and TOFDM systems with and without the modified ZF equalizer comparing to systems with perfect channel knowledge for FFT size of 512 and 1024.
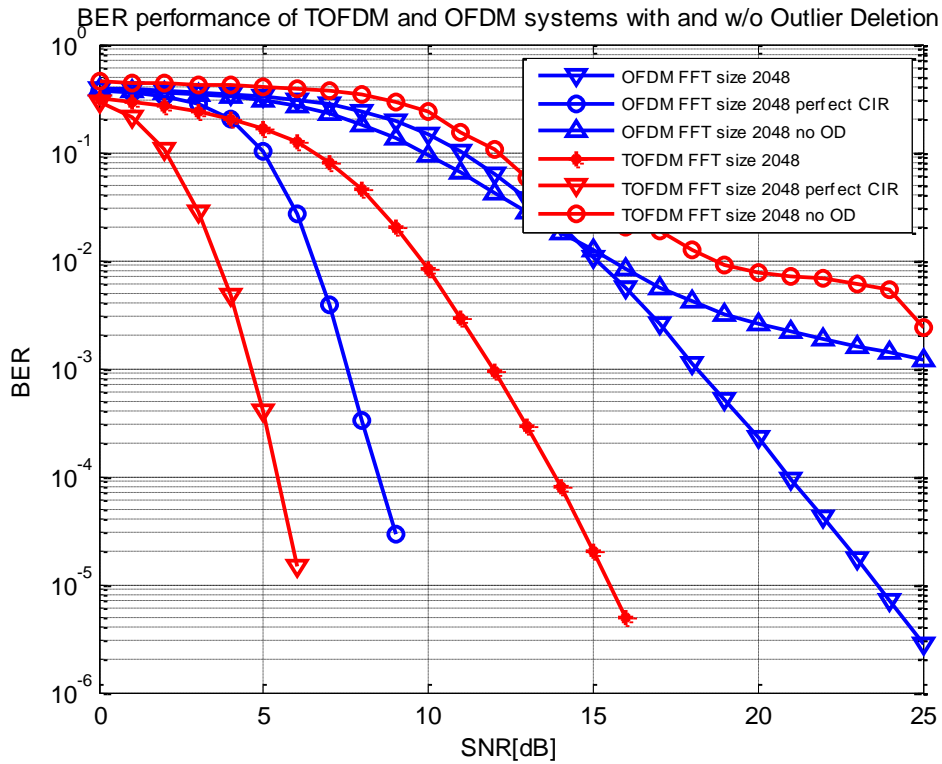
Figure 5.8: BER performance of OFDM and TOFDM systems with and without the modified ZF equalizer comparing to systems with perfect channel knowledge for FFT size of 2048.

Results shown in Figure 5.6-5.8 clearly demonstrated that T-OFDM is superior to OFDM for systems with perfect channel knowledge and systems with the modified ZF equalizer across all three FFT sizes. On the other hand, the BER performance of T-OFDM systems dropped significantly and fall behind of OFDM systems when not implementing the modified ZF equalizer. Those results emphasizes the importance of outlier deletion in the proposed T-OFDM systems. As a result, a modified ZF equalizer is required in order for T-OFDM systems to fully utilize its advantage of providing extra system diversity without losing any throughput.

With the above findings in mind, the packets generated following Figure 5.1 is sent through the tank channel. BER versus SNR plots with different FFT sizes are shown in in Figure 5.9-5.11. Performance of systems with and without the modified ZF channel equalizer are also compared.
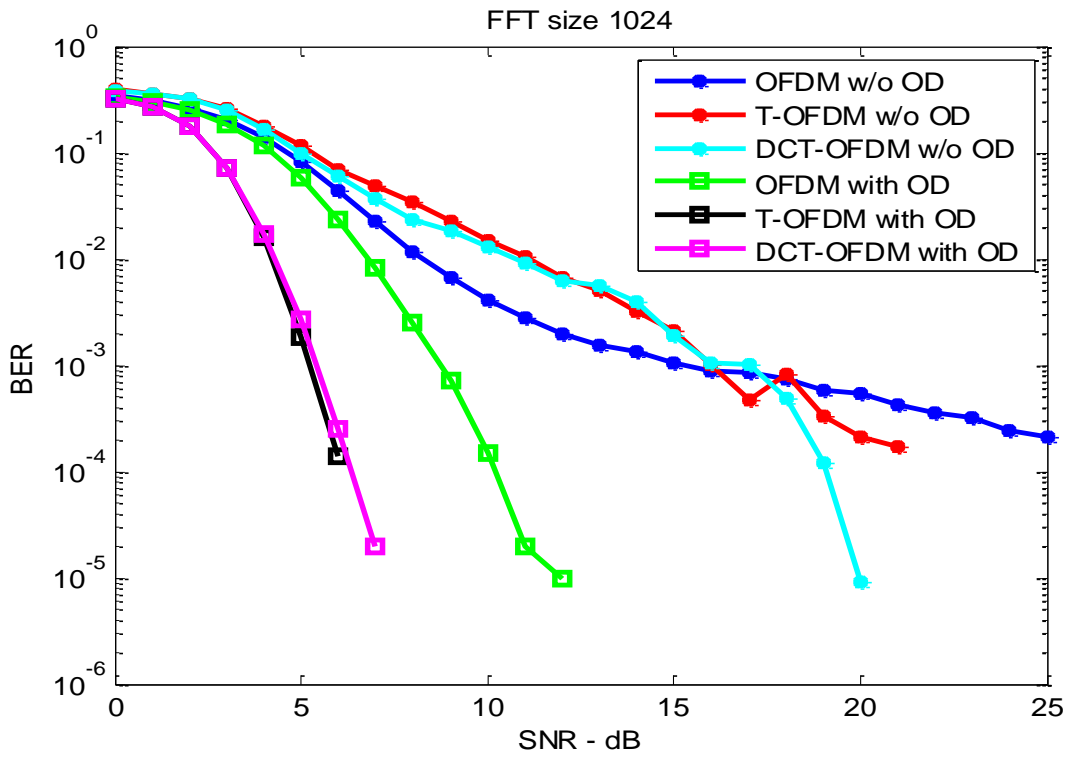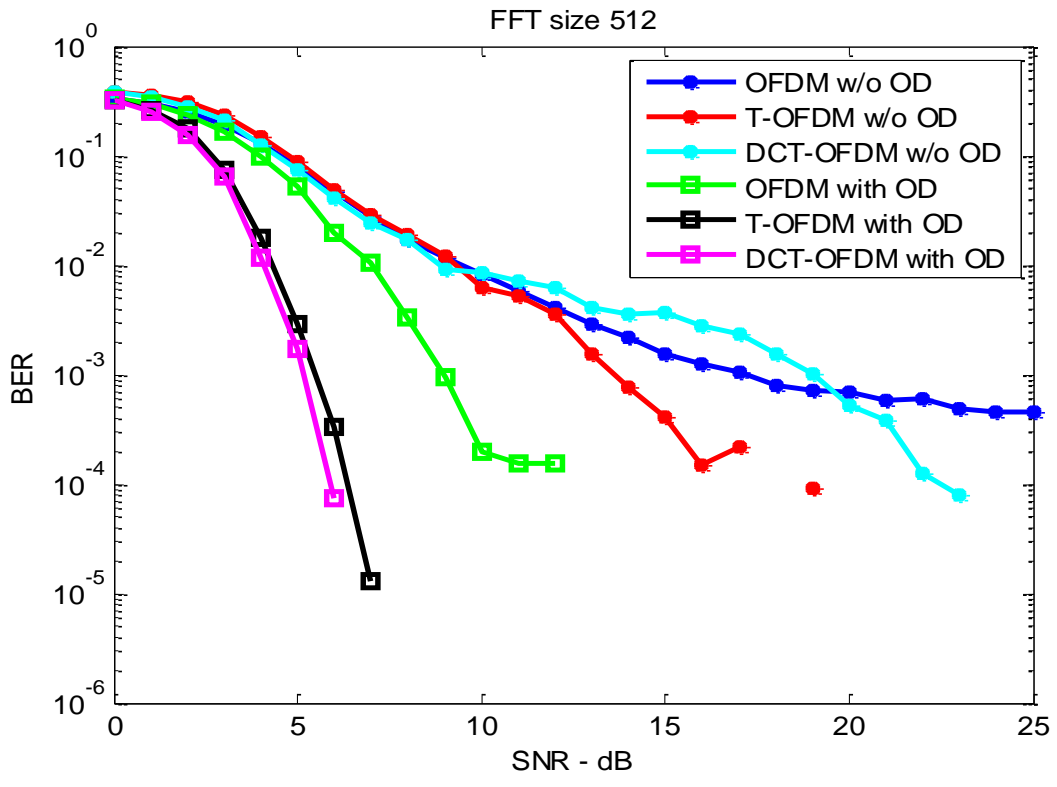
Figure 5.9/5.10: BER performance with FFT size of 512/1024.
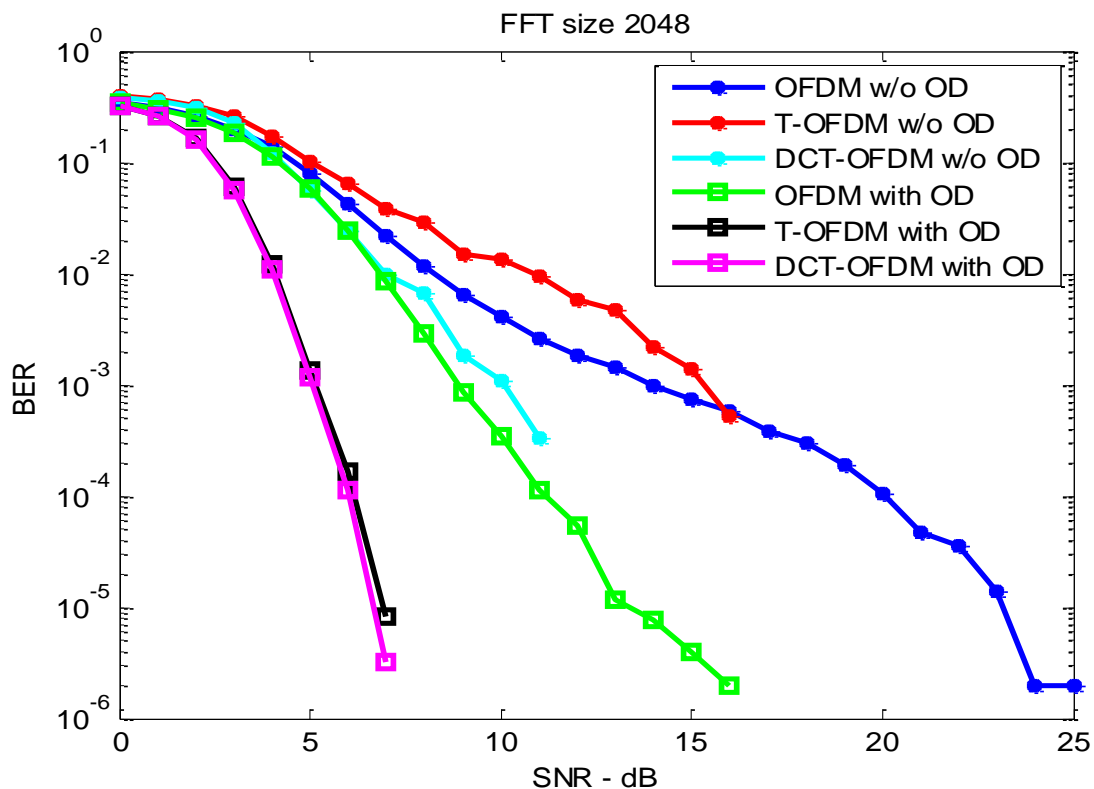
Figure 5.11: BER performance with FFT size of 2048.

BER results in Figure 5.9-5.11 revealed that both T-OFDM and DCT-OFDM outperform conventional OFDM significantly in all three cases with outlier deletion. Conversely, similar performance is observed between T-OFDM and DCT-OFDM. On the other hand, the importance of implementing outlier deletion as a noise suppression method is apparent. In the cases of 512 length FFT and 1024 FFT, both T-OFDM and DCT-OFDM system perform worse than or close to OFDM systems in the medium to low SNR scenarios without outlier deletion due to noise enhancement. However, in the case of 2048 FFT, the BER performance gap between systems with and without outlier deletion is shortened as the amount of noise enhancement is alleviated through averaging over a longer packet length.

5.2.5 Sea Trial Results

This sea trial was conducted on March 18, 2015, roughly two nautical miles east of the Blyth coast in the North Sea, UK. The transmitter was towed by the side of research vessel Princess Royal with a depth of about 15 m and the receiver hydrophone was towed by vessel JFK TWO at a depth of about 6 m. Figure 5.12 shows the dock area (where equipment are placed) and an overview of research vessel Princess Royal.

Figure 5.12: Dock area and overall size of research vessel Princess Royal.

Experiments are started with two research vessels ranged at 500m then slowly (relatively speed is approximately 5-8 knots) driving towards each other, then driving away from each other again. To test the performance limitation of the proposed system, packets are generated only containing FFT sizes of 512 and 2048 in order to validate the aforementioned relationship between the performance of channel equalizer and channel's frequency diversity. Two sets of recordings (with four-minute length each) are obtained at distances of approximately 500m and 2km. The sea depth remains approximately 35m during all recordings. Numerical results are presented next with a selected set of results and comparisons.

5.2.5.1 Doppler Scaling Factor Estimation

The algorithm described in Section 5.2.3 was used to estimate the Doppler scaling factor for each of the received block. After obtaining the Doppler scaling factor, the relative speed between the transmitter and receiver can be estimated using a nominal sound speed of $c = 1500$ m/s.   For the packet with FFT size of 2048, the results from 500m and 2km are shown in Figure 5.13. Within Figure 5.13, the relative speed measured at packets numbered as 15, 22, 51 and 56 are abnormally high. That is because during the recoding of received data, we accidentally left the boat's depth sounder on, which caused a significant noise like interference on received packets. As a result, the received packets have a much higher noise floor (the frequency the depth sounder uses is roughly 12 kHz which is within the frequency range used in data transmission). Because the accuracy of the Doppler estimation technique greatly relies on the accuracy of packet duration estimation, the extra added noise floor may cause inaccurate

measurement of the Doppler Effect. When plotting Figure 5.13, we could remove the irregular data sets from calculating and plotting the relative speed. However, for the sake of consistency and fairness of the experiment, we decided to keep those 'rogue' data in while explaining the possible causes of them.   We can see that with a maximum relative speed exceeding -1.3m/s, the Doppler shift at the edge of the band (16000Hz) is roughly -13.9Hz which is much larger than the frequency spacing Δf (3.91Hz for FFT size of 2048). As a result, rescaling the received packet is essential to mitigate the Doppler spread in the frequency domain. However, we should note that the accuracy of the sampling rate conversion method is highly dependent on the measuring interval at the receiver as the assumption that the Doppler spread is uniform across the received packet no longer holds true with an increased packet length. Measuring and compensating for the residual Doppler shift in a non-uniform case can be achieved with inserted null subcarriers as in [109], with a penalty of reduced bandwidth efficiency. Even though the accuracy of rescaling can be improved by carefully designing the transmitted packets.   Figure 5.14 illustrates the system performance with and without sampling rate conversion for T-OFDM packets received at 2000m with a FFT size of 512.
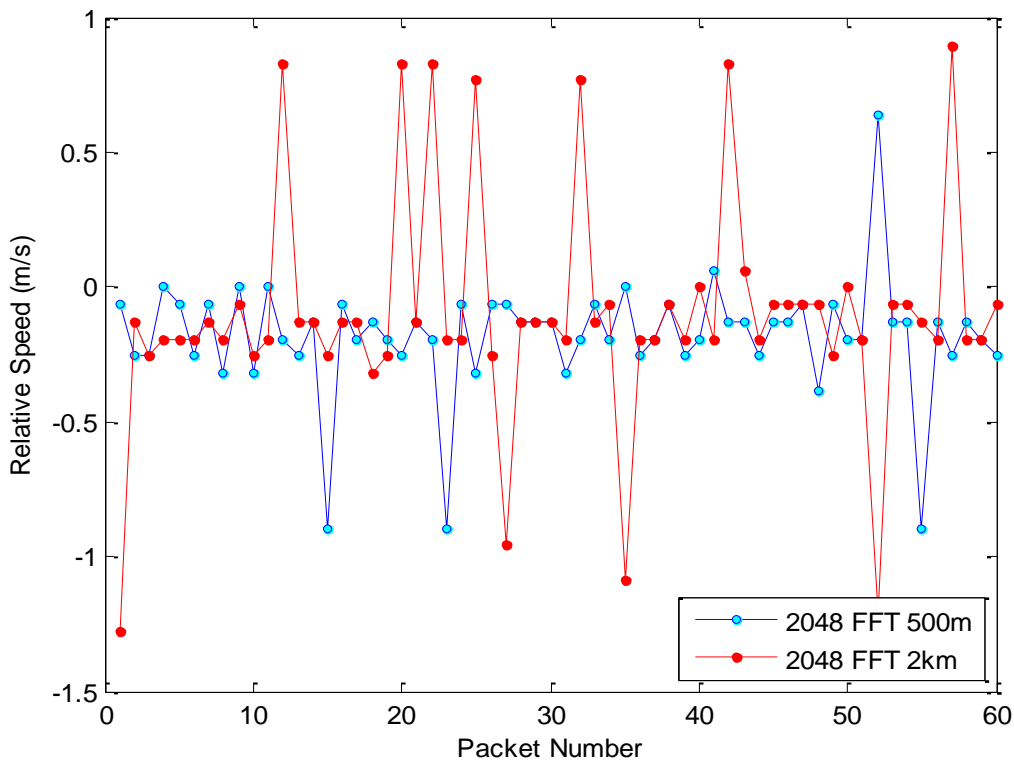
Figure 5.13: Estimation of the relative speed at distance of 500m and 2km.
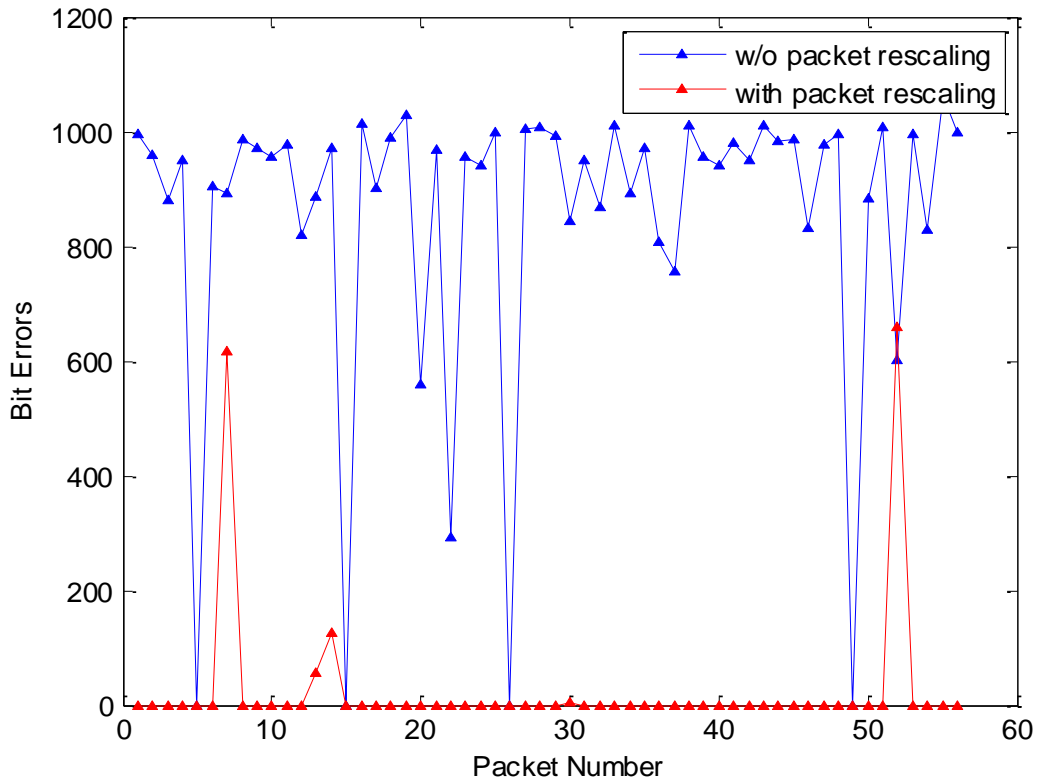
Figure 5.14: Packet bit errors of systems with and without Doppler correction with FFT size of 2048 recorded at 500m.

5.2.5.2 Channel Estimation

We started recording at a distance of 500m with a channel variation shown in Figure 5.15. The dots in the plot represents energy level. The measured channel response at 500m and 2000m are shown in Figure 5.16. The medium distance channel will usually offer a good trade-off between the channel difficulty and received SNR. The overall delay spread is roughly 6ms. Another data set recorded at a distance of 2000m revealed a calm channel with minimal multipath and a low noise floor. The reason is that with increased range, the transmitted wave bends upward to the receiver instead of hitting the sea bottom, producing much less multipath, therefore offers the best channel condition overall. We choose FFT size of 512 recorded at a range of 2000m to demonstrate the performance difference between systems with and without implementing the proposed ZF channel estimator. The corresponding block error rate (BLER) results are presented in Table 5.1. We chose BLER as our performance criterion here because it illustrations a more comprehensive view on the overall performance of the system across every received packets. From Table 5.1 we can see that although limited by the noisy nature of the

channel (the difficulty of identifying the outliers from non-outlier date points increases), the proposed ZF equalizer worked better with T-OFDM system rather than DCT-OFDM system.
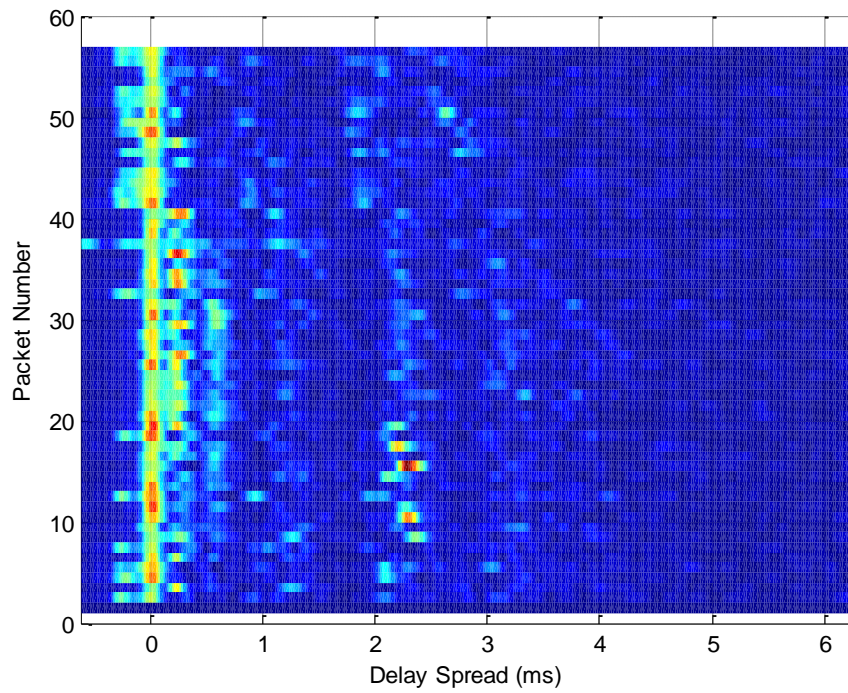
Figure 5.15: Channel variation from recording taken at 500m.

Table 5.1 BLER Performance of the Modified ZF Estimator

Schemes	With Outlier Deletion	W/O Outlier Deletion
T-OFDM	0.075	0.103
DCT-OFDM	0.246	0.260
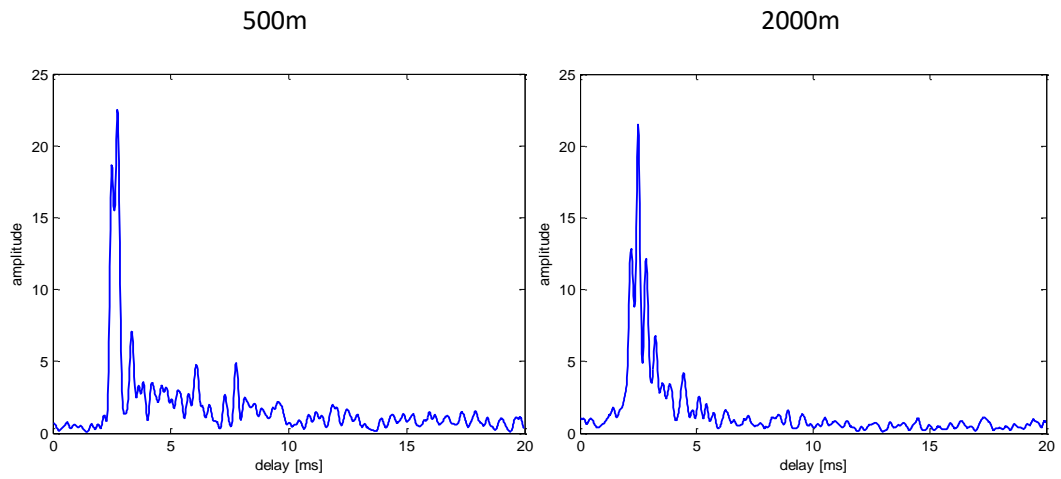
Figure 5.16: Measured channel impulse response at two distances.
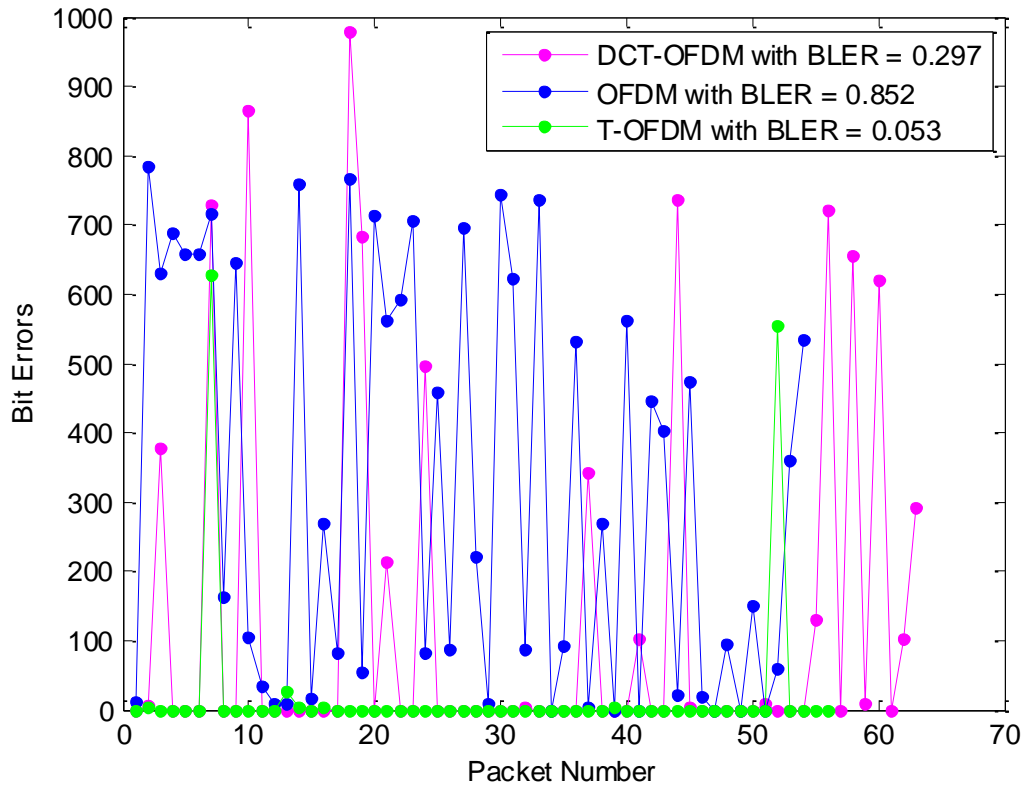
Figure 5.17: Packet bit errors with FFT size of 2048 recorded at 500m.

5.2.5.3 BLER Performance

BLER performance for all recordings is shown in Table 5.2 with Figure 5.17 showing one set of results. It is clear that the proposed T-OFDM system continuously outperformed both DCT-OFDM and OFDM system. It is also clear that for channels with longer delay spreads (500m), systems with longer FFT performed better as it increased the system robustness against delay spreads. Nevertheless in a channel with less multipath (2000m), performance of systems implementing 512 FFT are superior as they better utilized channel's frequency diversity.

Table 5.2 BLER Performance at Different Locations

FFT	Scheme	500m	2000m
512	T-OFDM	0.541	0.075
	DCT-OFDM	0.922	0.246
	OFDM	0.979	1
2048	T-OFDM	0.053	0.500
	DCT-OFDM	0.297	0.546
	OFDM	0.852	0.974

5.3 Chapter Conclusion

In this Chapter, we investigated the performance of different channel equalizers for conventional OFDM and the proposed T-OFDM system. A modified ZF channel equalizer is proposed in order to suppress the detrimental noise enhancement effect. Performance of the proposed equalizer is tested in both water tank and via sea trial in comparison to DCT-OFDM system and conventional OFDM system. The proposed system revealed better performance in UWA channels whilst retaining multipath resilience without any data rate loss. A modified ZF equalizer was implemented in the above systems which alleviated noise enhancement. Performance was tested in both water tank and the North Sea with achieved data rates of 6.1kb/s, 6.92kb/s and 7.43kb/s using rate 2/3 channel coding. Experimental results state that with little redundancy the proposed system outperformed both DCT-OFDM and OFDM systems in a fast fading channel. On the other hand, the modified ZF equalizer was revealed to be more effective in T-OFDM systems than DCT-OFDM systems. Therefore, as T-OFDM system revealed overall superiority against DCT-OFDM, this type of pre-coded OFDM system is ruled out for comparison in the remaining sections of this thesis. The optimal PAPR reduction method for the proposed system in underwater communication channel is evaluated in the next chapter.

CHAPTER 6

PAPR Reduction

Owing to subcarrier overlapping, the transmitted OFDM signal can have high peak values in the time domain. As a result, OFDM systems are known to have high Peak-to-Average Power Ratio (PAPR). The high PAPR is considered as one of the most detrimental aspects in the OFDM systems, as it decreases the Signal-to-Quantization Noise Ratio (SQNR) of ADC and DAC while degrading the efficiency of the power amplifier at the transmitter. The high PAPR problem is even more important for low power UWA communication devices since the efficiency of power amplifier is critical due to the limited battery energy. In this section, the PAPR of T-OFDM and conventional OFDM are analyzed. Different PAPR reduction methods are compared and the one with the best BER performance for a given limit on peak power (a constraint of the underwater modem hardware) is chosen for the proposed system.

6.1 Effect of PAPR on PA

In general, even linear amplifiers impose a nonlinear distortion on their output due to their saturation characteristics caused by an input much larger than its normal value [81]. A typical input-output characteristics of a PA in terms of the input power P_{in} and the output power P_{out} can be represented in Figure 6.1. Due to the saturation characteristic of the amplifier, the maximum possible output is limited by P_{out}^{max} when the corresponding input power is given as P_{in}^{max}. Therefore, as can be seen from Figure 6.1, the input power must be backed off in order to allow the PA working within the linear range. Consequently, the nonlinear range can thus be

described by IBO (Input Back-Off) or OBO (Output Back-Off), where IBO and OBO is expressed as [82]:

$$IBO = 10 \log_{10} \frac{P_{in}^{max}}{P_{in}}, \; OBO = 10 \log_{10} \frac{P_{out}^{max}}{P_{out}} \tag{6.1.0}$$
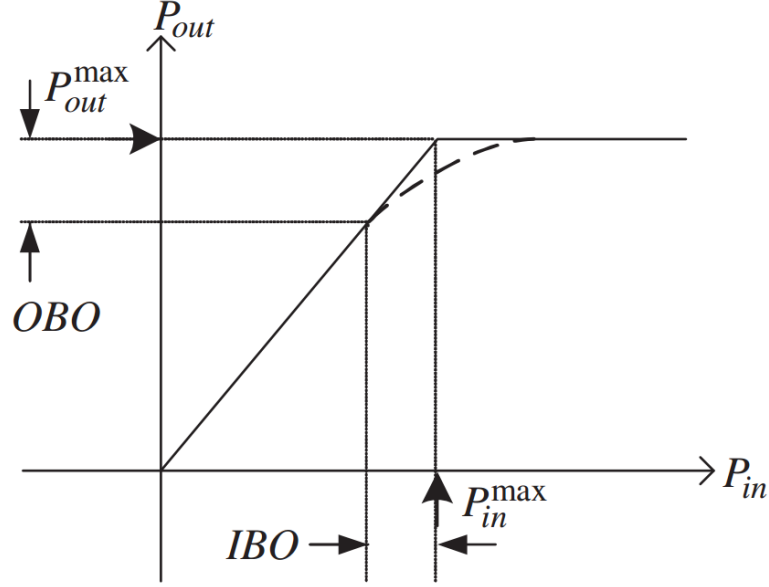
Figure 6.1: The input-output characteristic of an PA.

6.2 Definition of PAPR

Consider a baseband pulse amplitude modulation (PAM) signal for a complex data sequence $d[n]$

$$\hat{s}(t) = \sum_k d[n]g(t - kT_s) \tag{6.2.0}$$

Where $g(t)$ is a transmit pulse for each symbol and T_s is the symbol duration. The passband quadrature modulated signal can then be expressed as:

$$s(t) = \sqrt{2}\mathbf{Re}\{(\hat{s}_I(t) + j\hat{s}_Q(t))e^{j2\pi f_c t}\} \tag{6.2.1}$$

Where $\hat{s}_I(t)$ and $\hat{s}_Q(t)$ denote the in-phase and quadrature components of the complex baseband PAM signal $\hat{s}(t)$ respectively ($\hat{s}(t) = \hat{s}_I(t) + j\hat{s}_Q(t)$).

PAPR is the ratio between the maximum power and the average power of the complex passband signal $s(t)$ [83] that is

$$PAPR\{\hat{s}(t)\} = \frac{\max|\mathbf{Re}(\hat{s}(t)e^{j2\pi f_c t})|^2}{E\{|\mathbf{Re}(\hat{s}(t)e^{j2\pi f_c t})|^2\}} = \frac{\max|s(t)|^2}{E\{|s(t)|^2\}} \qquad (6.2.2)$$

By defining the crest factor (CF), the above power characteristic can be described in terms of magnitudes as

$$\text{Passband condition:} \, CF = \sqrt{PAPR}$$

$$\text{Baseband condition:} \, CF = \sqrt{PMEPR}$$

(6.2.3)

Where PMEPR denotes the Peak-to-Mean Envelope Power Ratio (PMEPR) which is the ratio between the maximum power and the average power for the envelope of a baseband complex signal. Hence, the PMEPR is denoted as

$$PMEPR\{\hat{s}(t)\} = \frac{\max|\hat{s}(t)|^2}{E\{|\hat{s}(t)|^2\}} \qquad (6.2.4)$$

For OFDM signal with N subcarriers, the maximum power appears when all of the subcarriers are added with identical phases. Assuming $E\{|s(t)|^2\} = 1$, it results in $PAPR = N$ that is, the maximum power is equivalent to N times the average power. Note that, more PAPR is expected for M-QAM with $M > 4$ than M-ary PSK. Also, the probability of the occurrence of the maximum power signal decreases as N increases [84].

6.3 PAPR Distribution of OFDM System

The PAPR defined in (6.2.2) describes the passband signal with a carrier frequency of f_c in the continuous time domain. Since f_c in general is much higher than $1/T_s$, a continuous time baseband OFDM signal $x(t)$ with the symbol period T_s and the corresponding passband signal $\bar{x}(t)$ with the carrier frequency f_c have almost the same PAPR [84]. However, the PAPR for the discrete-time baseband signal $x[n]$ may not be the same as that for the continuous-time baseband signal $x(t)$. In fact, the PAPR for $x[n]$ is lower than that for $x(t)$ as $x[n]$ simply may not have all peaks of $x(t)$. In practice, the PAPR for the continuous-time baseband signal can be measured only after implementing the actual hardware, including digital-to-analog convertor (DAC). Conversely, $x[n]$ can show almost the same PAPR as $x(t)$ if it is L-times oversampled with $L>4$ [85]. Therefore, the PAPR for the discrete-time signal can be rewritten as

$$PAPR[x_n] = \frac{\varsigma_{max}}{\varsigma_{average}} \tag{6.3.0}$$

Where $\varsigma_{max} = \underset{0 \le n \le NL-1}{max}[|x_n|^2]$ is the peak power of the discrete-time signal x_n, and $\varsigma_{average} = E[|x_n|^2]$ is the average transmitted power, N is the number of the subcarrier, and L is the oversampling factor. In OFDM systems, oversampling can be done by padding the frequency-domain signal with $0^{1 \times (L-1)N}$. Similarly, the same approach can be used with a WHT-OFDM system, padding the WHT output signal with zeroes.

The T-transform allows for the preservation of the average transmitted power, thus, the average power for $\mathbf{x} = \overline{\mathbf{T}}\mathbf{X}$ can be calculated as

$$
\begin{aligned}
E\{|\mathbf{x}|^2\} &= E\{\mathbf{x}\mathbf{x}^*\} \\
&= E\{(\overline{\mathbf{T}}\mathbf{X})(\mathbf{T}\mathbf{X}^*)\}
\end{aligned} \tag{6.3.1}
$$

Where $\{.\}^*$ denotes the complex conjugate. Therefore, the n-th element of $|\mathbf{x}|^2$ can be written as

$$
\begin{aligned}
|x_n|^2 &= \left(\sum_{m=0}^{N-1} X_m \hat{T}_{m,n} \right) \left(\sum_{m=0}^{N-1} X_m^* T_{m,n} \right) \\
&= \left(\sum_{m=0}^{N-1} |X_m|^2 |\hat{T}_{m,n}|^2 \right) + \left(\sum_{m=0}^{N-1} \sum_{g=0,g \ne m}^{N-1} X_m X_g^* T_{m,n} T_{g,n}^* \right)
\end{aligned} \tag{6.3.2}
$$

Consequently, (6.3.1) can be rewritten as

$$E\{|\mathbf{x}|^2\} = \frac{1}{N} \sum_{n=0}^{N-1} \left(\sum_{m=0}^{N-1} |X_m|^2 |\hat{T}_{m,n}|^2 \right) + \frac{1}{N} \sum_{n=0}^{N-1} \left(\sum_{m=0}^{N-1} \sum_{g=0,g \ne m}^{N-1} X_m X_g^* T_{m,n} T_{g,n}^* \right) \tag{6.3.3}$$

Due to orthogonality of matrix $\mathbf{T}$, the second term on the right hand side of (6.3.3) is equal to zero. Hence, (6.3.1) can simply be written as

$$E\{|\mathbf{x}|^2\} = \frac{1}{N} \sum_{m=0}^{N-1} |X_m|^2 \tag{6.3.4}$$

Therefore, the average power is preserved by the T-transform, hence the PAPR reduction will depend on peak power reduction.

6.4 Optimal PAPR Reduction Techniques for T-OFDM system in UWA channels

6.4.1 PAPR Reduction Techniques

The PAPR reduction techniques can be categorized into the following approaches: clipping technique, coding technique, probabilistic technique, adaptive pre-distortion technique and DFT-spreading techniques [85]. In general, those approaches can be classified as techniques with distortion and without distortion.

For techniques with distortion, the peak of the transmitted signal is reduced by clipping the large peak depending on a specific threshold. These techniques have achieved simple and effective PAPR reduction, despite a noticeable BER degradation. Examples of these schemes are iterative clipping [86], filtering [87], and nonlinear companding [88].

On the other hand, distortion-less schemes can achieve a certain amount of PAPR reduction without BER degradation. However, the main drawback and performance threshold of such schemes are computational complexity and data rate loss, due to added redundant bits sent as side information. Typical distortion-less techniques including tone reservation, active constellation extension (ACE) [88], coding technique [89], selective mapping (SLM) [90]-[95], and partial transmitting sequences (PTS) [96-100].

Among the mentioned methods, SLM and PTS schemes have received substantial interest in conventional OFDM systems due to their ability of suppressing PAPR without suffering from BER degradation. However, the trade-off between BER degradation and transmission efficiency and computational complexity are the main limitations of such techniques due to the required side information to be transmitted. In order to reduce the loss in transmission rate, [101] [102] [103] have proposed different methods to solve the side information challenge inherent in SLM and PTS schemes by utilizing a variety of techniques at the expense of additional complexity.

On the other hand, the high computational cost of these techniques is mainly introduced due to the necessity of performing several IFFT operations and phase optimizations at the transmitter. Many studies were conducted to reduce the required computational burden of the SLM and PTS techniques, examples can be found in [90]-[100]. However, those systems all come up with

trade-offs. For SLM systems, the burden of complexity is reduced in cases of similar or inferior PAPR and BER performance. In OFDM-PTS systems, the complexity is reduced either by lowering the number of IFFTs, or by reducing the complexity of the phase optimizers, albeit with PAPR or BER degradation.

For WHT-OFDM systems, [104] proposed a method for PAPR reduction in multicarrier systems by combining SLM and dummy sequence iteration with WHT. The system achieved considerable PAPR reduction, although the computational complexity is also greatly increased due to the implementing of several IFFTs and WHTs. Additionally, [105] suggested a new PAPR reduction technique including WHT in conventional OFDM system, which provided good PAPR suppression at the cost of relatively high complexity requirement due to added WHTs in cascaded format.

Before evaluating the performance of different PAPR reduction techniques on the proposed system, the characteristic of T-OFDM system is first analyzed in the following.

A typical OFDM system can be obtained by applying IFFT to a randomly generated data symbol vector of length N, hence the baseband signal can be obtained as

$$d_n = \frac{1}{\sqrt{N}} \sum_{k=0}^{N-1} D_k \cdot e^{j2\pi\frac{n}{N}k}, \ \ n = 0, ..., N-1 \tag{6.4.0}$$

From above, the PAPR is defined as

$$PAPR_{d_n} = \frac{\max\limits_{0 \leq n \leq N-1}|d_n|^2}{\sigma_s^2} \tag{6.4.1}$$

Where $d_n \in D_N = \{d_0, ..., d_{N-1}\}$ is a modulated OFDM subcarrier, $\sigma_s^2 = \varepsilon\{|D_k|^2\}/N$ denotes average power, and L is the oversampling factor with $L=4$.

As IFFT operation can be considered as the process of first multiplying sinusoidal functions followed by summing and sampling the results. This high correlation property with IFFT input causes the sinusoidal functions to be arranged with in-phase form. After summing these in-phase functions, the output has a high probability of containing large amplitude which translates to high PAPR. For a discrete IFFT input sequence D_k, its autocorrelation function is given by

$$\rho_k = \sum_{n=1}^{N-k} D_{n+k} D_n^*, k = 0, \dots, N-1 \qquad (6.4.2)$$

The maximum value of its PAPR is then

$$\gamma \leq 1 + \frac{2}{N} \sum_{k=0}^{N-1} |\rho_k| \qquad (6.4.3)$$

Considering the proposed WHT-OFDM system, the IFFT input is first transformed by WHT, hence the corresponding autocorrelation function become

$$\rho_{WHT-k} = \sum_{n=1}^{N-k} (d_{[n+k]} \times \frac{W_N}{\sqrt{N}})(d_n \times \frac{W_N}{\sqrt{N}})^* \qquad (6.4.4)$$

With $k = 0, \dots, N-1$. As the peak value of the autocorrelation is the average power of the input sequence, the peak value depends only on the input sequence with a fixed FFT size. This means that the level of the correlation is dependent on the amplitude of the side lobe. As the WHT scrambles the input sequence before IFFT operation, the side lobe amplitude should be lowered than data fed directly through IFFT. This reduced autocorrelation property results in a lowered PAPR in a T-OFDM system. However, the degree of reduction become inconspicuous in a realistic UWA channel due to the noisy nature of the channel itself. Consequently, in order to fully exploit the potential of T-OFDM system in UWA channel, a more efficient PAPR reduction technique need to be utilized.

6.4.2 T-OFDM Systems with Clipping

The clipping approach is the simplest PAPR reduction scheme, which limits the maximum of transmit signal to a pre-specified level. However, the following drawbacks limit its implementation only to specific applications [79] [81]:

● Clipping causes in-band signal distortion, resulting in BER performance degradation.

● Clipping causes out-of-band radiation, which imposes out-of-band interference. Although the out-of-band signals caused by clipping can be reduced by filtering, it may affect high-frequency components of in-band signal (aliasing) when the clipping is performed with the Nyquist sampling rate in the discrete-time domain. However, if clipping is performed for the sufficiently-oversampled OFDM signals (e.g., $L \geq 4$) in the discrete-time domain before a low-pass filter (LPF) and the signal passes through a band-pass filter (BPF), the BER performance will be less degraded.

- Filtering the clipped signal can reduce out-of-band radiation at the cost of peak regrowth. The signal after filtering operation may exceed the clipping level specified for the clipping operation.

For a set of transmitted T-OFDM symbol, after defining the clipping level A, the clipping ratio (CR) can then be determined as

$$CR = \frac{A}{\sigma} \tag{6.4.5}$$

Where σ denotes the RMS of signal. The clipped version of the transmitted T-OFDM symbol can then be re-written as

$$x^A = \begin{cases} x & if\ |x| \le A \\ \dfrac{x}{|x|} \cdot A & otherwise \end{cases} \tag{6.4.6}$$

Because the Walsh-Hadamard transform reduces the occurrence of high peaks comparing to the original OFDM system [42], the BER penalty introduced through clipping could potentially be alleviated in the proposed T-OFDM system, making clipping a potential candidate for implementations in the proposed T-OFDM system. This theory is validated in the test section. Next, based on the structure of the T-OFDM system, the commonly used SLM and PTS PAPR reduction techniques are evaluated.

6.4.3 T-OFDM-SLM system

The conventional SLM scheme used in OFDM systems can be constructed by creating U copies of the frequency domain symbol $\mathbf{X}$ as

$$\mathbf{d}^{(\mathbf{u})} = \mathbf{X} \tag{6.4.7}$$

Where $u \in \{0,1,\dots,U-1\}$.

Each branch is multiplied by an N distinct points phase rotation vector $\boldsymbol{s}^{(u)} = \left[s_0^{(u)}, s_1^{(u)}, \dots, s_{N-1}^{(u)}\right]$ and the multiplication process can be expressed as

$$\mathbf{v}^{(\mathbf{u})} = \boldsymbol{s}^{(u)} \cdot \mathbf{d} \tag{6.4.8}$$

Where {.} denotes the element-by-element multiplication process. The result of multiplication $\mathbf{v}^{(\mathbf{u})}$ is up-sampled by a factor $L=4$, and applied to LN-points IFFT to generate discrete-times
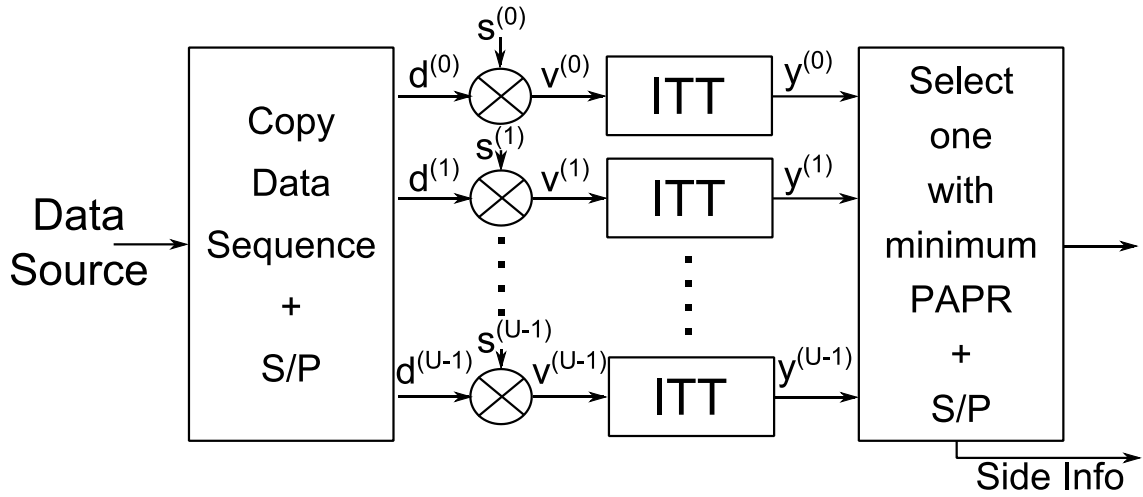
Figure 6.2. Block diagram of OFDM-based T-SLM scheme.

samples and then the PAPR is computed. Finally, the branch with the lowest PAPR is selected for transmission. The information about this branch is transmitted as the side information, given that the transmitter and the receiver share a common knowledge of the vectors $\boldsymbol{s}^{(\mathbf{u})}$. This SLM technique can be directly applied to the WHT-OFDM system [104], with the additional WHT block before the IFFT calculation. Therefore, the transmitted signal can be represented as

$$y_{\mathbf{WHT}}^{(u)} = \mathbf{W}\mathbf{v}^{(u)} \tag{6.4.9}$$

The remaining operations are identical to those of the conventional OFDM-SLM system. Consequently, the T-transform can be applied to the OFDM-SLM system by replacing the WHT-IFFT processes with the inverse T-transform, as shown in Figure 6.2. The corresponding signal is thus

$$y_{\mathbf{T-transform}}^{(u)} = \widehat{\mathbf{T}}\mathbf{v}^{(u)} \tag{6.4.10}$$

Once again, in OFDM, oversampling can be achieved by padding the frequency domain signal with $0^{1\times(L-1)N}$. Similarly, and identical approach can be used with WHT-OFDM by padding the WHT output signal with zeroes.

6.4.3.1 Computational Complexity of SLM based OFDM systems

In SLM scheme, the computational complexity consists of three parts:

a) *U×NL*-points IFFTs operations at the transmitter side;

b) Multiplications of the phase factor

c) PAPR computation and comparison among candidate signals

The SLM for OFDM, WHT-OFDM and T-OFDM requires identical operations for the entire system, except that the complexities of IFFT, WHT, and T-transform are compared. Therefore, the computational complexity in a) compared to the other related transforms is mainly considered. Accordingly, the computational complexity of the conventional SLM scheme is calculated based on the complexity of $U \times NL$-points IFFTs. The complexity of the IFFT is calculated based on two criteria of design including full-butterfly IFFT design, and pruning IFFTs design: i.e. omitting multiplications or additions with zero [106].

1) Complexity Calculation Based on Full-Butterfly IFFT Design

Full-butterfly IFFT design requires a $NL/2 \log_2 NL$ and $NL \log_2 NL$ of complex multiplications and additions, respectively. Therefore, based on a full-butterfly IFFT design, the total computational complexity of considered schemes, in terms of real additions, the computational complexity can be calculated as:

$$R_{Total}^{Conv.SLM} = 11UNL \log_2(NL) \tag{6.4.11}$$

$$R_{Total}^{WHT-SLM} = R_{Total}^{Conv.SLM} + 2UN \log_2(N) \tag{6.4.12}$$

$$R_{Total}^{T-SLM} = 12U[NL \log_2(NL) - (2NL - 2)] \tag{6.4.13}$$

Where *U* is the number of partitioned sub-blocks.

2) Based on the pruning IFFTs design, the computational complexity of a) in a conventional SLM scheme depends on the sparseness of data, i.e. non-zero data at the transmitter side, and full IFFT at the receiver side. Thus, the pruning IFFTs of the SLM scheme requires $\frac{1}{2}UNL \log_2 N + UN(L - 1)$ and $UNL \log_2 N$ complex multiplications and additions, respectively. Hence, the total complexity of such scheme in terms of real additions, can be calculated as

$$R_{Total}^{Pruning-SLM} = 11UNL \log_2(N) + 18UN(L - 1) \tag{6.4.14}$$

Similarly, in the case of a pruning-WHT-SLM system with oversampling, the total computational complexity in terms of real additions can be expressed as

$$R_{Total}^{Pruning-WHT-SLM} = R_{Total}^{Pruning-SLM} + 2UN \log_2(N) \tag{6.4.15}$$

Conversely, by implementing the pruning technique, the complexity of conventional-T-SLM can be dropped by $N/4$ butterflies. Consequently, the number of total butterflies in the pruning-T-SLM will be $\frac{1}{2}[NL \log_2 NL - (2NL - 2)] - \frac{NL}{4}$. Thus, the total computational complexity of T-SLM in terms of real additions can be expressed as

$$R_{Total}^{Pruning-T-SLM} = 12U[NL \log_2(NL) - (2NL - 2)] - 6UNL \tag{6.4.16}$$

6.4.4 Conventional PTS system

The PTS scheme is based on partitioning the input data block $\mathbf{X}$, which consists of N symbols into U disjoint sets $\hat{\mathbf{q}}^{(u)}, u = 0,1, \dots, U - 1$. Then each set of $\hat{\mathbf{q}}$ is padded with zeroes on both sides to obtain

$$\hat{\mathbf{q}}^{(u)} = [0^{1 \times uN/U}, \{\mathbf{X}\}_{uN/U}^{(u+1)N/U-1}, 0^{1 \times [N-(u+1)N/U]} \tag{6.4.17}$$

Each sub-block of $\hat{\mathbf{q}}$ is fed to individual NL-points IFFT attempting to reach the time-domain samples $\mathbf{X}^{(u)}$ as

$$\mathbf{X}^{(u)} = \hat{\mathbf{F}}\hat{\mathbf{q}}^{(u)} \tag{6.4.18}$$

The n-th sample of $\mathbf{X}^{(u)}$ can be written as

$$x_n^{(u)} = \frac{1}{\sqrt{NL}} \sum_{k=0}^{NL-1} q_k^{(u)} e^{j2\pi kn/NL}, n = 0,1, \dots, NL - 1 \tag{6.4.19}$$

Subsequently, each partially transmitted sequence $\mathbf{X}^{(u)}$ is multiplied by individual weighting phase factor, $b^{(u)} \in \{\pm 1, \pm j\}$, $u \in \{0,1, \dots, U - 1\}$. Based on the weight, P of $b^{(u)}$, there are $B' = P^{U-1}$ alternative representations for the OFDM symbol.

Finally, the transmitted symbol is constructed by adding the optimized U sequences, thus

$$\hat{d}_n = \sum_{u=0}^{U-1} b^{(u)} x_n^{(u)} \tag{6.4.20}$$

This scheme can be directly applied to WHT-OFDM systems by preceding the IFFT with the WHT, where data partition can be achieved in two ways, pre or post-WHT.

The computational complexity of PTS scheme will be composed based on the complexity of three parts, a), b) and c), as mentioned in previous SLM computational evaluation section. As stated in [67], the complexity of b) and c) operations in terms of real additions can be expressed as

$$D' = NL(U(20B' - 18) + 7B') \tag{6.4.21}$$

The complexity of D' is identical in both full-butterfly and pruning IFFT design. Furthermore, the burden of IFFTs computational complexity in the PTS scheme will be computed next based on the IFFT design.

6.4.4.1 Computational Complexity of PTS based OFDM systems

Similar to SLM systems, the complexity of calculating IFFTs in conventional PTS and WHT-PTS (where data partition performs after WHT, i.e. one WHT is required) schemes require $11UNL \log_2(NL)$ and $11UNL \log_2(NL) + 2N \log_2(N)$ real additions, respectively. Thus, the total real operations in conventional PTS and WHT-PTS schemes can be computed as

$$R_{Total}^{Conv.PTS} = 11UNL \log_2(NL) + D' \tag{6.4.22}$$

$$R_{Total}^{WHT-PTS} = 11UNL \log_2(NL) + 2N \log_2(N) + D' \tag{6.4.23}$$

Where D' is defined in (6.4.14).

1) Complexity Calculation Based on Pruning IFFT Design

Non-zero data in the conventional-PTS scheme is lower than that in oversampled-SLM scheme because sparse data depends on the oversampling factor L and the number of disjoint partitions, U; whereas it depends on L in the case of a SLM scheme. Consequently, the required complex multiplications, C_M and additions, C_A, in the pruning IFFTs (at transmitter) of the conventional PTS and WHT-PTS schemes can be computed as

$$C_M^{\text{pruning}-\text{IFFT}} = \frac{1}{2}UNL \log_2(\frac{N}{U}) + N(UL - 1) \tag{6.4.24}$$

$$C_A^{\text{pruning}-\text{IFFT}} = UNL \log_2(\frac{N}{U}) \tag{6.4.25}$$

$$C_M^{\text{pruning}-\text{WHT}-\text{IFFT}} = C_M^{\text{pruning}-\text{IFFT}} \tag{6.4.26}$$

$$C_A^{\text{pruning}-\text{WHT}-\text{IFFT}} = C_A^{\text{pruning}-\text{IFFT}} + N \log_2(N) \tag{6.4.27}$$

Consequently, the total real additions in the conventional PTS and WHT-PTS (including pruning IFFTs, full-butterfly IWHT/WHT, PAPR calculation and phase optimization process) can be written as

$$R_{Total}^{\text{pruning}-\text{PTS}} = 11UNL \log_2\left(\frac{N}{U}\right) + 18UNL - 18N + D' \tag{6.4.28}$$

$$R_{Total}^{\text{pruning}-\text{WHT}-\text{PTS}} = R_{Total}^{\text{pruning}-\text{PTS}} + 2N \log_2(N) \tag{6.4.29}$$

6.4.5 The T-PTS Scheme

In the proposed T-PTS scheme, the WHT of the data symbol $\mathbf{X}$ is computed as

$$\mathbf{d} = \mathbf{WX} \tag{6.4.30}$$

Then, the U disjoint partitions of the data vector, $\mathbf{d}^{(u)}, u = 0, \dots, U-1$, and the remainder of the processes are evaluated in a similar way to those in a traditional PTS scheme. Alternatively, the same disjoint partitions $\mathbf{d}^{(u)}$ can be computed by copying U-times the data samples $\mathbf{X}$ as, $\mathbf{X}^{(u)} = \mathbf{X}, u = 0,1, \dots, U-1$, and each copy is multiplied with a new normalized symmetrical matrix, $\mathbf{G}$. The U-versions of the normalized $\mathbf{G}$ matrix are computed as

$$\mathbf{G}^{(u)} = \mathbf{P}^{(u)}\mathbf{W} \tag{6.4.31}$$

Where $\mathbf{P}^{(u)}$ are new matrices that have $\frac{N}{U}$ data samples, which are equivalent to the u-th part of WHT matrix, $\mathbf{W}$, and $\frac{(U-1)}{U}N$ of zeroes. Consequently, the elements of these matrices can be computed as

$$\mathbf{P}^{(u)} = \left[0^{(:,1:uN/U)}, \{W\}^{(:,uN/U:(u+1)N/U-1)}, 0^{(:,1:[N-(u+1)N/U])} \right] \tag{6.4.32}$$

Consequently, each individual normalized $\mathbf{G}^{(u)}$ matrix has U elements comprising of uniformly distributed ones and $N - U$ zeroes in each column and row. Thus, the U versions of $\mathbf{X}$ are multiplied with each individual $\mathbf{G}^{(u)}$ matrix as

$$\mathbf{q}^{(u)} = \mathbf{G}^{(u)} \mathbf{X}^{(u)} \tag{6.4.33}$$

Therefore, the same non-overlapped sub-blocks partitions of (6.4.23) will be obtained by feeding each individual sequence in (6.4.26) into the WHT, as followed by the other steps in the PTS scheme. The up-sampling of (6.4.26) can be performed by generating U copies of $\mathbf{q}$, then each divided by $\sqrt{L}$. Thus,

$$\hat{\mathbf{v}}^{(u)} = \hat{\mathbf{v}}^{(u)}/\sqrt{L} \tag{6.4.34}$$

Where $v^{(u)} = [q_0^{(u)}, q_1^{(u)}, ..., q_L^{(u)}]$, and $q_l^{(u)} = q^{(u)}, l = 0,1, ..., L-1$.
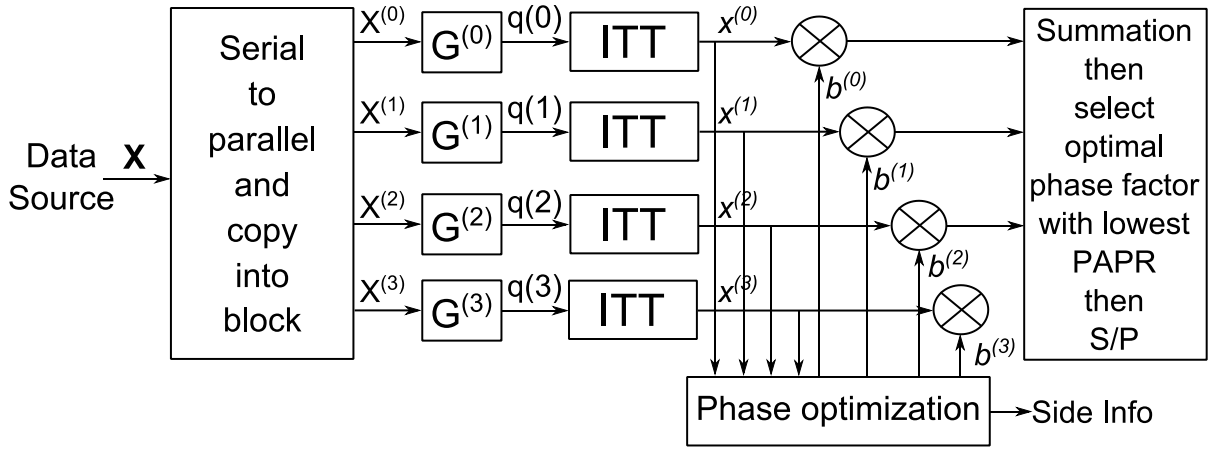
Figure 6.3: Block diagram of T-PTS scheme with $U = 4$.

The computational complexity of employing WHT with OFDM-PTS should be taken into account. Therefore, the WHT-IFFT can be simply replaced by the T-transform, as shown in Figure 6.3. The U disjoint sub-blocks of the new scheme can be attained by passing each individual sequence of (6.4.27) to the inverse T-transform as

$$x^{(u)} = \hat{\mathbf{T}}\hat{\mathbf{v}}^{(u)} \tag{6.4.35}$$

Then, the phase optimization and PAPR calculation steps are similar to those of a conventional PTS scheme.

6.4.5.1 Computational Complexity of T-PTS OFDM system

The computational complexity required of implementing the T-PTS scheme are evaluated based on the complexities of ITT, phase optimization process, PAPR calculations and $\mathbf{G}^{(u)}$ matrices. The complexity of phase optimization and PAPR calculations, which are identical in the T-PTS,

conventional PTS and WHT-PTS schemes can be reduced significantly as in [104]. Consequently, the computational complexity of ITT and $\mathbf{G}^{(u)}$ matrices are mainly considered in comparison with IFFTs and WHT-IFFTs. Implementing U-matrices of $\mathbf{G}$ requires $2U(U-1)N$ real additions. Thus, the total real additions in the T-PTS scheme based on the full-butterfly T-transform can be expressed as

$$R_{Total}^{\text{Full}-\text{T}-\text{PTS}} = 12U[NL\log_2(NL) - (2NL - 2)] + 2U(U - 1)N \qquad (6.4.36)$$

On the other hand, the total real additions in the oversampled T-PTS scheme based on pruning T-transform, i.e. by omitting the butterfly of the same data symbols, can be computed as

$$R_{Total}^{\text{Pruning}-\text{T}-\text{PTS}} = R_{Total}^{\text{Full}-\text{T}-\text{PTS}} - 6UNL \qquad (6.4.37)$$

6.5 Numerical Results

The performance of the above proposed PAPR reduction techniques are evaluated in this section. Due to the unique characteristics of UWA channels, the proposed PAPR techniques are first tested in a controlled environment (a water tank). The PAPR reduction technique yielded best BER performance is chosen and further tested in a real world environment. The results are presented next.

6.5.1 Water Tank Test Results

The proposed system is first tested in a water tank with approximate dimensions of 3m long, 2m wide and 2m deep. A typical impulse response of the channel is shown in Figure 6.4.
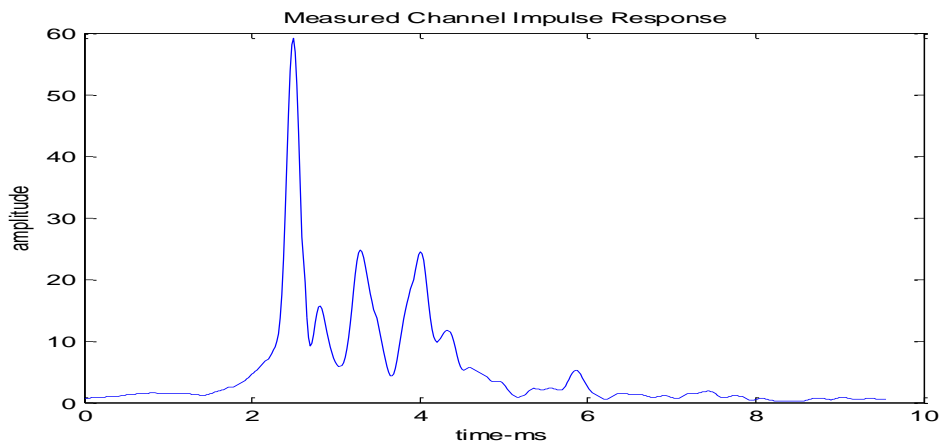
Figure 6.4 Typical measured channel impulse response of the water tank.

Some degree of channel variability is attained by stirring the tank water. As the conventional SLM technique can be directly implemented onto the proposed system, the performance variation of T-OFDM and conventional OFDM with this technique is mainly a projection of performance difference between T-OFDM and OFDM system. Therefore, only two data packets are generated with WHT-PTS and clipping implemented as PAPR reduction technique, respectively. First, the proposed T-OFDM system with PTS technique is tested against OFDM system implementing the same scheme. Packets are generated for both system with varying FFT size and partitioning number of N=1,2,4,8,16. The CCDF (complementary cumulative distribution function) of PAPR for both systems with varying FFT sizes are presented in Figure 6.5-6.7.

Figure 6.5: CCDF of 512 FFT OFDM and T-OFDM system with various number of partitioned blocks.
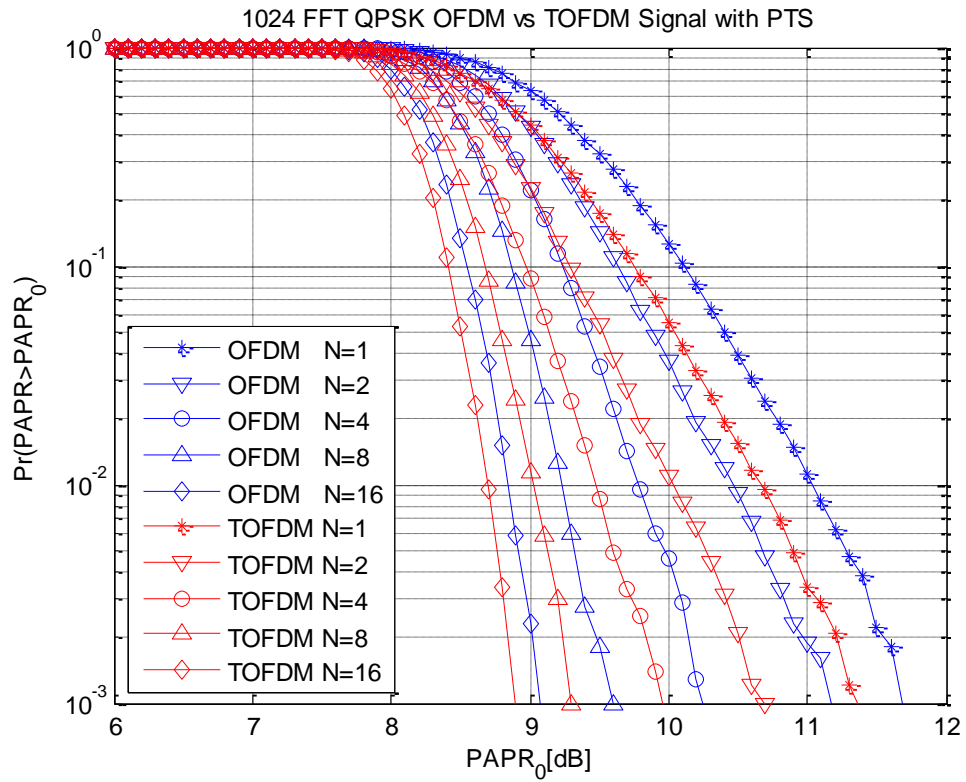
Figure 6.6/6.7: CCDF of 1024/2048 FFT OFDM and T-OFDM system with various number of partitioned blocks.

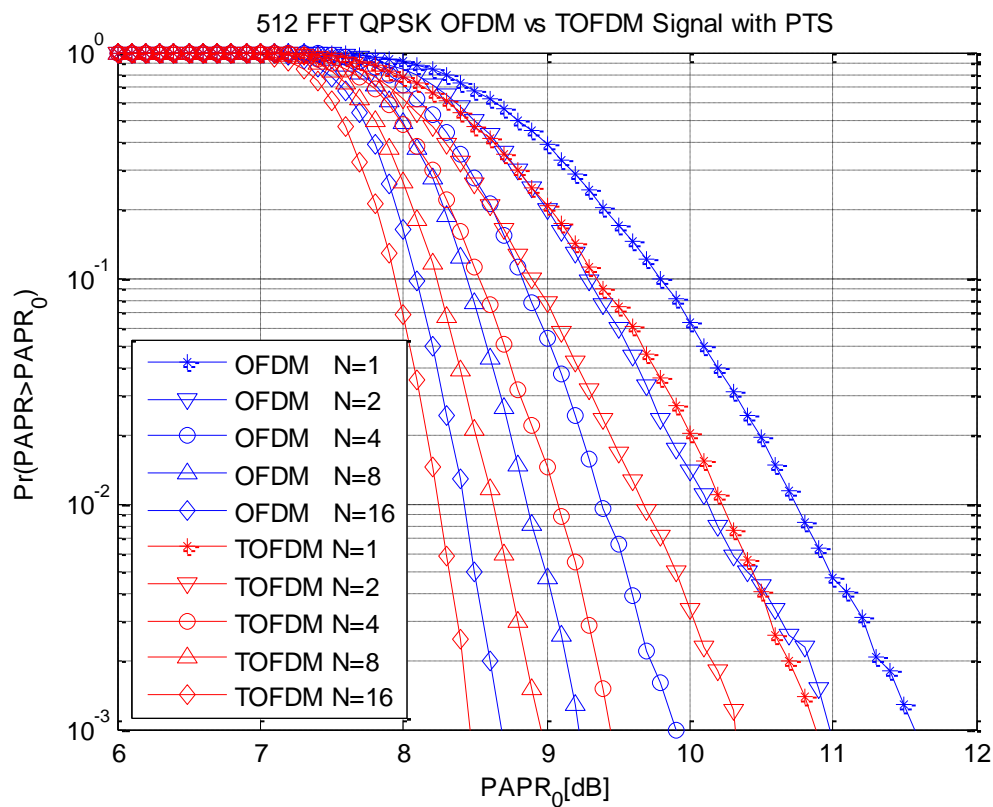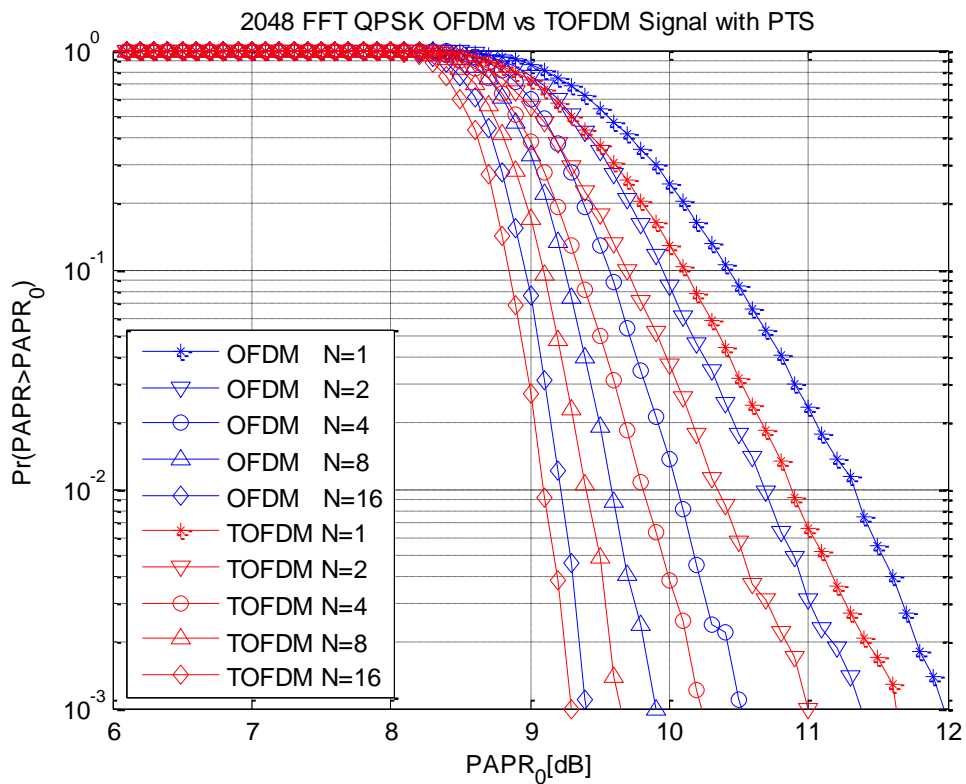As can be seen from Figure 6.5-6.7, the degree of PAPR reduction increases when increasing the number of partitions. Note that for every partition number, the proposed T-OFDM system revealed lower PAPR when comparing to corresponding OFDM systems. However, the computational complexity increases accordingly. In order to determine the optimal partitioning number, the BER performance of OFDM and T-OFDM system is tested next. The BER is calculated by adding AWGN onto the received signal with measured SNR. As the experiment is conducted in a controlled environment, therefore the performance difference between systems with different FFT sizes are minimal. Figure 6.8 is an example of the measured BER for both systems with a FFT size of 512. As delineated in Figure 6.8, although the proposed T-OFDM system outperforms the corresponding OFDM system for every partitioned sub-block number, this technique is still ruled out for our application as the amount of BER performance improvement gained through the process cannot outrun the reduced amount of PAPR, not to mention the added computational burden. Systems utilizing the clipping technique is tested next.
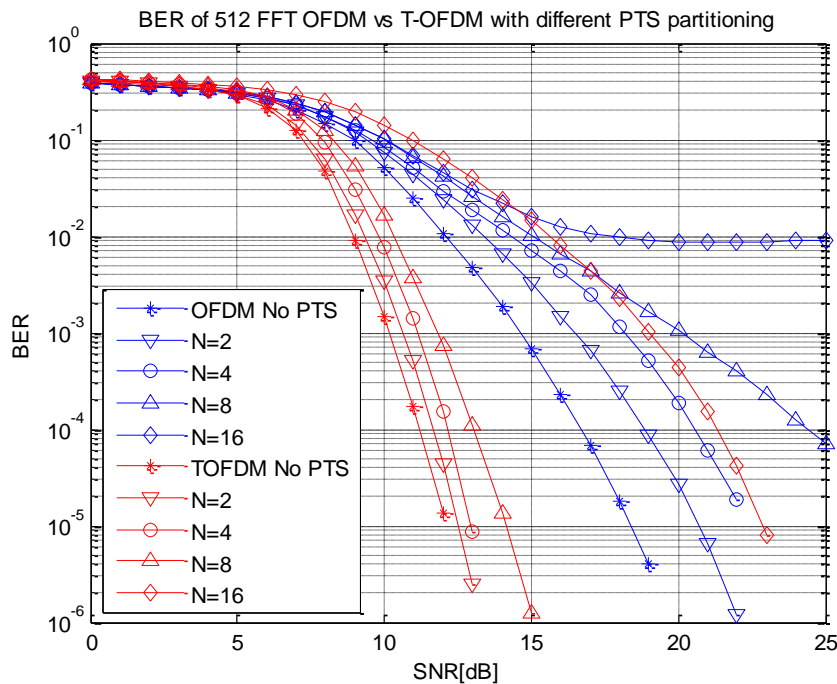
Figure 6.8: BER performance of 512 FFT OFDM and T-OFDM system with various partitioned blocks.

Figure 6.9-6.11 demonstrate the PAPR reduction potential of systems implementing clipping with different clipping ratios.

Although T-OFDM systems revealed lower PAPR than OFDM systems without applying any clipping (due to WHT), both systems experience the same amount of PAPR after clipping is implemented.
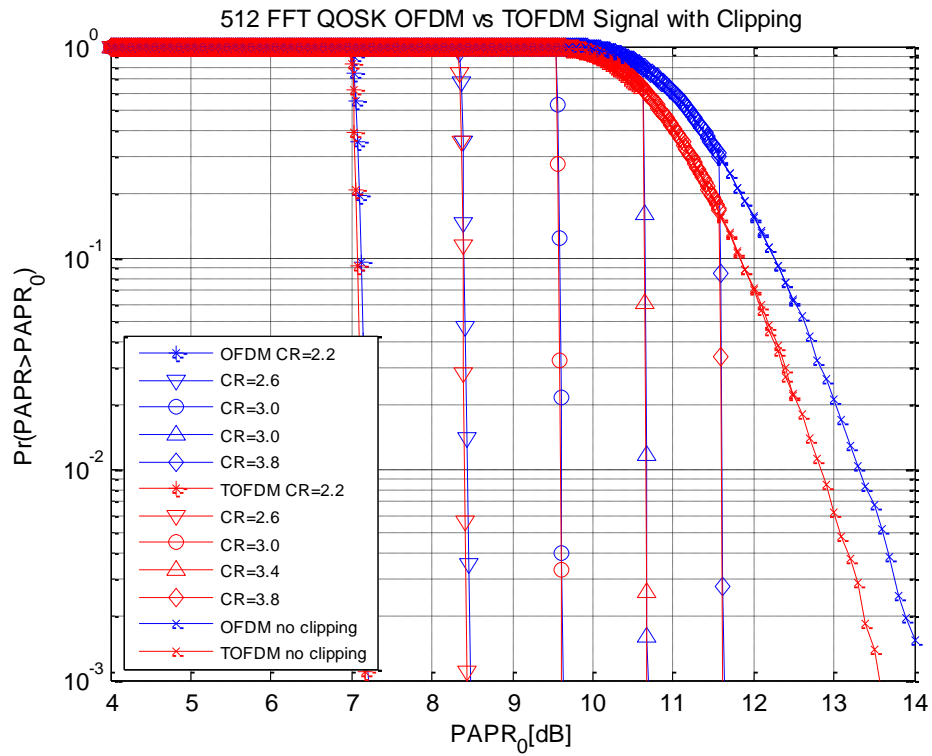
Figure 6.9: PAPR performance of 512 OFDM/TOFDM system with clipping.
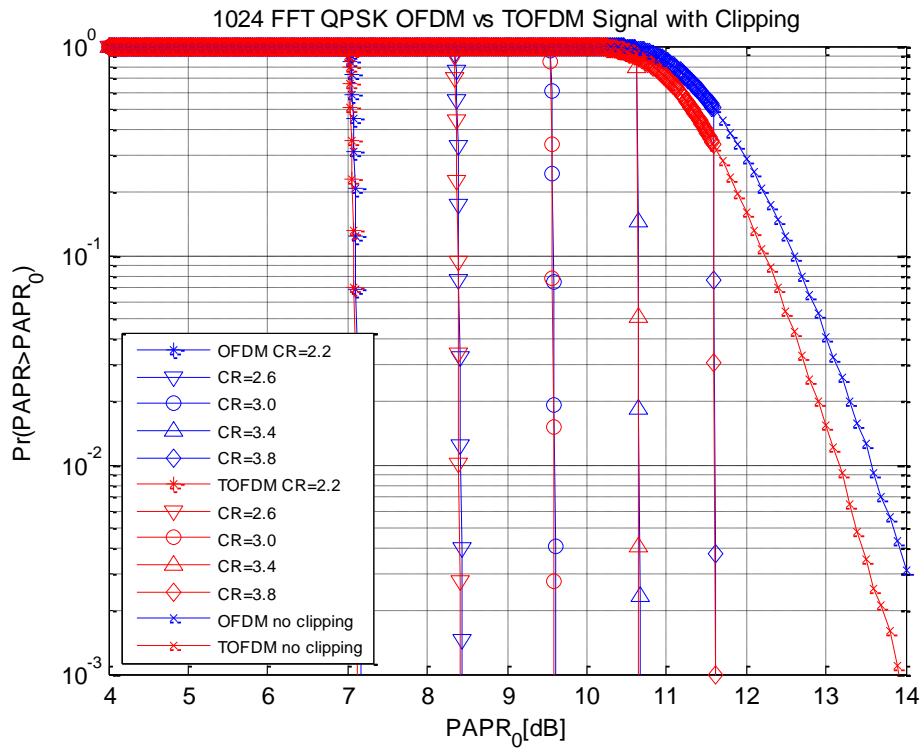
Figure 6.10: PAPR performance of 1024 OFDM/TOFDM system with clipping.
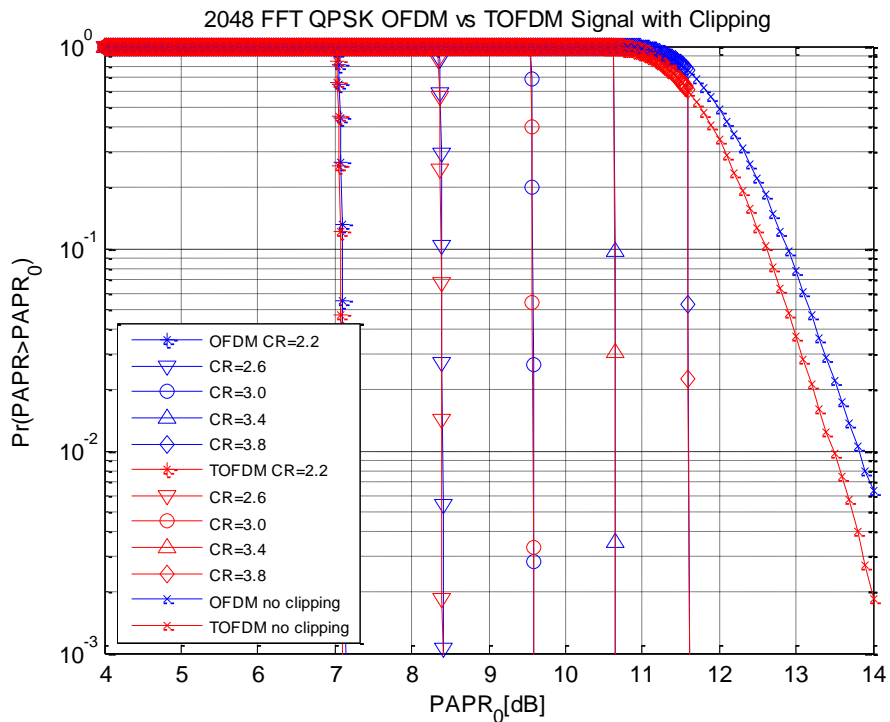
Figure 6.11: PAPR performance of 2048 OFDM/TOFDM system with clipping.

The biggest advantage of utilizing the clipping method when comparing it to methods such as PTS or SLM is that it provides very effective PAPR reduction with the smallest amount of added computational complexity. Conversely, the penalty on the BER performance is

proportional to the clipping ratio applied. As stated in the previous sections, the hypothesis is that T-OFDM will perform better with clipping techniques applied as the Walsh-Hadamard transform lowers the probability of high amplitude peaks from occurring. The BER performance of both systems with clipping technique implemented in show next. By following the same procedure, the BER plots for both systems with varying FFT sizes and clipping ratios are demonstrated in Figure 6.12-6.14. As can be seen from the BER plots, the BER performance for both systems suffers from the amount of clipping applied. On the other hand, the proposed T-OFDM system drastically outperforms OFDM systems with the same clipping ratio across all three FFT sizes. It is also shown that with mild clipping, both systems achieved a minimum PAPR reduction of 8 dB with little to none BER degradation.
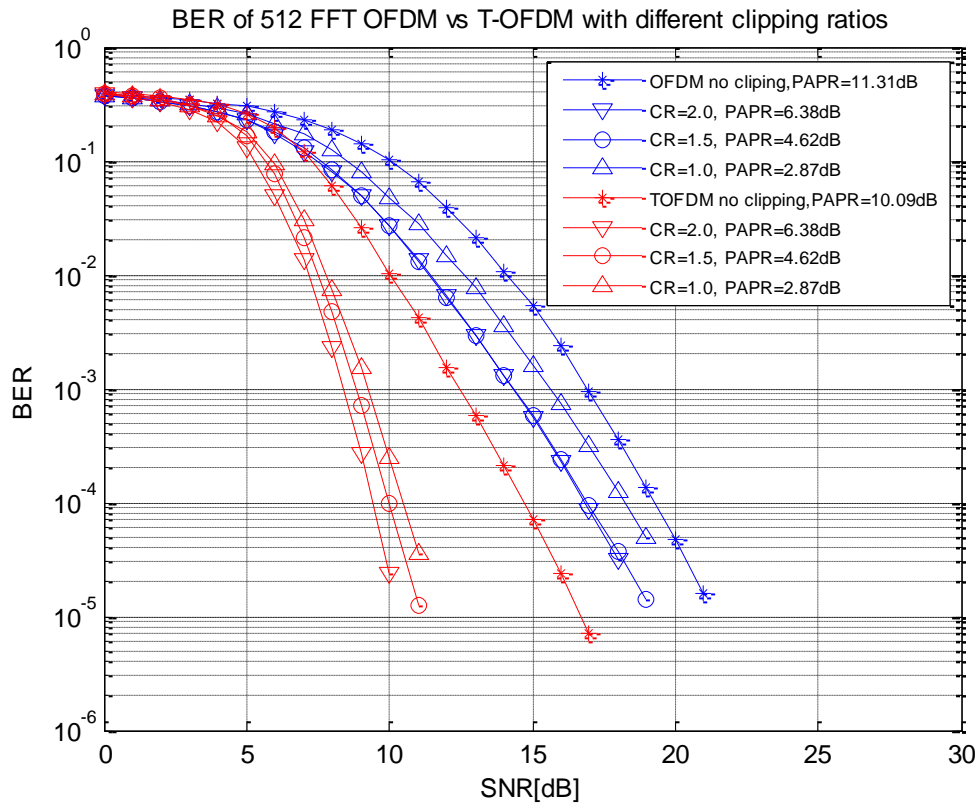
Figure 6.12: Water tank BER of 512 FFT OFDM/TOFDM system with clipping.
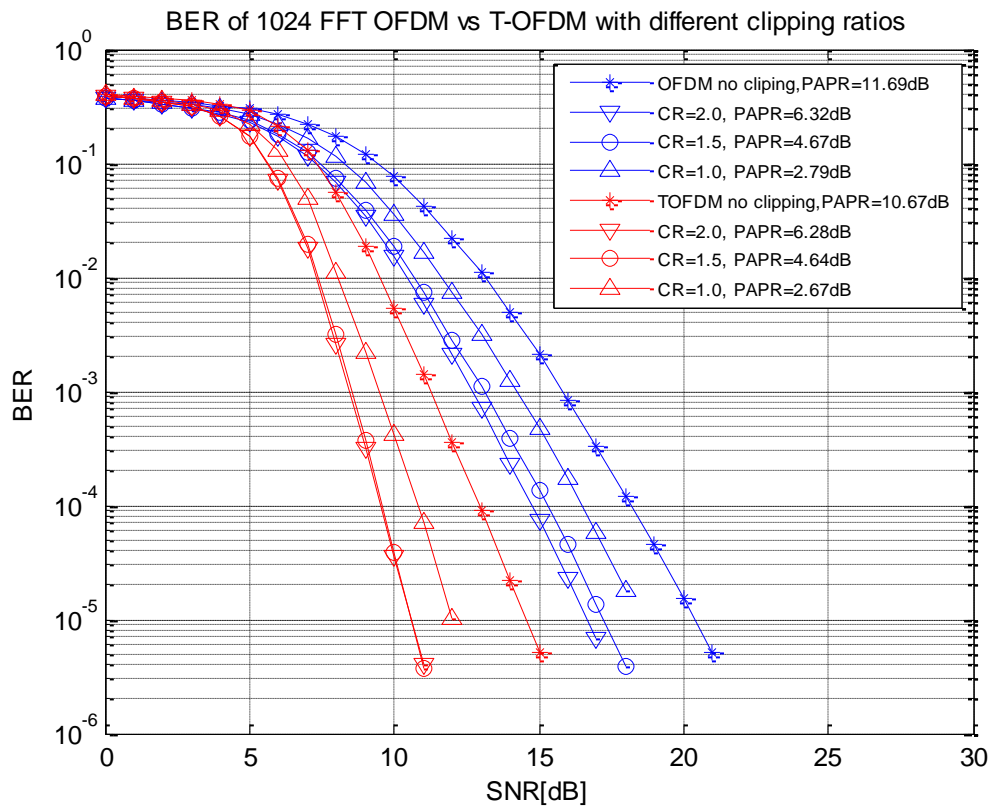
Figure 6.13: Water tank BER of 1024 FFT OFDM/TOFDM system with clipping.
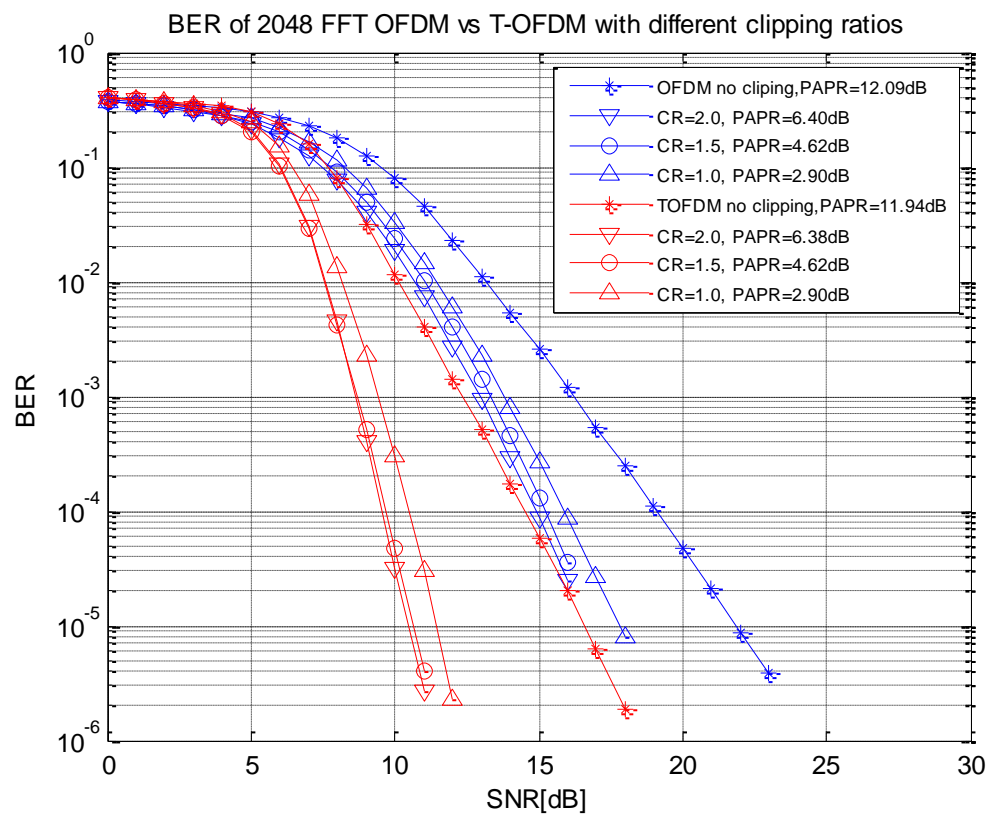
Figure 6.14: Water tank BER of 2048 FFT OFDM/TOFDM system with clipping.

On the other hand, for all three FFT sizes, both T-OFDM and OFDM systems without clipping revealed the worst BER performance. This is due to the fact that, for a constant amount of transmitted power, clipping process offered a higher mean power at the receiver side. Conversely, the BER performance between systems with mild clipping and moderate clipping (CR=2 and CR=1.5) is very close although even the mildest clipping provided huge PAPR reduction. Conversely, systems with hardest clipping (CR=1.0) yielded lowest PAPR whilst the BER performance degradation became severe and the performance gap between no clipping is closing. Overall, this does match the theory stated in the prior section where T-OFDM systems can better tolerate the distortions introduced from the clipping process. The proposed system is then tested in a short range multipath channel with results presented next.

6.5.2 River Test Results

The trial was conducted on February 7, 2016 at Royal Quay Marina, River Tyne, Newcastle upon Tyne, UK. The transmitter and receiver are set 3m below the water surface across a busy shipping canal with a water depth of roughly 12m. The direct distance between transmitter and receiver is approximately 100m.

Figure 6.15 shows the experiment setup and trial location.
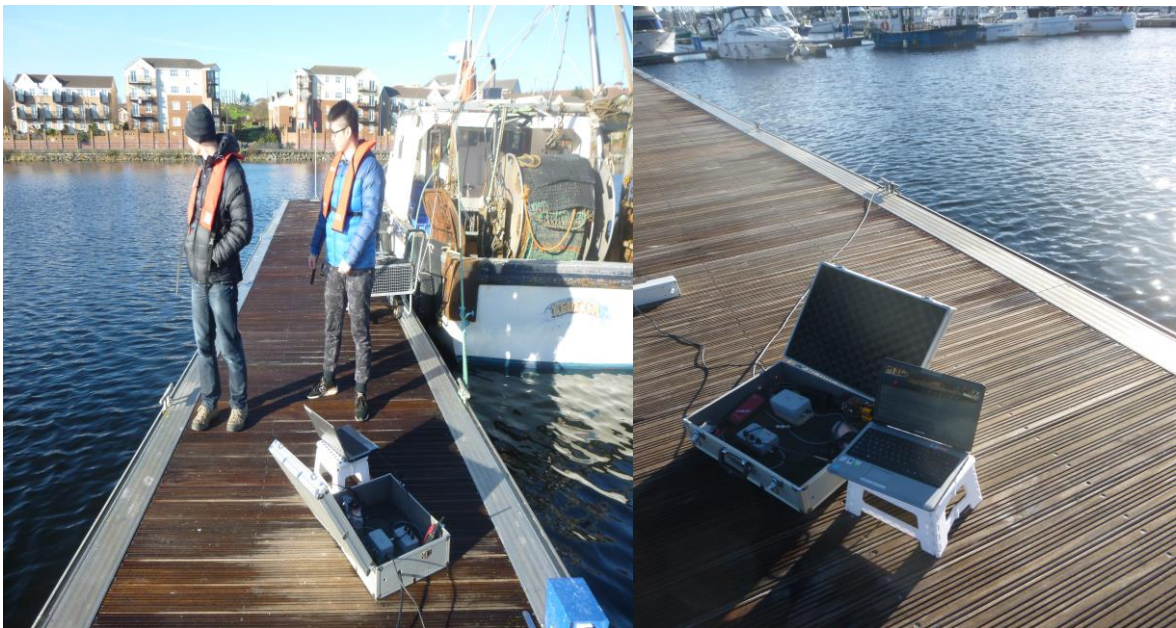
Figure 6.15: River trial location and an overall view of the receiver kit (with hydrophone in the water).

a) Packet Structure: The transmitted packets are produced as shown in Figure 6.16

| silent period | Packet N = 512 | silent period | Packet N = 1024 | silent period | Packet N = 2048 | silent period |

| Up-chirp | T-OFDM | Down-chirp | OFDM | Up-chirp |
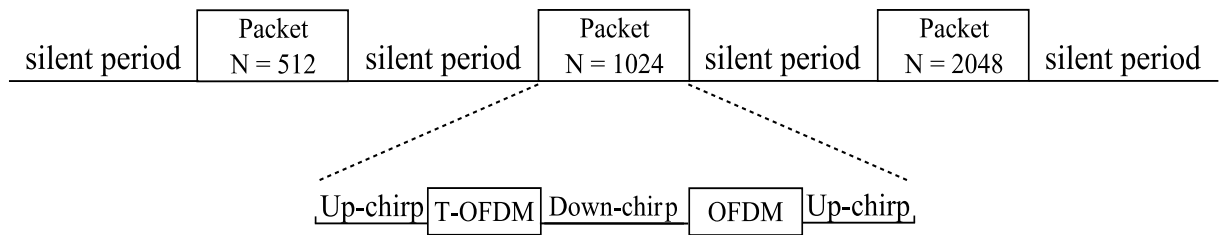
Figure 6.16: Data burst structure

Three clipping ratios are chosen and assigned to the first three sets which corresponds to scenarios where mild clipping, moderate clipping and heavy clipping are applied. The last data set represents systems without any clipping implemented.

b) Channel Overview: The water channel where the proposed systems were tested is in a busy shipping canal with the presence of severe amount of man-made noise such as engine noise introduced from bypassing ferries. Additionally, the relatively smooth bottom of the river bed and the narrow opening of the Marina exit resulted in a multipath heavy channel with moderate channel delay spreads. On the other hand, the semi-closed structure of the marina provided a steady channel with little channel variations. The channel condition is verified in Figure 6.17 and 6.18 which are a typical channel impulse response captured during the recoding and the channel variation for all received packets, respectively.

c) Test Results: For each of the transmitted packet, four minutes of data are recorded where the corresponding block error rate for each packet is listed in Table 6.1. The block error rate (BLER) is chosen as performance criterion as it provides the most comprehensive view on the overall system performance across every received packet. The transmitted power is adjusted correspondingly for each packet with different PAPR in order to achieve the maximum possible performance. Overall, systems with a FFT size of 1024 performed the best which matched the channel characteristics (moderate delay spread and channel complexity). Note that for T-OFDM system with FFT size of 1024 and clipping ratio of 1.5, the BLER was 0.012, this is because during the recoding of that specific packet a ferry shipped past the canal causing irregularly high noise floor. For both OFDM and the proposed T-OFDM systems, packets with a clipping ratio of CR=2 revealed the best performance for all three FFT sizes where all packets are received and decoded without any error. It also shown that at a busy channel with severe added

man-made noise, the inherent high PAPR issue associated with OFDM/T-OFDM systems become performance threshold as systems without clipping technique implemented performed the worst.

In order to further differentiate the performance difference between the proposed system and OFDM systems with varying FFT sizes and different applied clipping ratio, BER performance are generated by adding white Gaussian noise (AWGN) onto received packets based on the measured power level. Results are displayed through Figure 6.18- Figure 6.20. Note that during the transmission of four packets with different clipping ratios, the power amplifier is adjusted accordingly in order to offer the highest possible transmitting power without the signal being distorted. Hence systems with low peak power (i.e. low PAPR ratio) have the advantage of higher transmitting power. As can be seen from Figure 6.19-6.21, the proposed T-OFDM systems outperform OFDM system for all three FFT sizes with clipping applied as a PAPR reduction method. It is also proven that an effective PAPR reduction technique is crucial for the viability of OFDM based systems in highly noisy channels as even systems with mildest clipping drastically outperforms the original systems. Conversely, the BER performance gained from reduced PAPR decreased vastly with increased degree of clipping. The BER performance improvement with PAPR reduction is listed in Table 6.2.
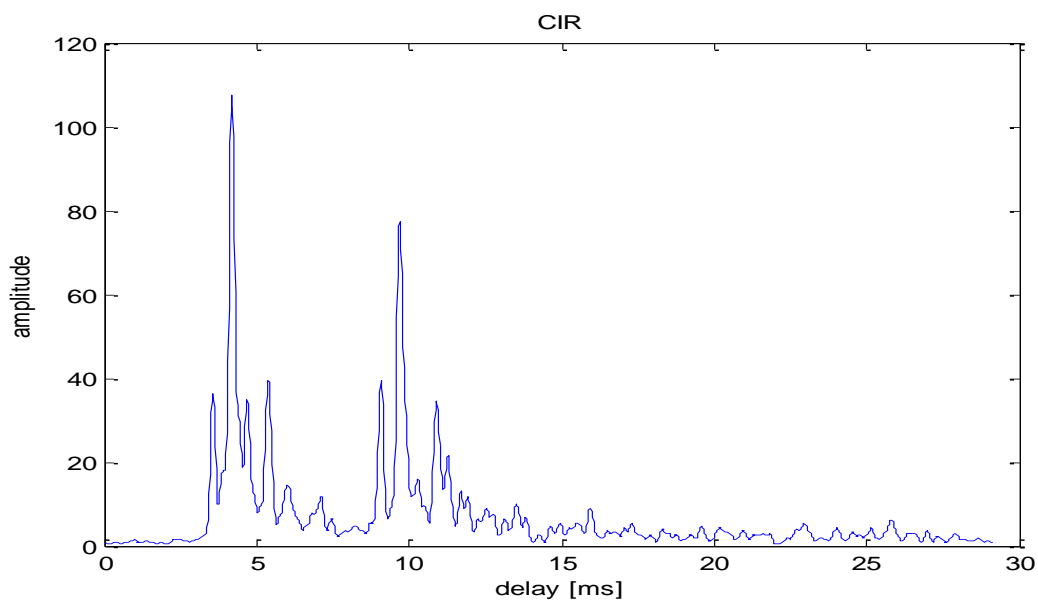
Figure 6.17: Typical measured channel impulse response at trial location.
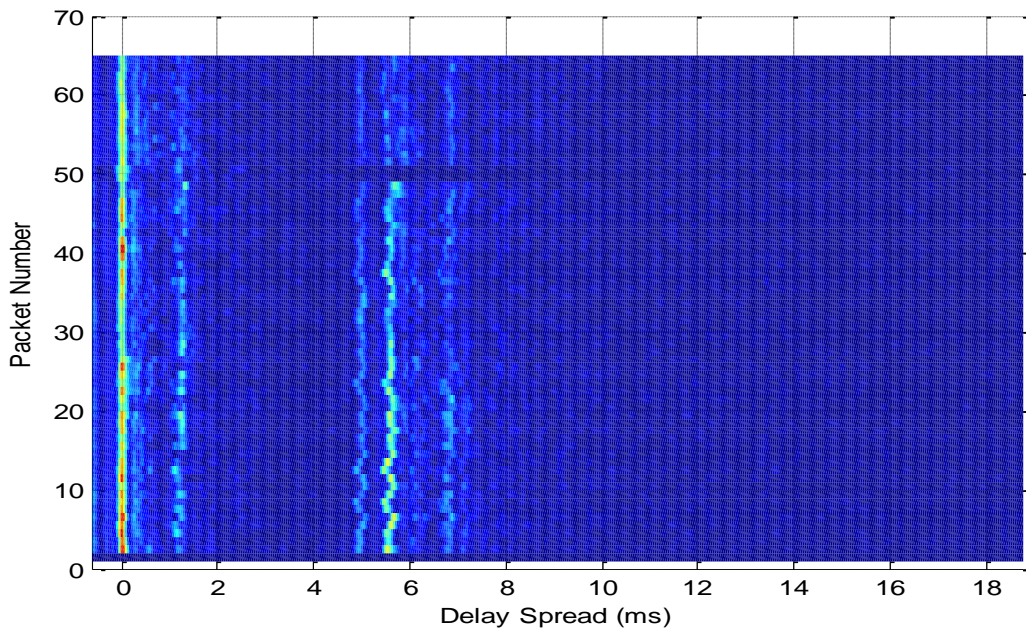
Figure 6.18: Channel variation at recorded location.

Note that difference of SNR is measured at a BER level of 10^{-3}. Although the proposed T-OFDM system significantly outperformed OFDM system with the same clipping ratio in terms of BER performance, the amount of gained BER through clipping varies with FFT sizes.
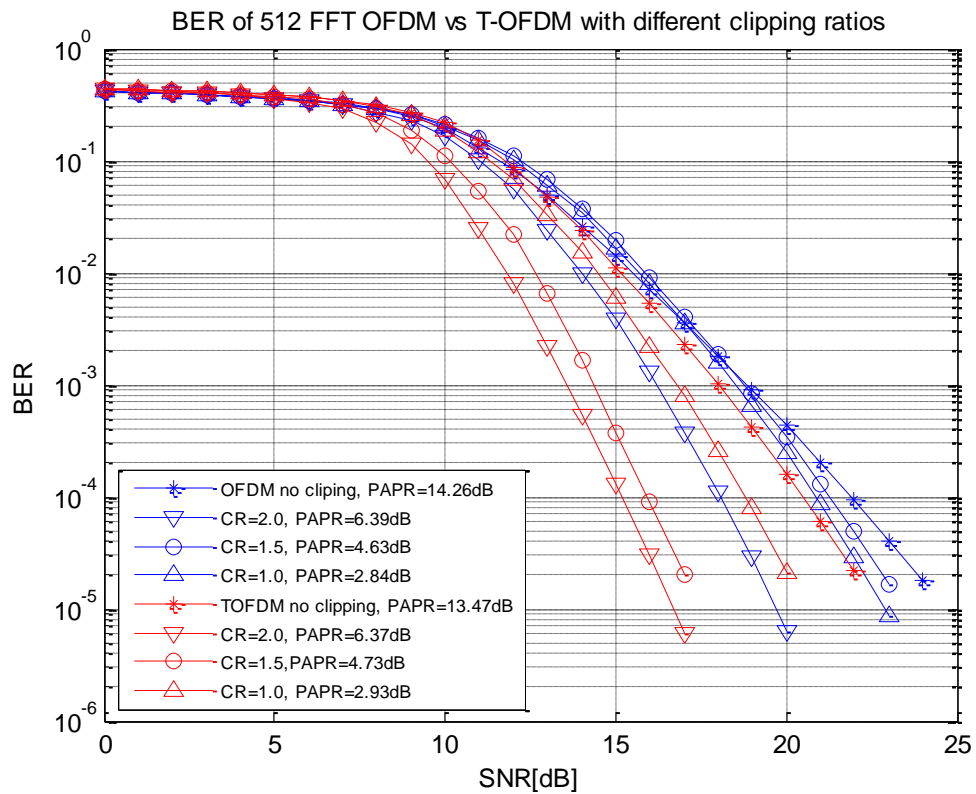
Figure 6.19: BER performance of 512 OFDM/TOFDM with clipping.
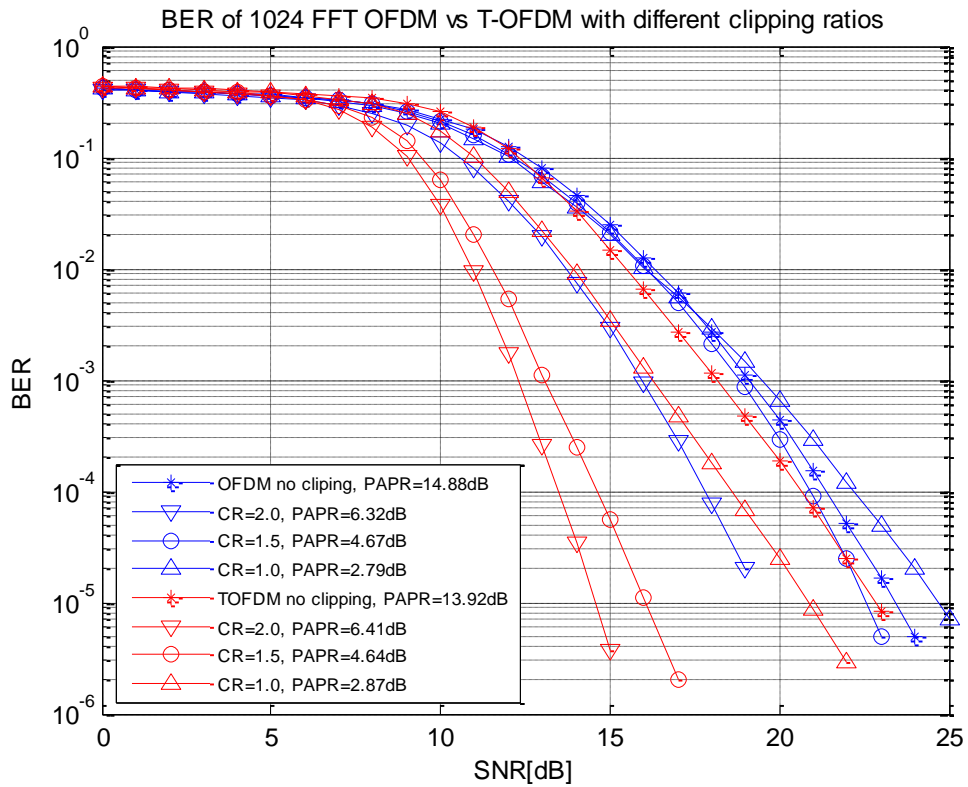
Figure 6.20: BER performance of 1024 OFDM/TOFDM with clipping.
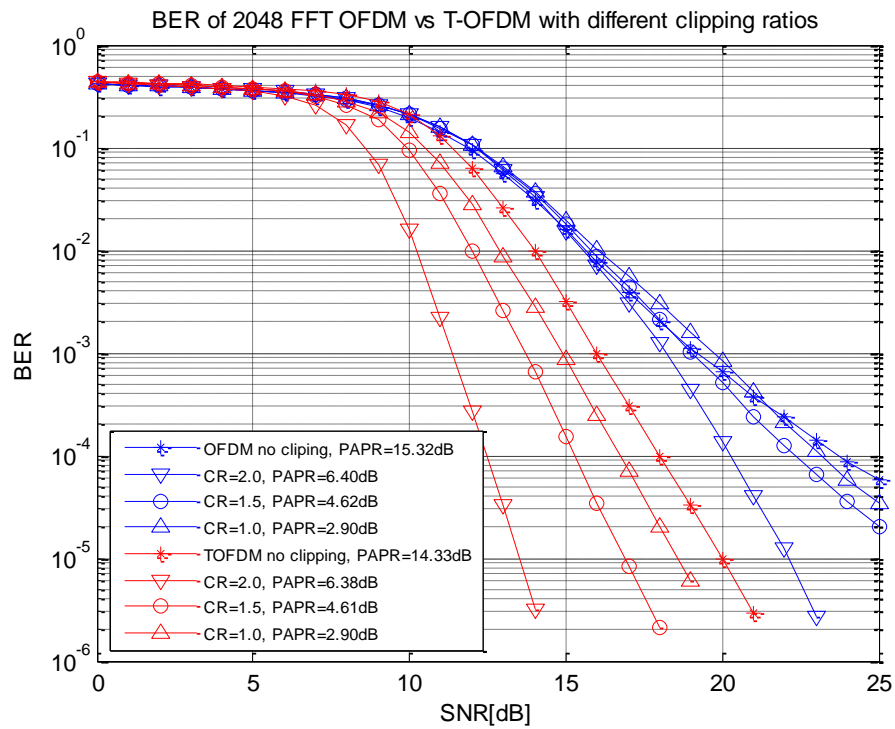
Figure 6.21: BER performance of 2048 OFDM/TOFDM with clipping.

For the optimal clipping ratio of CR=2, the amount of gained BER through clipping is comparable between T-OFDM and OFDM with FFT size of 512 and 1024. However, the BER performance of T-OFDM improved drastically through clipping with FFT size of 2048. This is due to the fact that systems with longer FFT can better utilize the channel diversity which is further emphasized by the proposed T-OFDM system in this case.

Table 6.1 BLER Performance for systems with varying clipping ratios.

FFT	SCHEME	NO CLIPPING	CR=2	CR=1.5	CR=1
512	T-OFDM	0.017	0.000	0.000	0.000
	OFDM	0.033	0.000	0.013	0.016
1024	T-OFDM	0.000	0.000	0.012	0.000
	OFDM	0.037	0.000	0.000	0.015
2048	T-OFDM	0.021	0.000	0.011	0.000
	OFDM	0.163	0.000	0.021	0.160

Table 6.2 Effectiveness of Different Clipping Ratios

FFT	512				1024				2048			
Schemes	OFDM		TOFDM		OFDM		TOFDM		OFDM		TOFDM	
PAPR	14.26dB		13.47dB		14.88dB		13.92dB		15.32dB		14.33dB	
	ΔPAPR	ΔSNR	ΔPAPR	ΔSNR	ΔPAPR	ΔSNR	ΔPAPR	ΔSNR	ΔPAPR	ΔSNR	ΔPAPR	ΔSNR
CR=2	7.87	2.68	7.10	4.26	8.56	3.55	7.51	5.88	8.92	1.57	7.95	4.63
CR=1.5	9.63	0.35	8.74	3.69	10.21	0.64	9.28	5.15	10.70	0.76	9.72	2.26
CR=1	11.42	0.11	10.54	1.24	12.09	0.37	11.05	1.96	12.42	0.61	11.43	1.13

Figure 6.20: BER performance of 2048 OFDM/TOFDM with clipping.

While on the other hand, the penalty of having a longer symbol in terms of channel estimation performance is less pronounced in the tested channel where little channel variation is experienced.

6.6 Chapter Summary

In this chapter, we focused on the PAPR of T-OFDM system with the addition of evaluation of different PAPR reduction schemes and their performance in the proposed T-OFDM system in UWA channels. From both water tank test and real world environment tests, the proposed T-OFDM system achieved better performance against OFDM system with varying FFT sizes without sacrificing any data throughput. When utilizing clipping technique as PAPR reduction method, both systems revealed an improvement on BER performance. However, the actual amount of BER improvement acquired is significantly higher in the proposed T-OFDM system comparing to OFDM systems. Results indicate that clipping technique works more efficiently in the proposed system as T-OFDM has higher tolerance against signal distortion introduced from the clipping process, making clipping the ideal PAPR reduction method for the proposed system for use in UWA channels.

CHAPTER 7

Conclusion

7.1 Concluding Remarks

This chapter concludes the key results and conclusions from the previous chapters. A comprehensive description is given for each chapter, focusing on the main contributions towards the development of a high data rate, low cost multicarrier underwater acoustic communication system.

In this thesis, the initial investigation was focused on the channel characteristics of UWA channels. An evaluation of the channel response revealed the noticeable amount of delay spread and the separation between different multipath arrivals introduced from the low range to depth ratio of the UWA channel geometry. On the other hand, the relative motion between the transmitter and receiver together with the low maximum velocity of acoustic waves underwater is found to cause complications in the estimation and compensation of the incurred Doppler shift. Eventually, the highly noisy nature inherent to the UWA channel was shown to cause intermittent fluctuations in the received signal SNR. Various previous systems ranging from coherent to non-coherent systems with the addition of multicarrier systems were analyzed. Due to the ability of suppressing the detrimental multipath spread and the potential of high data rate transmission, OFDM represented multicarrier systems were chosen as the interesting candidate for UWA communication, although with noticeable limitations for applications underwater. As a result, the motivation behind this research was to utilize the prominent features of T-transform

which was introduced in [51] to combine the Walsh-Hadamard transform (WHT) and the discrete Fourier transform (DFT) into a single fast orthonormal unitary transform, with the OFDM systems instead of IFFT/FFT to construct the proposed T-OFDM system. Chapter 3 presented the comprehensive analysis of OFDM and T-OFDM systems started from basic principles of multicarrier transmission to the fast transforms closely associated with both systems. Moreover, the length of the T-transform was shown to be the same as the number of subcarriers, thus no bandwidth expansion (i.e. no data rate losses) was experienced when utilizing the T-transform as the transmission techniques.

Based on the understanding of the specific channel conditions and the characteristics of the proposed system, Chapter 4 explored a selection of suitable receiver structures. The lower computational complexity requirement of T-OFDM has been addressed by comparing its complexity along with three proposed receiver types with conventional systems. Additionally, the theoretical BER formula for the T-OFDM system have been derived over AWGN, flat fading and quasi-static frequency selective fading channel models with ZF and MMSE equalizers. The BER performance was then obtained via transmission over a water tank. Various data rates were achieved through puncturing the transmitted sequence. Results indicates that with enough added redundancy, OFDM marginally outperformed T-OFDM system. However the proposed system revealed better spectral efficiency as it offered superior BER performance when increasing the data rate (less redundancy).

On the other hand, due to the spreading property of the T-transform, T-OFDM suffers more from inaccurate channel coefficients in deep fades as each channel coefficient affects all of the transmitted symbols. As a result, deep fading coefficients will have detrimental effects on the BER performance of the received signal as it creates an extra 'noise floor'. Accordingly, different equalization techniques were analyzed in Chapter 5. Although MMSE channel equalizer provides a good level of noise suppression, it is not practical for use in fast varying UWA channels as the channel response and noise variance required in computing the equalizer sequence cannot be updated fast enough in order to track the channel variability. As a result, a modified ZF channel estimator which eliminates the noise enhancement by identifying and replacing the null channel taps was introduced. The performance of systems implementing ZF equalizer and modified ZF equalizer was first verified in a water tank result. The proposed T-

OFDM system was tested alongside with conventional OFDM system and DCT precoded OFDM system. For FFT sizes of 512, 1024 and 2048, all three systems implemented with the modified ZF channel estimator revealed at least 10dB of SNR improvement at a BER level of 10^{-3}. On the other hand, both DCT-OFDM and T-OFDM systems outperformed conventional OFDM system by at least 5dB at a BER level of 10^{-3}. The proposed systems were then tested in a sea trial. Block error rate (BLER) performance shown that the proposed T-OFDM system continuously outperformed both DCT-OFDM and OFDM system. It was also revealed that for channels with longer delay spreads (500m), systems with longer FFT performed better as it increased the system robustness against delay spread. Although the 2000m channel demonstrated that systems with a FFT size of 512 were superior as better utilization of channel frequency diversity was achieved. Those results verified that T-OFDM outperforms OFDM in severe multipath channels due to the spectral diversity introduced by the WH transform without affecting any system throughput.

Furthermore, as the WHT scrambles the input sequence before IFFT operation, the side lobe amplitude is lowered than data fed directly through IFFT. For varying FFT sizes, this reduced autocorrelation property reduces the PAPR within a range of 0.75dB ~ 1.2dB. However, this degree of reduction become inconspicuous in a realistic UWA channel due to the highly dynamic nature of the channel itself. Therefore, Chapter 6 presented an evaluation of various PAPR reduction techniques such as clipping technique, PTS and SLM schemes. Moreover, the sparsity and diagonal structure of T-transform have been utilized with conventional SLM and PTS schemes to introduce T-SLM and T-PTS schemes. Computational complexity analysis shown that both T-SLM and T-PTS schemes revealed lower computational load comparing to conventional schemes. In order to choose the optimal PAPR reduction technique for use in UWA channels, numerical results for systems implementing different PAPR reduction techniques were given via water tank test and river test. CCDF plots for system with various FFT sizes were first given demonstrating the potential amount of PAPR reduction. SLM and PTS schemes were ruled out for use in UWA channels after water tank test as the BER performance suggested that the amount of reduced PAPR could not out run the BER degradation, not to mention the added system complexity. Conversely, the clipping technique was verified as an effective PAPR reduction technique based on the BER performance. With mild clipping, both systems achieved

a minimum PAPR reduction of 8dB with little to none BER degradation. On the other hand, for all three FFT sizes, both T-OFDM and OFDM systems without clipping revealed the worst BER performance. This is due to the fact that, for a constant amount of transmitted power, clipping process offered a higher mean power at the receiver side. Conversely, the BER performance between systems with mild clipping and moderate clipping (CR=2 and CR=1.5) is very close although even the mildest clipping provided huge PAPR reduction. Conversely, systems with hardest clipping (CR=1.0) yielded lowest PAPR whilst the BER performance degradation became severe and the performance gap between no clipping is closing, indicating that it is not implementable in any practical systems. Next, the proposed system was tested in a short range multipath channel placed in a busy shipping canal. The advantage of systems implementing a more effective PAPR reduction was projected in the transmitter side as the lower PAPR enabled a higher transmitting power as the transmitter power amplifier was less possible to saturate. BER performance suggested that the proposed T-OFDM system was superior to OFDM system for all tested FFT sizes. It was also proven that an effective PAPR reduction technique is crucial for the viability of OFDM based systems in highly noisy channels as even systems with mildest clipping drastically outperforms the original system. Conversely, the BER performance gained from reduced PAPR decreased vastly with increased degree of clipping. Although the proposed T-OFDM system significantly outperformed OFDM system with the same clipping ratio in terms of BER performance, the amount of gained BER through clipping varies with FFT sizes. For the optimal clipping ratio of CR=2, the gained BER through clipping was comparable between T-OFDM and OFDM with FFT sizes of 512 and 1024. However, the BER performance of T-OFDM improved drastically through clipping with FFT size of 2048. This was due to the fact that systems with longer FFT can better utilize the channel diversity which was further emphasized by the proposed T-OFDM system in this case. While on the other hand, the penalty of having a longer symbol in terms of channel estimation performance was less pronounced in the tested channel where little channel variation was experienced. Overall, the superior BER results suggested that large BER performance gains (also higher tolerance in amplifier non-linearity) can be achieved in T-OFDM systems using a simple clipping PAPR reduction technique in a realistic multipath fading channel.

This thesis has presented a set of comprehensive recommendations for the design of a high data rate, robust and low complexity multicarrier communication system for use in UWA channels. Based on rigorous testing and a thorough evaluation of the typical operating conditions, a suitable T-OFDM based system has been constructed, enabling the better exploitation of channel diversity without any loss in the system throughput.

7.2 Future Work

Based on the outcomes and finding of the presented research, severe areas of future work are proposed:

The idea utilized in generating the T-transform which combines the WHT and the DFT into one orthonormal unitary transform can be utilized to generate other new transforms from the existing transforms, such as Hartley transform, Hilbert transform, etc. This means, the advantages of any two cascaded transforms can be combined together and utilized. Therefore, new transforms can be evaluated with the aim of overcoming the detrimental characteristics for use in UWA channel.

The tests in the presented work were all conducted using single element receivers. In order to further utilize the space diversity and overall throughput, multi-element receivers could be utilized in the further system. Furth more, due to the geometry of multi-element receivers, the varying receiving angles for different receiver elements could be utilized to mitigate the detrimental effect of multipath arrivals. Moreover, the T-OFDM system can be used with alternative diversity techniques such as multiple input multiple output (MIMO) in order to increase diversity over different media of transmission.

The modified ZF equalizer with outlier deletion has revealed superior performance for the proposed system. However, the advantage of utilizing this equalizer decreases when received signal has a low SNR value. With the presence of noise, the difficulty of correctly identifying the outliers in the reciprocal of the generated frequency response increases drastically with the increased noise floor. Hence, future research could focus on noise suppressing on the measured frequency response, such as projecting onto a different domain with better noise separation.

OFDM systems in general are sensitive to synchronization errors resulted from the Doppler Effect due to the closely placed subcarriers in the frequency domain. As a result, its application is limited in platforms with little relative speed. In order to expand its applications onto highly mobile systems such as μROV systems with high accelerations, future research could focus on the investigation of an optimal techniques that can be used to track and/or compensate for the fine and coarse frequency offset caused by Doppler spread.

Reference

1. R. Moore, "Radio communication in the sea," Spectrum, IEEE, vol. 4, no. 11, pp. 42–51, 1967.

2. B. Cochenour, L. Mullen, and A. Laux, "Characterization of the beam-spread function for underwater wireless optical communications links," Oceanic Engineering, IEEE Journal of, vol. 33, no. 4, pp. 513–521, 2008.

3. S. Tang, Y. Dong, and X. Zhang, "On link misalignment for underwater wireless optical communications," *Communications Letters*, *IEEE,* vol. 16, no. 10, pp. 1688-1690, 2012.

4. A. Quazi and W. Konrad, "Underwater acoustic communications," *IEEE Comms. Magazine,* pp. 24-29, Mar. 1982.

5. M. Stojanovic, "Recent advances in high rate underwater acoustic communications," *IEEE J. Oceanic Eng*., pp. 125-136, Apr. 1996.

6. A. Kaya, S.Yauchi, "An acoustic communication system for subsea robot," *Proc. OCEANS'89*, pp.765-770, Seattle, Washington, Oct, 1989.

7. M. Suzuki, T. Sasaki, "Digital acoustic image transmission system for deep sea research submersible," *Proc. OCEANS'92*, pp. 567-570, Newport, RI, Oct, 1992.

8. M. Stojanovic, J.A.Catipovic and J.G. Proakis, "Phase coherent digital communications for underwater acoustic channels," *IEEE J.Oceanic Eng*., vol, 19, pp. 100-111. Jan. 1994.

9. L. Berkhovskikh, Y.Lysanov, *Fundamentals of Ocean Acoustics*, New York: Soringer, 1982.

10. M. Stojanovic, J.Preisig, "Underwater acoustic communication channels: Propagation models and statistical characterization," *IEEE Communications Magazine*, 2009, 47(I): 85-89.

11. M. Stojanovic, "Underwater acoustic communications," *Wiley Encyclopedia of Electrical and Electronics Engineering*, pp. 688-698, 1998.

12. S. Flatte, Ed., *Sound Transmission Through a Fluctuating Ocean*, Cambridge, UK; Cambridge University Press, 1979.

13. R.H.Owen, B.V.Smith and R. F. W. Coates, "An experimental study of rough surface scattering and its effects on communications coherence," in Proc. *OCEANS'94*, pp.III.483-III.488, Brest, France, Sept. 1994.

14. A. Essebbar, G. Loubet and F. Vial, "Underwater Acoustic Channel Simulations for Communications," in Proc. *OCEAN'94*, pp. III.495-III.500, Brest, France, Sept. 1994.

15. A. Falahati, B. Woodward and S. Bateman, "Underwater acoustic channel modes for 4800 b/s QPSK signals," *IEEE J.Oceanic Eng*., vol.16, pp.12-20, Jan.1991.

16. C. Bjerrum-Niese, L.Bjorno, M.A.Pinto and B. Quellec, "A simulation tool for high data-rate acoustic communication in a shallow-water, time-varying channel," *IEEE J. Oceanic Eng*., vol. 21, pp.143-149, Apr.1996.

17. J.Catipovic, "Performance limitations in underwater acoustic telemetry," *IEEE J.Oceanic* Eng., vol. 15, pp.205-216, July 1990.

18. M.Chitre, "A High-Frequency Warm Shallow Water Acoustic Communications Channel Model and Measuremenets," *J. Acoust. Soc. America*, vol. 122, no. 5, Noc, 2007, pp. 2580-86.

19. J. Catipovic, M. Deffenbaugh, L. Freitag, and D. Frye, "An acoustic telemetry system for deep ocean mooring data aquisition and control," in Proc. of MTS/IEEE OCEANS Conference, Seatle, WA, Oct. 1989.

20. J. Gomes, A. Silva, and S. Jesus, "Adaptive spatial combining for passive time-reversed communications," J. Acoust. Soc. Am., vol. 124, no. 2, pp. 1038–1053, Aug. 2008.

21. J. Ling and J. Li, "Gibbs-sampler-based semiblind equalizer in underwater acoustic communications," IEEE Journal of Oceanic Engineering, vol. 37, no. 1, pp. 1–13, Jan. 2012.

22. A. Song, M. Badiey, A. E. Newhall, J. F. Lynch, H. A. DeFerrari, and B. G. Katsnelson, "Passive time reversal acoustic communications through shallow-water internal waves," IEEE Journal of Oceanic Engineering, vol. 35, no. 4, pp. 756 –765, Oct. 2010.

23. G. Ayela, M. Nicot and X. Lurton, "New innovative multi-modulation acoustic communication system," in *Proc. OCEANS'94*, pp. I.292-I.295, Brest, France, Sept, 1994.

24. J. Fisher et al., "A high rate, underwater acoustic data communications transceiver," in *Proc. OCEANS'92*, pp. 571-576, Newport, RI, Oct. 1992.

25. A. Sehgal, I. Tumar and J. Schönwälder, "AquaTools: An Underwater Acoustic Networking Simulation Toolkit," *OCEANS*, Sydney, 24-27 May 2010, pp. 1-10.

26. M. Stojanovic, "On the Relationship between Capacity and Distance in an Underwater Acoustic Communication Channel," *ACM SIGMOBILE Mobile Computing and Communications Review*, Vol. 11, No. 4, 2007, pp. 34-43.

27. M. Johnson, D. Herold and J. Catipovic, "The design and performance of a compact underwater acoustic network node," in Proc. OCEANS'94, pp. III.467-471, Brest, France, Sept, 94.

28. R. F. W. Coates, M. Zheng and L. Wang, "BASS 300 PARACOM: A model underwater parametric communication system," *IEEE J. Oceanic Eng.*, vol. 21, pp. 225-232, Apr. 1996.

29. G. S. Howe et al., "Sub-sea remote communications utilizing an adaptive receiving beamformer for multipath suppression," in Proc, *OCEANS'94*, pp.I.313-316, Brest, France, Sept. 1994.

30. J. Neasham, D. Thompson, A. Tweedy, M. Lawlor, O. Hinton, A. Adams, and B. Sharif, "Combined equalization and beamforming to achieve 20kbits/s acoustic telemetry for rovs," vol, 2, pp.988-993 vol. 2, 1996.

31. M. Stojanovic, J. A. Catipovic and J. G. Proakis, "Phase coherent digital communications for underwater acoustic channels," *IEEE J. Oceanic Eng.*, vol. 19, pp. 100-111, Jan. 1994.

32. M. Stojanovic, J. G. Proakis and J. A. Catipovic, "Performance of a high rate adaptive equalizer on a shallow water acoustic channel," *J. Acoust. Soc. Amer.*, vol. 100 (4), Pt. 1, pp. 2213-2219, Oct. 1996.

33. S. Weinstein, "The history of orthogonal frequency-division multiplexing," Communications Magazine, IEEE, vol. 47, no. 11, pp. 26–35, 2009.

34. B. Li, S. Zhou, M. Stojanovic, L. Freitag and P. Willett, "Multicarrier Communication over Underwater Acoustic Channels with Nonuniform Doppler Shifts," *IEEE Journal of Oceanic Engineering*, vol. 33, No. 2, 2008, pp.198-209.

35. B. Li, S. Zhou, M. Stojanovic, L. Freitag, J. Huang and P. Willett, "MIMO-OFDM over an Underwater Acoustic Channel," OCEANS Vancouver, 29 September-4 October 2007, pp. 1-6.

36. A. Thottappilly, "OFDM for Underwater Acoustic Communication," Master of Science, Virginia Polytechnic Institute and State University, Blacksburg, 2011.

37. B. Muquet, Zhengdao Wang, G. B. Giannakis, M. de Courville and P. Duhamel, "Cyclic prefixing or zero padding for wireless multicarrier transmissions?," in *IEEE Transactions on Communications*, vol. 50, no. 12, pp. 2136-2148, Dec 2002.

38. Z. Wang, S. Zhou, G. B. Giannakis, C. R. Berger and J. Huang, "Frequency-Domain Oversampling for Zero-Padded OFDM in Underwater Acoustic Communications," IEEE Journal of Oceanic Engineering, Vol. 37, No. 1, 2012, pp. 14-24.

39. T. Ebihara and K. Mizutani, "Underwater Acoustic Communication With an Orthogonal Signal Division Multiplexing Scheme in Doubly Spread Channels," IEEE Journal of Oceanic Engineering, vol. PP, No. 99, 2013, pp. 1-12.

40. P. Kumar, "DCT Based OFDM for Underwater Acoustic Communication," 1st International Conference on Recent Advances in Information Technology, Dhanbad, 15-17 March 2012, pp. 170-176.

41. H. Ding, J. A. Neasham, S. Boussakta and C. C. Tsimenidis, "Performance evaluation of T-transform based OFDM in underwater acoustic communications," *OCEANS 2015 - Genova*, Genoa, 2015, pp. 1-7.

42. M. Park, H. Jun, J. Cho, N. Cho, D. H and C. Kang, "PAPR reduction in OFDM transmission using Hadamard transform," IEEE International Conference on Communications, New Orleans, LA, 2000, pp. 430-433, vol.1.

43. M. Ahmed, S. Boussakta, B. Sharif, C. C. Tsimenidis, "OFDM Based on Low Complexity Transform to Increase Multipath Resilience and Reduce PAPR," *IEEE Transactions on Signal Processing*, vol. 59, no. 12, pp. 5994, 6007, Dec. 2011.

44. S. Mason, C. Berger, S. Zhou, and P. Willett, "Detection, synchronization, and Doppler scale estimation with multicarrier waveforms in underwater acoustic communication," *IEEE Journal on Selected Areas in Communications*, vol. 26, no. 9, pp. 1638 –1649, December 2008.

45. H. Jinxing, Y. R. Zheng, W. Jintao and S. Jian, "Dual PN Padding TDS-OFDM for Underwater Acoustic Communication," *Oceans*, Hampton Road, 14-19 October 2012, pp. 1-4.

46. N. Papandreou and T. Antonakopoulos, "Bit and Power Allocation in Constrained Multicarrier Systems: The Single-User Case," *EURASIP Journal on Advances in Signal Processing*, Vol. 2008, No. 1, 2008, p. 11.

47. J. Huang, S. Zhou and P. Willett, "Nonbinary LDPC Cod- ing for Multicarrier Underwater Acoustic Communica- tion," *IEEE Journal on Selected Areas in Communications*, Vol. 26, No. 9, 2008, pp. 1684-1696.

48. C. R. Berger, S. Zhou, J. C. Preisig and P. Willett, "Sparse Channel Estimation for Multicarrier Underwater Acoustic Communication: From Subspace Methods to Compressed Sensing," *IEEE Transactions on Signal Processing*, Vol. 58, No. 3, 2010, pp. 1708-1721.

49. D. Kilfoyle, A. Baggeroer, "The state of the art in underwater acoustic telemetry,", IEEE Journal of Oceanic Engineering, vol. 25, no. 1, pp. 4-27, 2000.

50. 3GPP (Feb. 2003) TSG-RAN-1 Meeting #31, Technical description of the OFDM/IOTA modulation.

51. S. Boussakta and A. G. J. Holt, "Fast algorithm for calculation of both Walsh-Hadamard and Fourier transforms (FWFTs)," *IEE Electron. Lett.*, vol. 25, no. 20, pp. 1352-1354, Sep. 1989.

52. E. C. Ifeachor and B. W. Jervis, *Digital Signal Processing: A Practical Approach*. England: Prentice Hall, 2002.

53. J. W. Cooley and J. W. Tukey, "An algorithm for the machine calculation of complex Fourier series," *Mathematics of computation*, vol. 19, pp. 297-301, 1965.

54. S. S. Kelkar, L. L. Grigsby, and J. Langsnery, "An extension of parseval's theorem and its use in calculating transient energy in the frequency domain," *IEEE Trans. On Industrial Electronics.,* vol. IE-30, no. 1, pp. 42-45, Feb. 1983.

55. M. S. Correngton, *Advanced analytical and signal processing techniques*. ASTLA Document No. AD-277942, April 1962.

56. F. E. Weiser, *Walsh function analysis of instantaneous nonlinear stochastic problems*. PhD thesis, Polytechnic Institute of New York, 1964.

57. N. Ahmed, *Orthogonal Transforms for Digital Signal Processing*. New York: Springer-Verlag, 1975.

58. A. C. Andrews, *Computer Techniques in Image Processing*. New York: Academic Press, 1970.

59. G. Robinson, "Logical convolution and discrete walsh and fourier power spectra," *IEEE Trans. Audio Electroacoust.*, vol. 20, no. 4, pp. 271-280, Oct. 1972.

60. M. Maqusi, *Applied Walsh Analysis*. London: Heyden and Son Ltd, 1981.

61. H. O. Kunz, "On the Equivalence between One-Dimensional Discrete Walsh-Hadamard and Multidimensional Discrete Fourier Transforms", *IEEE Transactions on Computers*, vol. 28(3), 267-8.

62. H. F. Harmuth, Sequency Theory – Foundations and Applications, Academic Press, New York, 1977.

63. J. Arndt, *Matters Computational: Ideas, Algorithms, Source Code*, Springer, 2010.

64. M. G. Karpovsky, R. S. Stanković, and J. T. Astola, Spectral Logic and Its Applications for the Design of Digital Devices, Wiley-Interscience, 2008.

65. E. Chu and A. George, *Inside the FFT Black Box, Serial and Parallel Fast Fourier Transform Algorithm*. CRC Press, 2000.

66. Q. Wen, Y. Xiao, P. Cheng, C. Zhang, and S. Li, "S-PTS for PAPR reduction in OFDM systems," *in Proc. IEEE WiCOM*, 2008, pp. 1-4.

67. R. J. Baxley and J. T. Zhou, "Comparing selected mapping and partial transmit sequence for PAPR reduction," *IEEE Trans. Broadcast.*, vol. 53, no. 4, pp. 737-803, Dec. 2007.

68. L. Yang, K. K. Soo, Y. M. Siu, and S. Q. Li, "A low complexity selected mapping scheme by use of time domain sequence superposition technique for PAPR reduction in OFDM system," *IEEE Trans. Broadcast.*, vol. 54, no. 4, pp. 821-824, Dec. 2008.

69. Ahmed M., S. Boussakta, B. S. Sharif, C. C. Tsimenidis, "OFDM Based on Low Complexity Transform to Increase Multipath Resilience and Reduce PAPR," *Signal Processing, IEEE Transactions on,* vol. 59, no. 12, pp. 5994-6007, Dec. 2011.

70. Xiaodong Li, Chindapol, A., Ritcey, J.A., "Bit-interleaved coded modulation with iterative decoding and 8 PSK signaling," Communications, IEEE Transactions on , vol.50, no.8, pp.1250,1257, Aug 2002.

71. Shah, C.P.; Tsimenidis, C.C.; Sharif, B.S.; Neasham, J.A., "Low-Complexity Iterative Receiver Structure for Time-Varying Frequency-Selective Shallow Underwater Acoustic Channels Using BICM-ID: Design and Experimental Results," Oceanic Engineering, IEEE Journal of , vol.36, no.3, pp.406,421, July 2011.

72. Fang Xu; Xiaoyi Hu; Ru Xu, "A Novel Implementation of Carrier Interferometry OFDM in an Underwater Acoustic Channel," OCEANS 2007 - Europe , vol., no., pp.1,5, 18-21 June 2007.

73. J. G. Proakis and M. Salehi, *Digital Communicatioin*. 5th Ed. New York, USA: McGraw-Hill, 2008.

74. P. Banelli, "Theoretical analysis and performance of OFDM signals in nonlinear fading channels," *IEEE Trans. Wireless Commun.,* vol. 2, no. 2, pp. 284-293, March 2003.

75. C. Snow, L. Lampe, and R. Schober, "Error rate analysis for coded multicarrier systems over quasi-static fading channels," *IEEE Trans. Commun.,* vol. 55, no. 9, pp. 1736-1746, Sep. 2007.

76. S. LiJun, T. Youxi, and L.Shaoqian, "BER performance of differential demodulation OFDM system in multipath fading channels," in *Proc. IEEE GLOBECOM,* China, 2003, pp. 1-5.

77. H. A. Ahmed, A. I. Sulyman, and H. S. Hassanein, "BER performance of OFDM system with channel impairments," in *9th IEEE Int. Workshop on Wireless Local Net. (WLN),* Switzerland, Oct. 2009.

78. Breunig M M, Kriegel H P, Ng R T, et al. LOF: identifying density-based local outliers, ACM sigmod record. ACM, 2000, 29(2): 93-104

79. Wu M, Jermaine C. Outlier detection by sampling with guarantees, Proceedings of the 12th ACM SIGKDD international conference on Knowledge discovery and data mining. ACM, 2006: 767-772.

80. M. Stojanovic, " Low complexity OFDM detector for underwater channels," in Proc. MTS/IEEE OCEANS Conf., Boston, MA, Sep. 18-21, 2006.

81. T. Jiang, Y. Wu, "An Overview: Peak-to-Average Power Ratio Reduction Techniques for OFDM Signals," in *IEEE Transactions on Broadcasting,* vol. 54, no. 2, pp. 257-268, June 2008.

82. S. Litsyn, *Peak Power Control in Multicarrier Communications,* Cambridge University Press, 2007.

83. J. Palicot, Y. Louet, "Power ratio definitions and analysis in single carrier modulations, EUSIPCO, Antalya, Turkey, 2005.

84. H. Ochiai, K. Imai, "On the distribution of the peak-to-average power ratio in OFDM signals," *IEEE Trans. Commun.,* **49**(2), 282-289.

85. S. H. Han, H. J. Lee, "An overview of peak-to-average power ratio reduction techniques for multicarrier transmission. *IEEE Wireless Commun.,* **12**(2), 56-65, 2005.

86. E. J. P. K. Bae, J. G. Andrews, "Quantifying an iterative clipping and filtering technique for reducing PAR in OFDM," *IEEE Trans. Wireless Commun.,* vol. 9, no. 5, pp. 1558-1563, May 2010.

87. J. Armstrong, "Peak-to-average power reduction for OFDM by repeated clipping and frequency domain filtering," *IEEE Elect. Lett.,* vol. 38, no. 5, pp. 246-247, Feb. 2002.

88. T. Jiang, W. Xiang, P. G. Richardson, D. Qu, and G. Zhu, "On the nonlinear companding transform for reduction in PAPR of MCM signals." *IEEE Trans. Wireless Commun.,* vol. 6, no. 6, pp. 2017-2021, June 2007.

89. S. S. Yoo, S. Yoon, S. Y. Kim, and I. Song, "A novel PAPR reduction scheme for OFDM systems: Selective mapping of partial tones (SMOPT)," *IEEE Trans. Consum. Electron.,* vol. 52, no. 1, pp. 40-43, Feb. 2006.

90. K. Kang, S. Chang, "Peak-to-average power control in OFDM using standard arrays of linear block codes," *IEEE Commun. Lett.,* vol. 7, no. 4, pp. 174-176, Apr. 2003.

91. L. Yang, K. K. Soo, Y. M. Siu, and S. Q. Li, "A low complexity selected mapping scheme by use of time domain sequence superposition technique for PAPR reduction in OFDM system," *IEEE Trans. Broadcast.,* vol. 54, no. 4, pp. 821–824, Dec. 2008.

92. D.-W. Lim, J.-S. No, C.-W. Lim, and H. Chung, "A new SLM OFDM scheme with low complexity for PAPR reduction," *IEEE Signal Process. Lett.,* vol. 12, no. 2, pp. 93–96, Feb. 2005.

93. S. J. Heo, H. S. Noh, J. S. No, and D. J. Shin, "A modified SLM scheme with low complexity for PAPR reduction of OFDM systems," *IEEE Trans. Broadcast.,* vol. 53, no. 4, pp. 804–808, Dec. 2007.

94. C.-P. Li, S.-H. Wang, and C.-L. Wang, "Novel low-complexity SLM schemes for PAPR reduction in OFDM systems," *IEEE Trans. Signal Process.,* vol. 58, no.5, pp. 2916–2921, May 2010.

95. C.-L. Wang and S.-J. Ku, "Novel conversion matrices for simplifying the IFFT computation of an SLM-based PAPR reduction scheme for OFDM systems," *IEEE Trans. Commun.,* vol. 57, no. 7, pp. 1903–1907, Jul. 2009.

96. C.-L. Wang and Y. Ouyang, "Low-complexity selected mapping schemes for peak-to-average power ratio reduction in OFDM systems," *IEEE Trans. Signal Process.,* vol. 53, no. 12, pp. 4652–4660, Dec. 2005.

97. A. Ghassemi and T. A. Gulliver, "PAPR reduction of OFDM using PTS and error-correcting code subblocking," *IEEE Trans. Wireless Commun.,* vol. 9, no.3, pp. 980–989, Mar. 2010.

98. S.-J. Ku, C.-L. Wang, and C.-H. Chen, "A reduced-complexity PTS-based PAPR reduction scheme for OFDM systems," *IEEE Trans. Wireless Commun.,* vol. 9, no. 8, pp. 2455–2460, Aug. 2010.

99. Y. Wang, W. Chen, and C. Tellambura, "PAPR reduction method based on parametric minimum cross entropy for OFDM signals," *IEEE Commun. Lett.,* vol. 14, no. 6, pp. 563–565, Jun. 2010.

100.   H. Chen and H. Liang, "PAPR reduction of OFDM signals using partial transmit sequences and Reed-Muller codes," *IEEE Commun. Lett.*, vol. 11, no. 6, pp. 528–530, Jun. 2007.

101.   S. Y. L. Goff, S. S. Al-Samahi, B. K. Khoo, C. C. Tsimenidis, and B. S. Sharif, "Selected mapping without side information for PAPR reduction in OFDM," *IEEE Trans. Wireless Commun.,* vol. 8, no. 9, pp. 3320–3325, Jul. 2009.

102.   A. D. S. Tayalath and C. Tellambura, "SLM and PTS peak-power reduction of OFDM signals without side information," *IEEE Trans. Wireless Commun.,* vol. 4, no. 5, pp. 2006–2013, Dec. 2005.

103.   M. F. Naeiny and F. Marvasti, "Selected mapping algorithm for PAPR reduction of space-frequency coded OFDM systems without side information," *IEEE Trans. Veh. Technol.,* vol. 60, no. 3, pp. 1211–1216, 2011.

104.   S. Kim, J. Chung, and H. Ryu, "PAPR reduction of OFDM signal by the SLM-based WHT and DSI method," in *in Proc. IEEE TENCON, Region 10 conf., Nov. 2006, pp. 1-4.*

105.   M. Park, H. Jun, J. Cho, N. Cho, D. Hong, and C. Kang, "PAPR reduction in OFDM transmission using Hadamard transform," in *in Proc. IEEE ICC, New Oreleans, LA, USA,* pp. 430-433, June 2000.

106.   Z. Hu, H. Wan, "A novel generic fast Fourier transform pruning technique and complexity analysis," *IEEE Trans. Signal Process.,* vol. 53, no. 1, pp. 274-282, Jan. 2005.

107.   Sharif, B.S.; Neasham, J.; Hinton, O.R.; Adams, A.E., "A computationally efficient Doppler compensation system for underwater acoustic communications," Oceanic Engineering, IEEE Journal of , vol.25, no.1, pp.52,61, Jan. 2000.

108.   Kumar, P., Kumar, P., "Performance Evaluation of DFT-Spread OFDM and DCT-Spread OFDM for Underwater Acoustic Communication," Vehicular Technology Conference (VTC Fall), 2012.

109.   Baosheng Li; Shengli Zhou; Stojanovic, M.; Freitag, L., "Pilot-tone based ZP-OFDM Demodulation for an Underwater Acoustic Channel," OCEANS 2006 , vol., no., pp.1,5, 18-21 Sept. 2006.

110.   W. H. Thorp, "Analytic description of the low-frequency attenuation Coefficient," The Journal of Acoustical Society of America, vol. 42, p. 270, 1967.

111.   Y. V. Zakharov and A. K. Morozov, "OFDM Transmission Without Guard Interval in Fast-Varying Underwater Acoustic Channels," in *IEEE Journal of Oceanic Engineering,* vol. 40, no. 1, pp. 144-158, Jan. 2015.

112.   J. Li, L. Liao and Y. V. Zakharov, "Space-time cluster combining for UWA communications," *OCEANS 2016 – Shanghai,* Shanghai,2016, pp. 1-6.

113.   J. J. Beek, O. Edfors, M. Sandell, S. K. Wilson, and P. O. Borjesson, "On channel estimation in OFDM systems," in *Proc. IEEE VTC,* Jul. 1995, vol. 2, pp. 815-819.

114.   J. G. Proakis, D. G. Manolakis, *Digital Signal Processing,* 3rd edition, NJ,:Prentice-Hall, 1996.

115.   Grubbs, Frank (1950), Sample Criteria for Testing Outlying Observations, *Annals of Mathematical Statistics,* 21(1) pp. 27-58.